

1-1-2015

# Theoretical and Experimental Investigations to Improve the Performance of Surface Acoustic Wave (SAW) Biosensors

Mandek Richardson

*University of South Florida*, [mbrichar@mail.usf.edu](mailto:mbrichar@mail.usf.edu)

Follow this and additional works at: <http://scholarcommons.usf.edu/etd>

 Part of the [Biomedical Engineering and Bioengineering Commons](#)

---

## Scholar Commons Citation

Richardson, Mandek, "Theoretical and Experimental Investigations to Improve the Performance of Surface Acoustic Wave (SAW) Biosensors" (2015). *Graduate Theses and Dissertations*.  
<http://scholarcommons.usf.edu/etd/5566>

This Dissertation is brought to you for free and open access by the Graduate School at Scholar Commons. It has been accepted for inclusion in Graduate Theses and Dissertations by an authorized administrator of Scholar Commons. For more information, please contact [scholarcommons@usf.edu](mailto:scholarcommons@usf.edu).

Theoretical and Experimental Investigations to Improve the Performance of Surface Acoustic  
Wave (SAW) Biosensors

by

Mandek Richardson

A dissertation submitted in partial fulfillment  
of the requirements for the degree of  
Doctor of Philosophy in Biomedical Engineering  
Department of Chemical and Biomedical Engineering  
College of Engineering  
University of South Florida

Major Professor: Venkat Bhethanabotla, Ph.D.  
Patricia Kruk, Ph.D.  
Robert Frisina, Ph.D.  
Gokhan Mumcu, Ph.D.  
Anna Pyayt, Ph.D.

Date of Approval:  
December 1, 2014

Keywords: Biosensing, non-specific binding, microcavities, immunoassay, phononics

Copyright © 2015, Mandek Richardson

## **DEDICATION**

This work is dedicated to my late grandmother, Eva Kendrick. You're the one who filled me with a thirst for knowledge, and I will never forget the many life lessons you've taught me.

## **ACKNOWLEDGMENTS**

I would like to start off by thanking my family for all their love and support. Specifically, my mother, Karen Richardson, my brother, Mikkell Richardson and my wife Shaheda Richardson. This has been a long process and I couldn't have done it without all of your support.

I would like to thank my advisor Dr. Venkat Bhethanabotla, for giving me an opportunity and guiding me along this process. I would also like to thank Dr. Patricia Kruk, Dr. Anna Pyayt, Dr. Robert Frisina, and Dr. Gokhan Mumcu for being on my committee and providing valuable advice and input.

I would like to express my gratitude to Mr. Bernard Batson and Dr. Sylvia Thomas for helping to open doors and exposing me to scientific research. Thank you to Dr. Subramanian Sankaranarayanan for his collaboration and guidance on a significant part of this work. Thanks to the staff at the Nanotechnology Research and Education Center (NREC), particularly Richard Everly, Robert Tufts, Jay Bieber, and Sclafani Louis-Jeune for providing training and expertise during the many hours I spent at the center working on my research. I would like to thank Dr. Karen Liller for selecting me as a participant in the Doctoral Leadership Institute and Dr. Thomas Weller for serving as my mentor while at the institute. Being a leadership fellow played a significant role in my maturation and development as a doctoral student. Additional thanks to, Dr. Byeong Cha from the Lisa Weitz Advanced Microscopy & Cell Imaging Core Laboratory, Mr. Leigh West from the Center of Drug Discovery and Innovation, and the staff from USF

Research Computing. Special thanks to Dr. Vonzell Agosto, for the many valuable and helpful discussions over the last several years.

Lastly, I would like to thank all those persons who weren't mentioned, who over the course of this work engaged me in discussions, answered questions, or merely listened when I needed someone to talk to.

## TABLE OF CONTENTS

LIST OF TABLES .....	iv
LIST OF FIGURES .....	v
ABSTRACT.....	ix
CHAPTER 1: INTRODUCTION .....	1
1.1 Motivation.....	1
1.2 Objectives .....	2
1.2.1 Decreasing Insertion Loss with Microcavities.....	3
1.2.2 Biofouling Removal.....	3
1.3 Brief Description of Biosensors.....	4
1.4 Quick Overview of SAW Biosensors .....	6
1.5 Organization of Dissertation .....	6
CHAPTER 2: HISTORICAL OVERVIEW AND LITERATURE REVIEW .....	9
2.1 Introduction.....	9
2.2 Overview of SAW Devices.....	9
2.2.1 Interdigital Transducers (IDTs) and SAW Delay Line Device .....	10
2.2.2 First SAW Sensors .....	11
2.3 SAW Biosensors .....	13
2.4 Love Wave Biosensors .....	14
2.5 Various Applications of SAW Biosensors.....	16
2.5.1 SAW DNA Sensors.....	16
2.5.2 SAW Bacteria Sensors.....	17
2.5.3 SAW Sensors and Cancer Detection.....	18
2.6 Removal of Non-Specifically Bound Proteins.....	18
2.7 Finite Element Modeling (FEM) of SAW Sensors.....	21
CHAPTER 3: SAW SENSOR DESIGN AND FINITE ELEMENT MODEL .....	25
3.1 Material Selection .....	25
3.2 IDT Design.....	26
3.3 Device Fabrication .....	28
3.4 Measured SAW Frequency Response.....	29
3.5 Application of a Waveguide .....	31
3.6 Immobilization of Biorecognition Elements.....	34
3.6.1 Physical Adsorption .....	34

3.6.2 Covalent Immobilization Using Silane Chemistry .....	35
3.7 Integration of Microfluidic Device with a SAW Sensor .....	37
3.8 Measurement Setup for Orthogonal SAW Experiments.....	40
3.9 Finite Element Model (FEM) of SAW Sensor .....	41
CHAPTER 4: LOW INSERTION LOSS AND HIGHLY SENSITIVE SH-SAW SENSORS BASED ON 36° YX LiTaO <sub>3</sub> THROUGH THE INCORPORATION OF FILLED MICROCAVITIES.....	45
4.1 Introduction.....	46
4.2 Computational Details .....	48
4.2.1 Choice of Substrate, Geometry, and Materials .....	48
4.2.2 Theory .....	50
4.2.3 Finite Element Model .....	51
4.2.4 Simulation Analysis.....	52
4.2.5 Fabrication of SAW Devices with Microcavities .....	53
4.2.6 Device Measurement and Characterization .....	54
4.3 Results and Discussion .....	54
4.3.1 Frequency Response and Material Displacements for 36°YX LiTaO <sub>3</sub> .....	54
4.3.2 Comparison of Insertion Loss.....	56
4.3.3 Mass Sensitivity Analysis.....	58
4.3.4 Comparison of Displacement Contours and Profiles.....	61
4.3.5 SAW Devices with Microcavities.....	65
4.4 Conclusions.....	67
CHAPTER 5: SHEAR-HORIZONTAL SURFACE ACOUSTIC WAVE PHONONIC DEVICE WITH HIGH DENSITY FILLING MATERIALS FOR ULTRA-LOW POWER SENSING APPLICATIONS .....	71
5.1 Introduction.....	71
5.2 FEM of Tungsten and Tantalum Filled Microcavities.....	73
5.3 Fabrication and Measurement of Tungsten and Tantalum Filled Microcavities .....	79
5.4 Conclusion .....	81
CHAPTER 6: REMOVAL OF NON-SPECIFICALLY BOUND PROTEINS USING RAYLEIGH WAVES ON AN ST-QUARTZ SUBSTRATE .....	83
6.1 Introduction.....	84
6.2 Mechanism of NSB Protein Removal.....	85
6.3 Computational Details .....	88
6.3.1 Model Setup.....	89
6.3.2 Piezoelectric Domain.....	89
6.3.3 Fluid Domain .....	90
6.3.4 Coupling from Solid Domain to Fluid Domain .....	90
6.3.5 Coupling from Fluid Domain to Solid Domain .....	91
6.4 Computational Results and Discussion .....	91
6.5 Materials and Methods.....	94
6.5.1 SAW Device Fabrication.....	94
6.5.2 Micropatterning the SAW Delay Path .....	94

6.5.3 Surface Modification and Attachment of Capture Antibody .....	94
6.5.4 Determination of Specific and Non-Specific Binding .....	95
6.5.5 Fluorescent Imaging.....	96
6.5.6 Protein Removal with Acoustic Energy.....	97
6.6 Experimental Results and Discussion.....	97
6.6.1 Removal of Non-Specifically Bound Antigen from Sensing and Non Sensing Regions.....	98
6.6.2 Removal of an Interfering Protein from Sensing and Non-Sensing Regions .....	100
6.6.3 Renewal of Sensor Surface .....	102
6.7 Conclusions.....	103
CHAPTER 7: SIMULTANEOUS DETECTION AND REMOVAL OF NON- SPECIFICALLY BOUND PROTENS USING ORTHOGONAL SURFACE ACOUSTIC WAVE TRANSDUCERS ON ST-QUARTZ.....	105
7.1 Introduction.....	105
7.2 Results and Discussion .....	109
7.2 Conclusions.....	115
CHAPTER 8: FUTURE WORK .....	116
8.1 Summary of Contributions.....	116
8.2 Future Work.....	120
8.2.1 SAW with Microcavities Combined with Waveguide.....	120
8.2.2 Microcavities Used as Reflectors.....	121
8.2.3 Orthogonal SAW with Microcavities .....	122
8.2.4 Integration of a Dual Delay Line with Orthogonal SAW Sensor .....	122
REFERENCES .....	123
APPENDICES .....	140
Appendix A Copyright Permissions for Chapter 4.....	141
Appendix B Copyright Permissions for Chapter 5 .....	142

## LIST OF TABLES

Table 3.1	Relevant SAW parameters used in device designs for theoretical and experimental studies.....	28
Table 3.2	Comparison between theoretical and measured center frequency for each wave mode used.....	30
Table 4.1	Results from frequency response simulations for the various device configurations .....	57
Table 4.2	Simulation results comparing IL for air, ZnO, and NCD filled cavities to a standard device where the cavity depth is 1 $\mu\text{m}$ .....	66
Table 5.1	Relevant material properties for the substrate and filling materials under study .....	79
Table 6.1	Forces (in Newtons) as a function of device frequency.....	93
Table 7.1	Comparison between theoretical and measured center frequency values for each wave mode.....	111

## LIST OF FIGURES

Figure 1.1 Illustration of the typical elements that make up a biosensor.....	5
Figure 2.1 Illustration of a SAW delay line device.....	11
Figure 2.2 Illustration of a Love-wave sensor.....	15
Figure 3.1 A schematic showing the different wave modes generated on ST-quartz with respect to how the IDT pairs are oriented to the crystalline x-axis. ....	26
Figure 3.2 Schematic of a SAW delay line with single split finger input and output IDTs.....	27
Figure 3.3 Process flow used in the fabrication of SAW devices on ST-quartz. ....	29
Figure 3.4 Frequency responses for (a) SH-SAW mode and (b) Rayleigh mode. ....	30
Figure 3.5 Illustration of how a SSBW is converted to a Love-wave when a waveguide material is applied to the sensor surface. ....	32
Figure 3.6 Comparison of the frequency responses for an ST-quartz sensor without a waveguiding layer (red) and with a waveguiding layer (blue). ....	33
Figure 3.7 Illustration of the biosensing layer used when the sensor has the following configuration: piezoelectric substrate/waveguide/gold film. ....	35
Figure 3.8 Illustration of the bare ST-quartz substrate modified with a 3-GPS layer to covalently attach antibodies for biosensing. ....	36
Figure 3.9 Illustration of a microfluidic device design for a SAW sensor chip.....	38
Figure 3.10 Frequency response curves for an ST-quartz sensor under three conditions .....	39
Figure 3.11 Schematic of a SAW sensor with orthogonally placed transducers .....	40
Figure 3.12 Illustration of measurement setup for removal and sensing experiments. ....	41
Figure 3.13 Image of the SAW delay line model used in ANSYS FEM simulations. ....	42

Figure 3.14 Simulated frequency response of the SSBW on ST-quartz using ANSYS .....	43
Figure 3.15 Simulated nodal displacements at the output IDT for SSBW propagating in ST-quartz.....	44
Figure 4.1 (a) Image of FE model of SAW device with filled microcavities used in ANSYS simulations and (b) illustration of SAW device with filled microcavities .....	52
Figure 4.2 Simulated frequency response for a two-port SAW device based on bare 36° YX LiTaO <sub>3</sub> , where delay paths equal 3λ and 10λ are compared .....	55
Figure 4.3 Displacements vs. time for 36° YX LiTaO <sub>3</sub> .....	55
Figure 4.4 (a) Comparison of the simulated frequency responses for the different device with microcavity depth equal to (a) 2.5 μm and (b) 5 μm .....	56
Figure 4.5 Comparison of mass sensitivity with respect to changes in IL (ΔIL) for all device configurations studied, where the microcavity depths are 2.5 μm and 5 μm deep.....	59
Figure 4.6 Comparison of mass sensitivity with respect to changes in resonant frequency (Δf <sub>0</sub> ) for all the device configurations studied, where microcavity depths are 2.5 μm and 5 μm deep.....	60
Figure 4.7 Nodal contour plots of sum of x, y and z displacements at a time step of 110 ns for (a) device with no microcavities in the delay path, (b) air filled cavities, (c) ZnO filled cavities and (d) NCD filled cavities; the microcavity depths are 2.5 μm .....	62
Figure 4.8 (Top view) Nodal contour plots of sum of x, y and z displacements at a time step of 110 ns for (a) bare SAW device, (b) air filled cavities, (c) ZnO filled cavities and (d) NCD filled cavities; the microcavity depths are 2.5 μm .....	63
Figure 4.9 Nodal displacements at the output IDT vs. time for all the different device configurations in (a) SH (y) direction, (b) longitudinal (x) direction and (c) substrate normal (z) direction; the microcavity depth is 2.5 μm .....	64
Figure 4.10 Image taken from a microscope of the SAW delay path showing etched microcavities next to an IDT at (a) 5X magnification and (b) 20X magnification .....	65
Figure 4.11 Measure frequency responses for a device with air-filled microcavities in the delay path (blue curve) and a device with no microcavities in the delay path (red curve).....	67

Figure 5.1 Simulated results for IL vs. frequency is plotted and compared for a device without microcavities and devices having microcavities filled with tungsten or tantalum where the cavity depth is (a) 2.5 $\mu\text{m}$ and (b) 5 $\mu\text{m}$ .	74
Figure 5.2 Sectional view of substrate showing displacements at a time step = 110 ns for (a) 2.5 $\mu\text{m}$ deep cavities filled with tantalum, (b) 5 $\mu\text{m}$ deep cavities filled with tantalum, (c) 2.5 $\mu\text{m}$ filled cavities filled with tungsten and (d) 5 $\mu\text{m}$ cavities filled with tungsten	77
Figure 5.3 Top view of substrate showing displacements at a time step = 110 ns for (a) 2.5 $\mu\text{m}$ deep cavities filled with tantalum, (b) 5 $\mu\text{m}$ deep cavities filled with tantalum, (c) 2.5 $\mu\text{m}$ deep cavities filled with tungsten and (d) 5 $\mu\text{m}$ deep cavities filled with tungsten	77
Figure 5.4 (a) SAW chip is shown prior to etching microcavities and filling with Ta	81
Figure 6.1 Coupled field FE FSI predicted mechanism of ultrasonic removal of particles weakly bound to a surface	88
Figure 6.2 Streaming velocities along the delay path with respect to device frequency	92
Figure 6.3 Processing steps to create patterned areas where specific binding occurs	96
Figure 6.4 Results indicating the removal of non-specifically bound antigens (goat anti-rabbit IgG) from the SAW delay path	99
Figure 6.5 Results indicating the removal of an interfering protein (donkey anti-mouse IgG) from the SAW delay path	101
Figure 6.6 Results after applying an amplified RF signal to the SAW input	103
Figure 7.1 Coupled field FE FSI predicted mechanism of ultrasonic removal of particles weakly bound to a surface	108
Figure 7.2 Illustration of the orientation of the SAW transducers for the different wave modes with respect to the crystalline x-axis which is perpendicular to the wafer flat	109
Figure 7.3 (a) Image of SAW device with orthogonally oriented transducers and measured frequency response of (b) SSBW wave mode and (c) Rayleigh wave mode	110
Figure 7.4 Plot of phase vs. time of the sensing path of the orthogonal SAW sensor during operation	112

Figure 7.5 Frequency response of Rayleigh wave delay line with (red) and without (blue) conjugate matching of the input and output ports.....113

Figure 7.6 Plot of phase vs. time of the sensing path of the orthogonal SAW sensor during operation .....115

## **ABSTRACT**

The objective of this dissertation is to improve the performance of surface acoustic wave (SAW) biosensors for use in point-of-care-testing (POCT) applications. SAW biosensors have the ability to perform fast, accurate detection of an analyte in real time without the use of labels. However, the technology suffers from the inability to differentiate between specific and non-specific binding. Due to this limitation, direct testing of bodily fluids using SAW sensors to accurately determine an analyte's concentration is difficult. In addition, these sensors are challenged by the need to detect small concentrations of a biomarker that are typically required to give a clinical diagnosis. Sensitivity, selectivity and reliability are three critical aspects for any sensing platform. To improve sensitivity the delay path of a SAW sensor has been modified with microcavities filled with various materials. These filled cavities increased sensitivity by confining wave energy to the surface by way of constructive interference and waveguiding. Thus, the improved sensitivity will result in a lower limit of detection. In addition, insertion loss is decreased as a consequence of increased wave confinement to the surface. Sensor selectivity and reliability are adversely affected by non-specific binding of unwanted species present in a sample. To address this issue a multifunctional SAW sensor is presented. The sensor consists of two SAW delay lines oriented orthogonal to each on ST-quartz in order to generate two distinct wave modes. One wave mode is used for sensing while the other is used to remove loosely bound material. By using the same transduction mechanism for both removal and sensing, the

sensor chip is simplified and complex electronics are avoided. The findings of this research involve the technological advances for SAW biosensors that make their use in POCT possible.

## CHAPTER 1: INTRODUCTION

A sensor is a device that converts a physical quantity into an observable and measurable signal. There are many instances in our daily lives where we interact with a type of sensor and may not realize it. Some examples are the touch screen at an ATM, motion detectors that turn lights on/off in a corridor, or the scale at a doctor's office. No matter the sensor's intended purpose, they all share common characteristics. Every sensor must be sensitive to a desired physical or chemical change while being insensitive to environmental influences. However, the sensor itself must not have any influence on the measurement.

The first biosensor was introduced by Clark and Lyons in 1962 and was based on the amperometric detection of glucose using an enzyme electrode [1, 2]. Since that time biosensors have played and continue to play a significant role in food safety, homeland security, environmental monitoring, and clinical applications, such as clinical diagnostics and drug discovery [2]. Current and future research will be focused towards point of care (POC) systems having the ability to perform simultaneous multiple analyte analysis (multiplexing) and high throughput screening [3]. The goal of these sensing systems are to integrate the analytical capabilities of a clinical lab into an inexpensive portable device [3]. This will allow sensing to take place at a patient's bedside, in the environment, or in a home.

### 1.1. Motivation

Although there are a number of diverse applications in which biosensors can be used, clinical diagnostics are where biosensors are used most [2]. This is based on the need to assess a

patient's health by monitoring physiological parameters and to identify biomarkers that result in disease diagnosis or prognosis. Currently most biosensing is done in a clinical laboratory with expensive bulky equipment that require operation and analysis by highly skilled personnel [4-6]. In addition, most of these tests take days to give results. By switching to biosensors, the potential to perform rapid and accurate real-time detection in a physician's office, clinic or at home is possible. The advantages for moving away from clinical lab tests to POC biosensors are the alleviation of psychological stress to patients as they await test results [2], improved patient care due to quicker decisions by the clinician of treatment options, and increased revenue for primary care physicians because diagnostic tests are performed in the office or clinic.

Besides the positive impact biosensors could have in the area of clinical diagnostics, market size and growth are also key factors that are driving biosensor research. In 2011, the global biosensors market was valued at \$9.9 billion (USD) and is expected to grow nearly 10% per year until 2018 [7]. This growth is led, in part, by demands for in-home care diagnostics and point-of-care-testing (POTC). However, despite the tremendous growth and advances in biosensor research, commercialization of biosensors is very slow. One reason is the high costs required to bring a biosensor to market [8]. Another challenge is the ability to get approval from the relevant regulatory agencies. This would require overcoming key technical hurdles such as stability, sensitivity, and reliability [8]. In the end, biosensors must be inexpensive, reliable, operate under various conditions, have a shelf-life of more than one month, and have the ability to detect multiple targets to increase their commercial value [3].

## **1.2. Objectives**

This work focuses on the use of surface acoustic wave (SAW) devices as biosensors. For SAW sensors to be successful in clinical diagnostics they must meet specifications on key

sensing parameters such as sensitivity, limit of detection and accuracy. These parameters have a direct correlation with clinically relevant criteria such as threshold, and minimal false positive and false negative test results.

### ***1.2.1. Decreasing Insertion Loss with Microcavities***

A typical SAW sensor suffers from high insertion loss [9]. This is problematic because IL is inversely related to sensor sensitivity. In addition, high power losses bring about the generation of heat, which can adversely affect protein activity. Several approaches have been utilized to decrease power loss which includes the incorporation of reflective gratings [10], grooves and corrugated surfaces [11], and the application of a waveguide material [12, 13]. The first aim of this dissertation is to decrease IL and subsequently increase sensitivity. To achieve this, a SAW delay path has been modified with microcavities. This includes theoretical and experimental investigations of how cavity geometry and different filling materials affect sensor performance. From the conclusions resulting from this work, an optimal device configuration can be conceived.

### ***1.2.2. Biofouling Removal***

To overcome key technical issues such as stability, sensitivity and reliability, the problem of biofouling needs to be solved. Biofouling is a significant issue that occurs when a biosensor is exposed to a complex medium (i.e. blood, plasma, or urine) which contains various macromolecules in addition to the analyte of interest. Effects of biofouling can include false positive test results and decreased sensor performance. Today most sensing performed with biosensors occur on idealized samples. These samples usually consist of the target analyte isolated in a buffer solution which doesn't reflect a real world scenario. Therefore, in order for a particular biosensor technology to have commercial success, it must perform as well or better

than established clinical lab tests on a real sample (i.e. blood, urine, etc.). In addition, sensor sensitivity, limit of detection and stability can be improved if biofouling is removed.

Consequently, the second aim of this dissertation is to improve the performance of a SAW sensor by reducing and or eliminating biofouling that occurs from the non-specific binding of proteins.

To accomplish this task a SAW sensor was developed that utilizes two distinct wave modes. One wave mode is used to sense a biorecognition event occurring at the sensor surface, and the other wave mode removes loosely bound material (biofouling) by SAW induced acoustic streaming.

To generate the two different wave modes, two pairs of interdigital transducers (IDTs) are fabricated orthogonal to each other in a delay line setup. The orthogonal transducer configuration utilizes the anisotropic material properties of ST-Quartz, which allows generation of the two different wave modes. Due to ability of the orthogonal SAW device to perform both actuation and sensing, real bodily fluids could be tested with this sensor in the future.

### **1.3. Brief Description of Biosensors**

What differentiates a biosensor from other types of sensors is the incorporation of a biologically derived molecule with a transducer to recognize an intended target with high selectivity (Figure 1.1) [14, 15]. A variety of biological components (enzymes, antibodies, antigens, nucleic acids, isolated receptors, whole cells, microorganisms, and plant and animal tissue) have been utilized in biosensing applications [16]. Biosensors can have many different classifications depending on the intended application, type of interaction, transduction principle, or if a label is used.

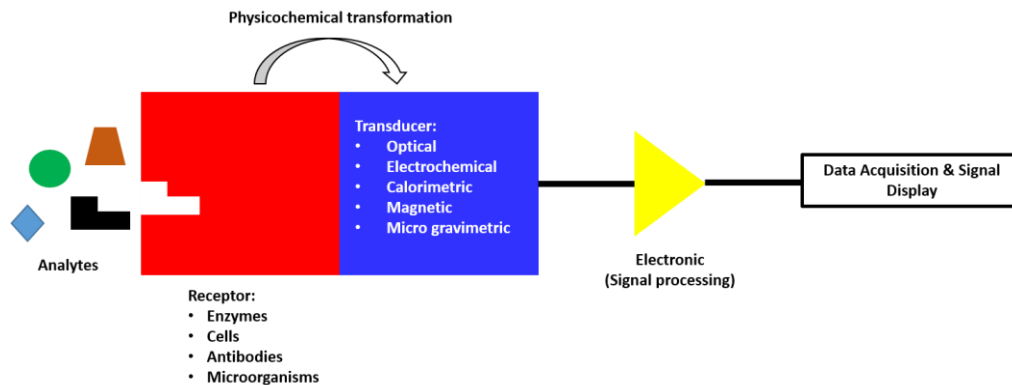


Figure 1.1 Illustration of the typical elements that make up a biosensor

The class of biosensors relevant to this work are affinity biosensors. These sensors have biorecognition elements that rely on high affinity interactions such as antigen-antibody, DNA-DNA, and cell receptor-small molecule. The interactions are usually characterized by a lock and key model, which describes the selective interaction between pairs of macromolecules [14].

The transducer of a biosensor converts a biochemical signal to an electronic signal to be read and interpreted by the operator (Fig. 1). Common transducer types are electrochemical, optical, thermal, and piezoelectric. Most biosensing systems on the market today are electrochemical based [8, 17], the majority of which are glucose sensors [8]. The next most common type of transducers are optical followed by piezoelectric.

Biosensors can be separated into two groups depending on whether the detected signal requires a label. If a biosensor needs a label, this type of sensor would be deemed indirect. In this setup a secondary molecule (e.g. enzyme or radioisotope) generates the signal (e.g. fluorescent or radioactivity). In contrast, if no label is required the sensor would be known as direct. An example would be the direct detection of a mass change. The advantage of a label based sensor is high sensitivity with minimal adverse effects from non-specific binding interactions. However, use of labels increase the complexity and cost of the sensing platform

[18]. In addition, measurements don't occur in real time and assay times could take up to several hours due to several binding reactions that need to occur to attach the label. By comparison, label free sensors allow measurements to be taken in real time with much faster response times. Despite the fast response times, label free sensors suffer from non-specific binding reactions that can negatively affect the sensor response.

#### **1.4. Quick Overview of SAW Biosensors**

A variety of biosensing technologies exist that can be used for clinical diagnostics. This work focuses on the use of surface acoustic wave (SAW) devices as biosensors. SAW devices with shear horizontal particle polarization provide a reliable, fast, cost-effective way to detect label-free interactions between biomolecules in real time. SAW sensors rely on the piezoelectric effect for transduction via a pair of interdigital transducers (IDTs) deposited on the surface. Exciting the IDTs with a time-varying voltage generates acoustic waves that are affected by changes to the propagation path. These changes can be monitored with high sensitivity by observing the wave's frequency, velocity and/or amplitude. Detection of cardiac makers [19], viruses [20], a breast cancer marker (*HER-2/neu*) [21, 22] and bacteria [23] are examples of applications involving SAW biosensors.

#### **1.5. Organization of Dissertation**

This dissertation is organized as follows.

Chapter 2 provides a historical overview and brief survey of the literature on SAW devices and their subsequent use as sensors. Specifically, major developments in the field of SAW sensors over the years will be highlighted and will conclude with their use in different biosensing applications. This chapter will also discuss the issue of non-specific binding of

proteins and what methods have been employed to eliminate this problem. In addition, FE modeling of SAW sensors is briefly discussed.

Chapter 3 provides the background information necessary to complete the studies in chapters 4-7. The various aspects that go into the design of the sensor platform is presented which includes, choice of material, IDT design, device fabrication, immobilization techniques, microfluidic design and measurement setup. Also, details of the FE model used to study various SAW sensor configurations in the theoretical investigations are provided.

Chapter 4 presents the use of a 3-D FE model to compare a standard SAW device to a SAW device containing unfilled microcavities and microcavities filled with ZnO or nanocrystalline diamond (NCD). In addition, IL measurements are compared for a SAW device with cavities and one without to determine if the aforementioned simulations reveal any trends. There are a couple of reasons why the proposed device configurations would be of great interest to the sensor field: for wireless sensing applications which require minimal power consumption; and to detect analytes at low concentrations in which high sensitivity is needed.

Chapter 5 describes the theoretical and experimental study of a phononic SH-SAW device comprised of a microcavity array filled with high density materials (tungsten or tantalum). Based on key material properties of tungsten and tantalum, power transfer can be increased or decreased. SAW devices having tantalum and tungsten filled microcavities were fabricated and measured to validate simulations.

Chapter 6 details a study on the removal of non-specifically bound proteins using a Rayleigh wave mode on ST-Quartz. First, results from a 3-D FE fluid solid interaction (FSI) model are given. The simulations were used to determine if the SAW induced forces generated are sufficient in strength to overcome adhesive forces that non-specifically bind particles to the

surface. Next experiments were conducted to determine if SAW acoustic streaming forces could remove non-specifically bound proteins. Equally important was to see if these forces would disrupt specific binding and if they were increased, could remove specifically bound antigens.

In Chapter 7 a SAW device consisting of orthogonally placed transducers on an ST-Quartz substrate is presented. This “orthogonal SAW” device was used to perform simultaneous detection and removal of non-specifically bound proteins. This work is of interest to individuals working in clinical diagnostics because it could pave the way for rapid and accurate testing of bodily fluids acquired directly from patients.

Chapter 8 summarizes the main contributions of this dissertation and provides suggestions of how to continue developing the SAW sensor designs presented.

## **CHAPTER 2: HISTORICAL OVERVIEW AND LITERATURE REVIEW**

### **2.1. Introduction**

The purpose of this chapter is to briefly discuss the fundamental aspects of surface acoustic wave (SAW) devices, with a particular emphasis on SAW delay line structures, and how these devices have been used for sensing. Some historical background is provided to highlight major developments in the field. This is followed by an overview of the different biosensing applications in which SAW devices have been used. Lastly, a brief synopsis of finite element models (FEMs) and a quick survey of the literature with respect to their use in SAW sensor designs is also given.

### **2.2. Overview of SAW Devices**

SAW devices generate and detect acoustic waves via the transduction of electrical energy to mechanical energy via transducers fabricated on the surface of a piezoelectric material. Piezoelectricity was first described by Pierre and Paul-Jacques Curie in 1880 [24]. In their work they discovered that when applying stress to certain materials (i.e. zinc blende, tourmaline, cane sugar, topaz, and quartz), charges would appear at their surface[25]. The first useful application of piezoelectric materials was made by Cady in 1921 when he used a quartz resonator to stabilize electronic oscillators [26, 27]. Piezoelectricity is a phenomenon associated with the generation of surface charges when a material lacking a center of symmetry is put under stress. The reciprocal effect is also possible. When a voltage is applied to the surface of a piezoelectric

material, deformation of the material (i.e. compression or elongation) will occur. Whether the material becomes compressed or elongated is determined by the polarity of the voltage signal.

### ***2.2.1. Interdigital Transducers (IDTs) and SAW Delay Line Device***

In 1965, White and Voltmer discovered that placement of spatially periodic electrodes (interdigital transducers (IDTs)) on the surface of a piezoelectric material could generate a surface wave [28]. Until that time electrodes were placed on the top and bottom surface of a piezoelectric crystal to generate compressional and shear waves. IDTs are formed by combining two comb-shaped structures made from a deposited metal film that is patterned by photolithography and etching. Typically the metal used to make IDTs is aluminum. However, when immersed in liquids, gold on a chromium, or titanium adhesion layer is preferred to avoid corrosive effects. The simplest IDT geometry consists of equal electrode finger width and inter-electrode spacing. The transducer operates at its synchronous frequency, where the acoustic wavelength ( $\lambda$ ) is equal to the IDT periodicity. At this frequency constructive interference occurs between waves whose travel time between IDT finger pairs is equal to period of the applied AC signal [29].

Figure 2.1 shows a simple SAW delay line structure. It contains two IDTs deposited on a piezoelectric substrate or thin film, separated by some pre-determined distance. To avoid cross talk the distance between IDTs should be at least  $100\lambda$  [24]. An RF signal is applied at the input IDT causing a time varying stress within the material, which results in acoustic wave propagation. As the wave travels across the substrate it creates mechanical displacements in the material that are accompanied by an electric potential. The generated SAW has extremely low velocity compared with electromagnetic waves and low propagation losses. This allows devices to be extremely compact in size and used in systems that require low power. Additionally, the

ability to monitor changes that occur due to wave/matter interactions is made easier by configuring the transducers into a delay line structure.

After the invention of the IDT in 1965 by White and Voltmer [28], the electronics industry quickly realized the potential for SAW devices in analog filter design and signal processing to generate, delay and filter RF signals [30]. At present, commercial use of SAW devices is primarily in the telecommunications industry for mobile cell phones and base stations. Their primary use in this area is to serve as bandpass filters in RF and IF sections of transceivers.

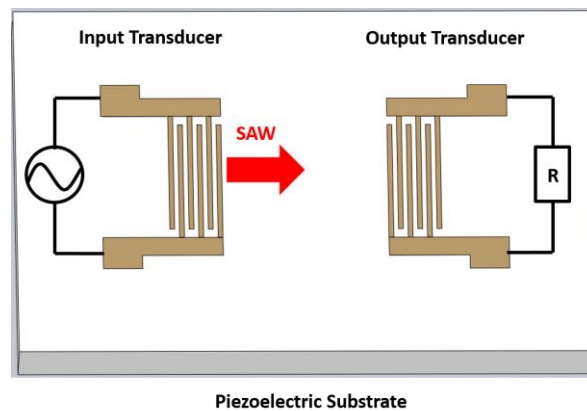


Figure 2.1 Illustration of a SAW delay line device

### 2.2.2. First SAW Sensors

It was in 1885 that Lord Rayleigh proved that mechanical waves similar to water waves travel on the surface of a solid and these waves have since been given the name Rayleigh waves [29]. In general, there are several types of acoustic waves that exist based on how particles move relative to their equilibrium position. There is the longitudinal wave, in which particles in a material are compressed and expanded relative to each other. A second type is a shear wave, where particles move orthogonal to the direction of propagation. Consequently, there are two different types of shear waves, the shear vertical (SV) wave and shear horizontal (SH) wave. The previously mentioned Rayleigh wave represents a third acoustic wave mode. It's a composite

wave that contains two components, longitudinal wave and SV-wave, with a  $90^\circ$  phase difference. As a result, particles move in an elliptical motion with mechanical displacements occurring within 1-2 wavelengths from the surface. This is why Rayleigh waves are also known as surface acoustic waves (SAWs).

SAWs are ideal for sensing applications because the confinement of the wave's energy near the surface makes them sensitive to surface changes and perturbations. The earliest uses of SAW devices as sensors occurred in the mid to late 1970's to detect changes in pressure and temperature [31-34]. Not long after in 1979, Wohltjen [35] used SAW sensors to determine the glass transition temperature of polymer films. In the same year the first use of SAW sensors in chemical gas detection was reported [36]. In this study the adsorption of gas molecules on a polymer film changed its properties, which allowed the gas to be detected. Since that time Rayleigh SAW devices have been used in numerous gas sensing applications [37-39]. In 1983 Roederer and Bastiaans [40] reported successful immunosensing in liquids using a Rayleigh SAW mode. However, a study conducted after this work was published concluded that Rayleigh waves are not suitable for liquid sensing [41]. As a result, the standard belief in the field is that Rayleigh waves are ineffective in liquid sensing applications. What causes Rayleigh waves to be unsuitable for liquid sensing is that its longitudinal component generates a compression wave with a propagation vector that points away from the substrate, into the fluid, which causes a loss of energy [41]. In order to successfully conduct sensing in liquids, a piezoelectric material with the appropriate crystal cut that supports shear horizontal SAWs (SH-SAWs) must be selected. The reason is particle displacements for this wave mode are perpendicular to the propagation direction but parallel to the surface. Therefore, when a liquid is placed on the surface minimal attenuation occurs because the wave lacks a surface normal component.

### 2.3. SAW Biosensors

SAW biosensors allow the label free detection of an antigen in real time by monitoring changes in frequency and amplitude of a wave that result from changes in the physiochemical properties (mass density, temperature, viscosity, pH, etc.) in the area where sensing takes place. Typically biosensing occurs in a liquid environment; however, the use of wave modes with particle displacements normal to the surface (i.e. Rayleigh SAW) suffer from high losses due to the generation of compression waves within the fluid [42]. To bypass this problem an acoustic wave with particle displacements parallel to the surface needs to be utilized. A wave with this characteristic is referred to as a shear horizontal (SH) wave and it will propagate with minimal attenuation when in contact with liquid. Several different wave modes can be classified as a SH wave: thickness shear modes (TSM), acoustic plate modes (APM), surface skimming bulk waves (SSBW), Love-waves, leaky surface acoustic waves (LSAW), and Bleustein-Gulyaev (BG) waves.

Early on, acoustic wave biosensing was routinely done with TSM which propagate in quartz crystal microbalances (QCMs) [43, 44]. Even though these devices were successful for biosensing applications, their operating frequencies are only between 10-50 MHz. This is problematic because according to the Sauerbrey equation [45], sensitivity to mass loading is proportional to  $f^2$ . Therefore, to increase sensor sensitivity the operating frequency must be increased. This becomes problematic because in order to operate a QCM at higher frequencies, the plate must be made thinner. This makes the device impractical for use due to its increased fragility [46]. Thus, sensors with high sensitivity, which are required for detecting most biomarkers at clinically relevant concentrations, cannot be realized with these devices.

APM sensors that also rely on the transmission of bulk waves were developed to operate in liquid [47]. By decreasing the thickness of the substrate acoustic, waves can travel between the top and bottom surface of the substrate via multiple reflections. This configuration has a certain advantage. The IDTs used to generate the waves can be located on the opposite face from where sensing takes place. Therefore, the IDTs are never in contact with the liquid. However, there is a drawback. To operate the device, simple electronics to monitor the resonant frequency cannot be used, on the count of the simultaneous generation of several APMs with a small separation between their operating frequencies. This causes unwanted mode hopping in the preferred oscillator set-up [46].

Certain SH polarized waves (SSBW and LSAW) can be generated using the same transducer configuration as that used to generate Rayleigh waves [48]. Besides not suffering from severe attenuation in liquids, they have the advantage of a higher operating frequency than Rayleigh waves for the same transducer periodicity due their higher velocities. However, SSBW and LSAW radiate energy into the bulk of the substrate. This makes them less sensitive to surface perturbations [46, 48]. To improve their performance for biosensing applications [20, 49, 50], wave energy is confined to the surface by applying waveguide materials [12] or incorporating grating structures[10].

#### **2.4. Love Wave Biosensors**

Application of a waveguide material can improve the sensitivity of a SH-SAW sensor [51-54] (Figure 2.2). The waveguide converts SH wave modes that propagate into the bulk of the substrate (SSBW [55] and LSAW [56]) into Love waves (Fig. 2.2)[12, 13].

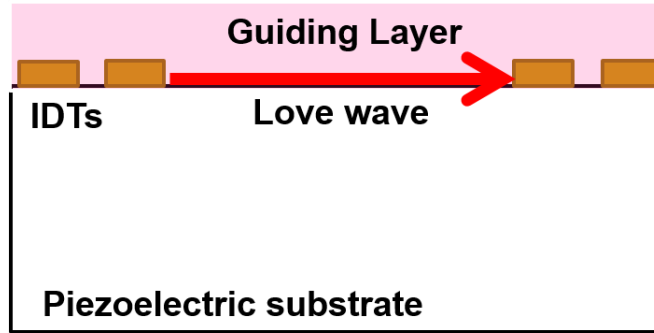


Figure 2.2 Illustration of a Love-wave sensor

To function as a waveguide the acoustic velocity in the layer must be less than the acoustic velocity in the substrate, which results in the acoustic wave being guided within the layer [12]. As a result, the acoustic losses into the substrate are minimized [46]. Initial work on Love wave sensors can be traced back to two research groups [46]. One approach carried out by Gizeli *et al.* [12], was to use a polymer waveguide layer (PMMA) deposited on ST-Quartz. It was found that the PMMA waveguide increased power transfer ( $\sim 8$  dB) and sensitivity to surface perturbations (mass loading and viscosity). Yet, the theoretically derived optimal thickness did not correlate with experimental results on account of viscous losses that occur within thicker polymer layers. Around the same time Kovacs *et al.* [13, 54] employed sputtered  $\text{SiO}_2$  as a waveguide. They found that for a given acoustic wavelength there exists an optimal waveguide layer thickness where maximum sensitivity would occur. In addition, only one Love wave mode would propagate and the electromechanical coupling coefficient would be greatest. Their results showed that a properly designed Love wave sensor would have better sensor performance than a standard SAW sensor. When these results came out in 1992, it was difficult to deposit the optimal thicknesses calculated [46, 57]. This was overcome by Du *et al.* [57, 58] in 1996 when  $\text{SiO}_2$  layers up to  $7.2 \mu\text{m}$  thick were deposited by RF magnetron sputtering. Consistent with theoretical predictions, their experimental results showed that maximum

sensitivity occurs at the optimal thickness for a given acoustic wavelength. Soon after, this Love wave device was successfully used as an immunosensor [46, 58].

Since the investigations mentioned in the previous paragraph, a variety of waveguide material have been utilized in Love wave sensors such as polymers (polyimide, polystyrene, PMMA) [53, 59], photoresists (Shipley 1813, SU8, Novolak) [52, 60, 61], dielectrics ( $\text{SiO}_2$ ) [62, 63] and piezoelectric thin films (ZnO) [64, 65]. Of these materials the most promising is ZnO. The ZnO film properties which make it appealing are high electromechanical coupling coefficient, large piezoelectric constant, biocompatibility, and most importantly, low acoustic velocity compared to common piezoelectric substrates [66]. A comparison between ZnO and  $\text{SiO}_2$  as waveguiding layers showed that ZnO was better at decreasing IL and increasing sensitivity [63, 67]. This is due not only to the lower velocity that ZnO has with respect to  $\text{SiO}_2$ , but also because of its piezoelectric nature.

## **2.5. Various Applications of SAW Biosensors**

Today there is great interest in biosensors for reliable and rapid detection of micro-organisms and pathogens for use in medicine, food safety, homeland security, and environmental and industrial monitoring [8]. Due to the beneficial properties of SAW sensors, they can be used in any of these settings. In particular, SAW sensors have been used to detect bacteria [53, 68-71], complimentary strands of DNA [72-78], viruses [20] and cancer biomarkers [22, 72, 79-81]. Use of SAW sensors for several of these applications are given in more detail in the material that follows.

### **2.5.1. SAW DNA Sensors**

A sensor that can reliably and rapidly detect single mutations within a nucleic acid can be used to discover single-nucleotide polymorphisms or mutated gene fragments. This would fulfill

a need in diagnostic applications. Genetic mutations associated with cancer can be inherited, acquired or caused by tumorigenesis. Typically DNA sensing with SAW sensors occur by immobilizing a DNA strand on its surface and measuring the response as the bound fragment hybridizes with its complementary strand [82]. Gronewold *et al.* [72], was able to accurately detect single point mutations in cancer- related gene fragments (*p53*, *ptch* and *BRCA1*). By monitoring  $\Delta\phi$ , the association and dissociation rate constants were determined for the binding of wild type and mutant gene fragments to an immobilized oligonucleotide probe. Their simple setup allowed the differentiation between wild-type sequences, and single nucleotide exchanges, or deletions on the basis of differences in dissociation rates and can therefore be used in a clinical setting. Other work in this area involves detecting oligonucleotides of different base lengths using its complementary ssDNA attached to the surface [74, 76-78]. The techniques used were highly sensitive and resulted in very low limit of detections (75 pg/cm<sup>2</sup> [50] and 136 pg/(ml Hz [74])).

### **2.5.2. SAW Bacteria Sensors**

The threats posed by biological warfare agents are an issue to soldiers on the battlefield and civilians who gather in highly public areas. Thus a need to perform quick, real-time, and accurate detection of micro-organisms on indoor air, and water or food supplies is imperative. Bacteria cells in particular pose a serious threat because they are robust, easy to deliver, and result in acute or delayed toxicity [83]. Several researchers have utilized SAW sensors for the detection of bacteria [68, 70, 83]. The detection of *E. coli* was accomplished by Berkenpas *et al* [68] using a SAW sensor fabricated on a novel substrate (langasite). Moll *et al* [83] and Deogabkar *et al* [69] also developed SAW sensing systems to detect *E. coli*. Other important work in the area was completed by Branch *et al.* [53], who used a Love wave sensor based on

36° YX LiTaO<sub>3</sub> to detect the anthrax simulant, B8 B. thuringiensis spores in an aqueous environment, below inhalation infectious levels.

### **2.5.3. SAW Sensors and Cancer Detection**

A search of the recent literature pertaining to SAW devices used to aid in cancer detection yields little results. Detection of genetic changes have shown promise in the early detection and assessment of risk for various types of cancers. For example, the identification of the alteration of several genes, *APC*, *p53*, and *K-ras*, are seen to be genetic markers for colon cancer [84]. In a previous section on SAW DNA sensors, an overview was given on the work by Gronewold *et al.* [72] on the detection of single point mutations in cancer gene fragments. A couple of research groups developed SAW sensing systems to detect breast cancer biomarkers. Guhl *et al.* [22] used a standard SH-SAW sensor based on 36° YX LiTaO<sub>3</sub> to detect HER-2/neu at a concentration of 10 ng/ml (threshold: 13-20 ng/ml). While Tigli *et al.* [80] used a novel CMOS-SAW sensor to detect the prominent breast cancer marker mammoglobin (hMAM). Another report on the successful detection of a cancer biomarker was given by Onen *et al.* [85]. This group used a SAW oscillator setup to detect the ovarian cancer marker Bcl-2 at a concentration below what is clinically required for diagnosis. Other interesting findings include an “electronic nose” to detect volatile organic compounds (VOCs) in the exhaled air of patients for detection of lung cancer [86]. Although this work is captivating it has a couple of drawbacks; this method requires a complex algorithm and uses an array consisting of many individual sensors.

### **2.6. Removal of Non-Specifically Bound Proteins**

Detection setups that require labels have higher operating costs, longer assay times compared to label-free techniques, and do not allow real time monitoring of biological

interactions [2]. It would appear that label free biosensors are superior to label detection schemes, however a major issue exists. Label-free detection schemes are not able to differentiate between a sensor response caused by the binding of analytes to specific receptors, and responses caused by material nonspecifically binding to the sensor surface [87]. Currently most reported sensing systems rely on a buffer solution containing an isolated antigen of interest to circumvent this problem. However, in real applications the antigen of interest will be present in a complex biological medium (serum, plasma, blood) which will also contain numerous interfering macromolecules [88]. For this reason, false positive clinical tests could result from the sensor's inability to differentiate between the actual response and background noise created by biofouling. Therefore, it is imperative to reduce or eliminate nonspecific binding (NSB) in order to use SAW sensors in clinical diagnostics.

NSB of proteins is caused by the hydrophobic nature of surfaces, electrostatic interactions between surfaces and partially charged biomolecules, and van-der Waals forces [89]. It was shown by Tamura *et al.* [90] that a linear relationship exists between ligand hydrophobicity and amount of NSB. Therefore, the surface needs to be modified so that it is hydrophilic and uncharged. The application of hydrophilic polymers having low affinity for protein adsorption such as poly(ethylene glycol) (PEG) [91], poly(vinyl alcohol) [92], poly(methacrylate) derivatives [93], and poly(acrylamide) [94] has been effective. However, many of these polymers have to be functionalized to introduce active sites for coupling, which increases the number of steps [95]. Another common technique to reduce NSB is to expose the antibody-coated substrates to other adhesive proteins which block adsorption sites [96]. For example, blocking proteins such as BSA or casein can be adsorbed on bare regions of the substrate to block other proteins from binding. The major drawbacks of this technique are the

expenses caused by the elaborate chemistry required and the increased assay time due to additional steps [97].

Removal of NSB proteins from a sensing surface via acoustic waves was shown using a TSM resonator [98]. According to the authors, removal occurs when mechanical stress on proteins due to the propagation of shear waves reduces the activation energy of desorption, which allows NSB proteins to be removed. In order for removal to occur, the biological film thickness must be within the wave penetration decay length,  $\delta$ , which is given by equation 2.1.

$$\delta = \left( \frac{\eta_L}{\pi f_0 \rho_L} \right)^{1/2}, \quad (2.1)$$

Here  $\eta_L$  is the fluid viscosity,  $\rho_L$  is the fluid density, and  $f_0$  is the fundamental frequency [98]. The removal of NSB was determined by measuring the fluorescent intensity of tagged proteins before, during, and after QCM operation at different input power levels. An array of 20  $\mu\text{m} \times 20 \mu\text{m}$  squares was used to differentiate between sensing and non-sensing regions. At low input power (i.e. 3.5 W) a reduction in fluorescent intensity in both areas indicated removal of loosely bound material. The authors also showed that increased removal of NSB proteins occur at higher input power (14W and 24.7W) without disrupting specific antigen-antibody binding.

Using a similar approach, Cular *et al.* [99] showed that SAWs generated on 128° YX LiNbO<sub>3</sub> can also remove NSB proteins from the sensor's surface. A micropattern between SAW transducers differentiated between sensing and non-sensing regions. The authors showed that after applying RF power NSB, proteins are removed. In addition, increasing the power resulted in more material being removed. Equally important, is that the study showed that the generated SAWs did not disrupt specific binding in the sensing regions. An issue arises because this substrate only supports Rayleigh waves, which are not suitable for sensing in liquids. Therefore,

another sensing method must be integrated if this substrate is used in a multifunctional Lab-on-a-Chip system. The solution is to use a SAW substrate that not only supports a Rayleigh wave mode, but a SH-SAW that can be used for sensing [100]. This will allow simultaneous removal of non-specifically bound proteins and sensing on the same device.

## 2.7. Finite Element Modeling (FEM) of SAW Sensors

When trying to determine if a new design is worth pursuing, a trial and error approach via experiments is too time consuming and expensive. Because of the availability of high-performance computers (HPCs) and powerful software simulation tools, computer aided design (CAD) enables rapid development of sensor designs at low cost. There are a number of different modeling techniques available for SAW designers to choose from. The proper selection depends on the physical effects one wishes to simulate, resources available, and the number of model simplifications that can be tolerated. Since only finite element modeling (FEM) was used in this work, it will be the focus of the following discussion.

Quite often models used to simulate the mechanical and electrical behavior of piezoelectric devices cannot be applied to actual designs because of simplifying assumptions that are invalid [101]. To simulate SAW sensors, the complete set of fundamental equations that relate the mechanical and electrical domains need to be solved. This can be accomplished using finite difference to handle the differential equations involved. In addition, due to the complicated geometries of SAW sensors, FE models are preferred.

Propagation of acoustic waves in piezoelectric materials are governed by the mechanical equations of motion and Maxwell's equations for electromagnetism [102]. These two systems of equations are coupled by the constitutive equations for piezoelectric materials given by [103]:

$$T_{ij} = c_{ijkl}^E S_{kl} - e_{kij} E_k, \quad (2.2)$$

$$D_i = e_{ikl} S_{kl} + \varepsilon_{ik}^s E_k, \quad (2.3)$$

where  $T_{ij}$  are components of mechanical stress,  $c_{ijkl}^E$  is the mechanical stiffness constant,  $S_{kl}$  is the mechanical strain,  $E_k$  is the electric field intensity,  $D_i$  is the electric displacement,  $e_{ikl}$  is the piezoelectric constant, and  $\varepsilon_{ik}^s$  is the permittivity constant. In the absence of internal body force the elastic behavior of piezoelectric media is given by Newton's Law

$$\frac{\partial T_{ij}}{\partial x_j} = \rho \frac{\partial^2 u_i}{\partial t^2}, \quad (2.4)$$

where  $\rho$  is mass density and  $u_i$  are components of displacement. The components of strain are defined by

$$S_{ij} = \frac{1}{2} \left( \frac{\partial u_i}{\partial x_j} + \frac{\partial u_j}{\partial x_i} \right). \quad (2.5)$$

The quasi-static assumption and the assumption that piezoelectric materials are perfect insulators helps reduce Maxwell's equations to

$$\frac{\partial D_i}{\partial x_i} = 0, \quad (2.6)$$

$$E_i = -\frac{\partial \varphi}{\partial x_i}, \quad (2.7)$$

where  $\varphi$  is the electric potential. Combination of the above equations gives a system of four coupled equations for the electric potential and the three components of displacement in piezoelectric materials [104].

$$-\rho \frac{\partial^2 u_i}{\partial t^2} + c_{ijkl}^E \frac{\partial^2 u_k}{\partial x_j \partial x_l} + e_{kij} \frac{\partial^2 \varphi}{\partial x_k \partial x_j} = 0, \quad (2.8)$$

$$e_{ikl} \frac{\partial^2 u_k}{\partial x_i \partial x_l} - \varepsilon_{ik}^S \frac{\partial^2 \varphi}{\partial x_i \partial x_k} = 0. \quad (2.9)$$

The FE approach requires discretization of the domain under study into smaller areas called elements which are connected at specific points called nodes. The coupled wave equations given in 2.7 and 2.8 can be discretized and solved to generate displacement profiles and voltages at each element or node.

The use of a FE model for an entire SAW device is not feasible unless a huge amount of computational resources and time are devoted, on account of the large number of nodes created and consequently the large number of equations that need to be solved. Different approximations can be used to reduce the FEM to a manageable level. The simplest method is to reduce the model size and subsequently the number of nodes generated. Secondly, 2-D models can be used to simplify some problems. For example, if the problem involves Rayleigh wave propagation the lateral dimension can be ignored since displacements only occur in the sagittal plane. Another approximation is to reduce the depth of the model, which will reduce the number of elements. That can be done since the SAW penetration depth is on the order of several wavelengths, so modeling the thickness of a real substrate may not be needed for a practical solution.

The use of FEMs to model wave propagation characteristics and SAW response has been shown extensively in the literature [9, 103-109]. Initial studies were focused on using FEMs to aid in device development as part of the engineering practice in industry [103]. For example, the optimization of transducer and reflector designs [110, 111]. FEMs were also useful to provide key insights when SAW devices started being used in high frequency applications. In order to

improve device performance, second order effects not relevant in low frequency applications needed to be understood [112]. Given that at low frequencies effects like electrode perturbations can be ignored because the electrode thickness to width ratio is negligible, increasing the device operating frequency makes this no longer possible [48]. Thus, the implementation of FEM models allowed designers the capability to predict the characteristic response of a SAW filter [112]. Identification and evaluation of new SAW materials quickly and without wasting valuable resource is also accomplished with FEMs. Interesting uncommon SAW materials studied are langasite [100] and a GaN piezoelectric thin film on a SiC substrate [113]. SAW sensor responses can also be modeled with FEM. Atashbar *et al.* [114] presented a 3D FE model of a SAW hydrogen gas sensor with a palladium film. In another study by Abdollahi *et al.* [107], a 3D FEM was utilized to study the mass sensitivity of SAW sensors based on a variety of substrates. The important take away from this investigation was that the authors showed the ability to quickly compare different piezoelectric substrates for sensing. It is apparent from the examples provided that FE models of SAW devices/sensors can be an indispensable tool for engineers testing the feasibility of new design ideas.

## **CHAPTER 3: SAW SENSOR DESIGN AND FINITE ELEMENT MODEL**

The creation of a biosensing system based on surface acoustic wave (SAW) devices requires careful consideration and the design of several different components. This requires an understanding of various disciplines such as chemistry/biochemistry, acoustic wave physics, electrical engineering, programming and data acquisition. This chapter serves as an overview of the different steps taken to design, fabricate and test the SAW biosensors used in this work. In addition, details of the finite element model (FEM) used for theoretical studies are provided.

### **3.1. Material Selection**

The first step in the realization of a SAW sensor is to choose a substrate. There are various substrates that one can choose from but the most common are quartz, lithium tantalate and lithium niobate. When choosing an appropriate substrate, factors such as the material's acoustic velocity, coupling coefficient ( $k^2$ ), and temperature coefficient of frequency (TCF) are important. However, if sensing is taking place in a liquid medium the most important consideration is particle polarization. To avoid excessive dissipation of acoustic energy the particles must be polarized in the shear-horizontal (SH) direction [56]. This requires a certain class of piezoelectric materials. The devices used in this work for experimental studies were fabricated on ST-quartz. This substrate was selected because it can generate Rayleigh SAW and SH-SAW by orienting the IDT pairs orthogonal to each other (Figure 3.1). When the transducers are parallel to the crystalline x axis a Rayleigh SAW will propagate. Orientation of the transducers normal to the x-axis generates a surface skimming bulk wave (SSBW) with SH

particle polarization. Utilization of quartz's ability to support both modes is of fundamental importance for the experimental investigations presented.

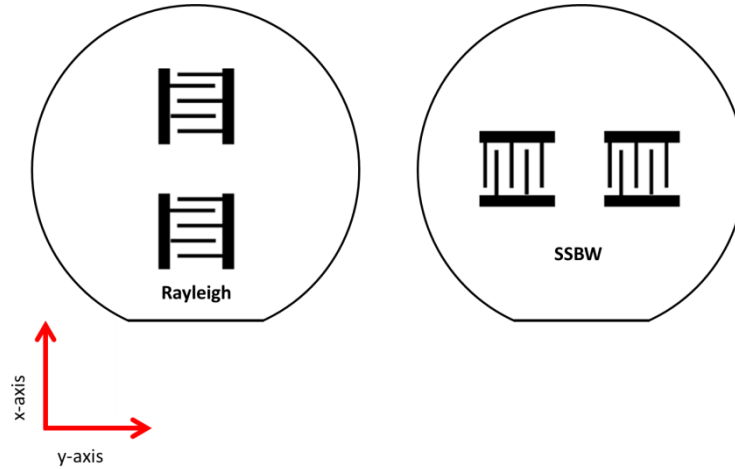


Figure 3.1 A schematic showing the different wave modes generated on ST-quartz with respect to how the IDT pairs are oriented to the crystalline x-axis (perpendicular to wafer flat)

### 3.2. IDT Design

The IDT is responsible for both excitation and detection of SAWs [28]. Since performance of the transducer is a vital aspect of how a SAW sensor will operate in an electrical circuit, which correlates to the relevancy and reliability of the output signal produced, considerable thought must go into its design. Design of an optimal IDT may take multiple iterations because the frequency, bandwidth and time response of the IDT are variables that are controlled by a number of factors: number of finger pairs, distance between input and output IDTs, aperture width, finger width, and spacing between adjacent fingers [115].

The majority of SAW devices employed as biosensors utilize a two port configuration. This requires two IDTs, one serves as the signal input and the other as the signal output. For two port designs, two options exist, a delay line and a resonator. The devices used in this study are delay line. A schematic is shown in Figure 3.2.

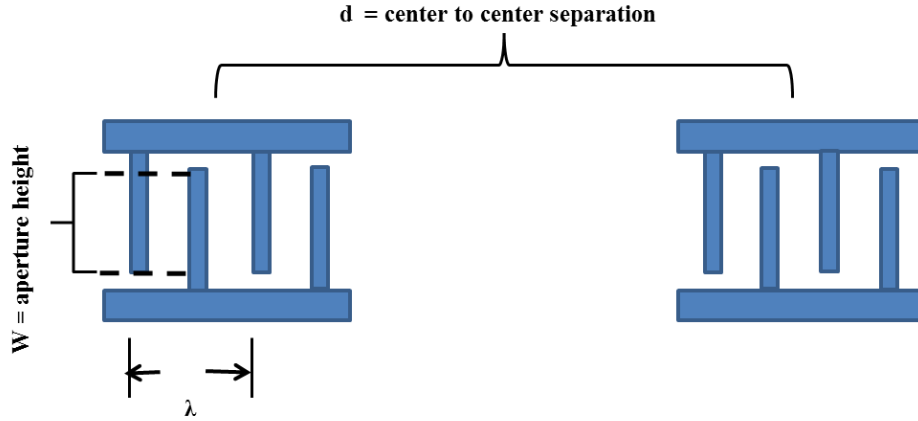


Figure 3.2 Schematic of SAW delay line with single split finger input and output IDTs

One important parameter of a SAW delay line is the distance between IDT centers ( $d$ ). To avoid direct electromagnetic coupling between the input and output IDTs should be separated by 100-300 acoustic wavelengths [116].

The simplest IDT configuration is a single split finger (SF) design with equal finger width and spacing. In this scenario the acoustic wavelength,  $\lambda$ , is given by:

$$\lambda = 4p, \quad (3.1)$$

where  $p$  is equal to the finger width. Since the SAW frequency is inversely proportional to the acoustic wavelength, operation at very high frequencies require small finger width/spacing. However, fabrication becomes difficult when dimensions become too small due to the physical limitations of photolithography. What makes operating at a higher frequency desirable is reduction in device size and increased sensitivity to surface perturbations.

For both the theoretical and experimental studies in this dissertation, I utilized the simple split finger design. In spite of its simplicity there is one inherent problem; IDTs with this configuration are bi-directional and therefore generate SAWs in opposing directions. As a result, 3 dB of loss will occur for each transducer because 50% of the power is directed away from the

intended direction. In other words, if no other loss mechanisms exist the insertion loss (IL) would be -6dB for a delay line SAW device. To overcome this problem, more sophisticated transducer designs that are unidirectional have been realized [30, 117]. Utilizing these unidirectional IDTs allows IL to be decreased beyond the -6 dB limit. Other important design parameters to consider are IDT aperture width and number of finger pairs, which determine the bandwidth of the frequency response and the impedance respectively. Table 3.1 lists the values of the parameters discussed along with the velocity for SH-SAW and Rayleigh SAW modes on ST-quartz. The device center frequency was determined by using the velocity and acoustic wavelength ( $\lambda$ ).

Table 3.1 Relevant SAW parameters used in device designs for theoretical and experimental studies

Parameter	SH-SAW Value	Rayleigh SAW Value
Velocity	5060 m/sec	3158 m/sec
Wavelength ( $\lambda$ )	40 $\mu\text{m}$	40 $\mu\text{m}$
Center frequency ( $f_0$ )	126.5 MHz	78.95 MHz
# finger pairs (input/output)	60	60
Aperture (input/output)	50 $\lambda$	50 $\lambda$
Center to Center Distance	200 $\lambda$	200 $\lambda$

### 3.3. Device Fabrication

SH-SAW and Rayleigh SAW devices were fabricated on ST-X quartz wafers, 0.5 mm thick and 4-inches in diameter. To prepare the wafers for processing, they were thoroughly cleaned to get rid of any contamination by using a solvent clean (acetone, methanol and IPA), followed by a DI rinse and drying with N<sub>2</sub>. Patterning of each wafer was done by standard photolithography. The input and output IDTs were composed of a 20 nm Ti adhesion layer and a 100 nm thick Au film. Excess metal was removed by lift-off in acetone. An overview of the process flow is shown in Fig. 3.3.

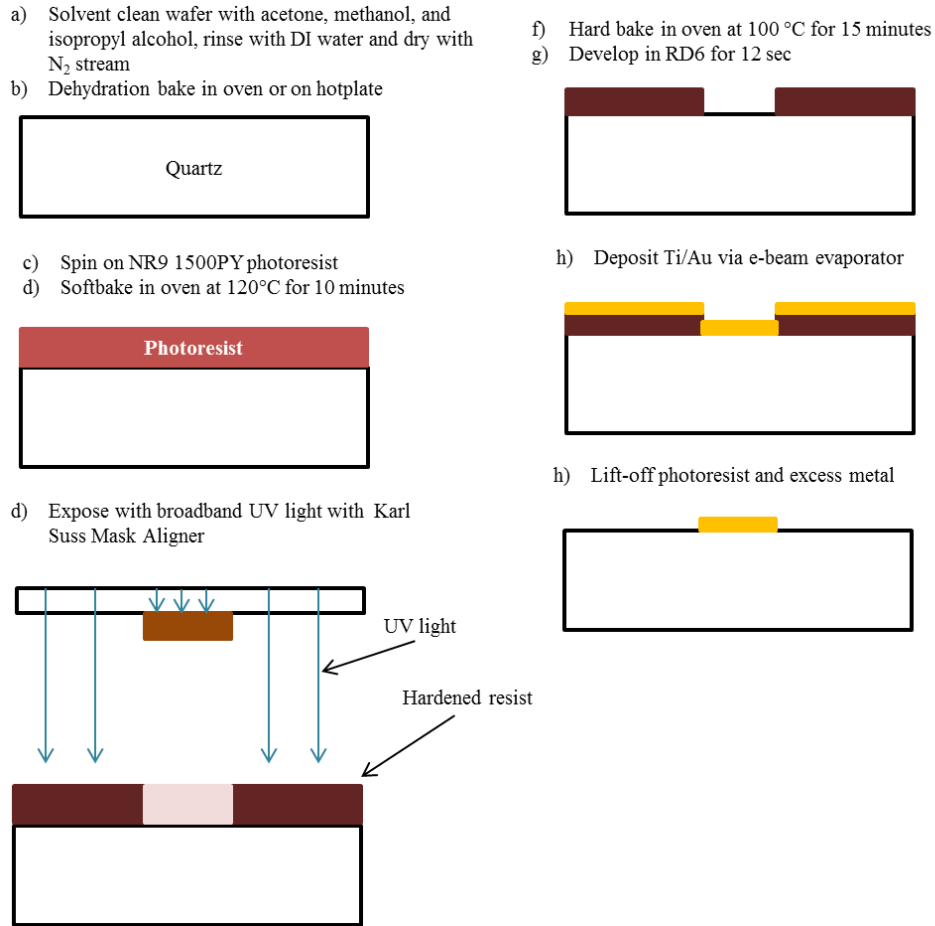


Figure 3.3 Process flow used in the fabrication of SAW devices on ST-quartz

### 3.4. Measured SAW Frequency Response

To verify if the SAW device was designed correctly and if the fabricated devices are working as expected, the frequency response was measured to find the center frequency. For each wave mode (SH-SAW and Rayleigh SAW) its center frequency can be calculated using the IDT periodicity and the corresponding acoustic velocity. Measured values are compared with those calculated to determine if each device is working properly. The frequency response was measured using an Agilent 8753 ES network analyzer. Figure 3.4 shows the measured frequency responses. Theoretical calculations were based on each mode's acoustic velocity (Rayleigh =

3158 m/sec and SSBW = 5060 m/sec) and acoustic wavelength ( $\lambda = 40 \mu\text{m}$ ). Comparisons between measured and theoretical values are shown in Table 3.2.

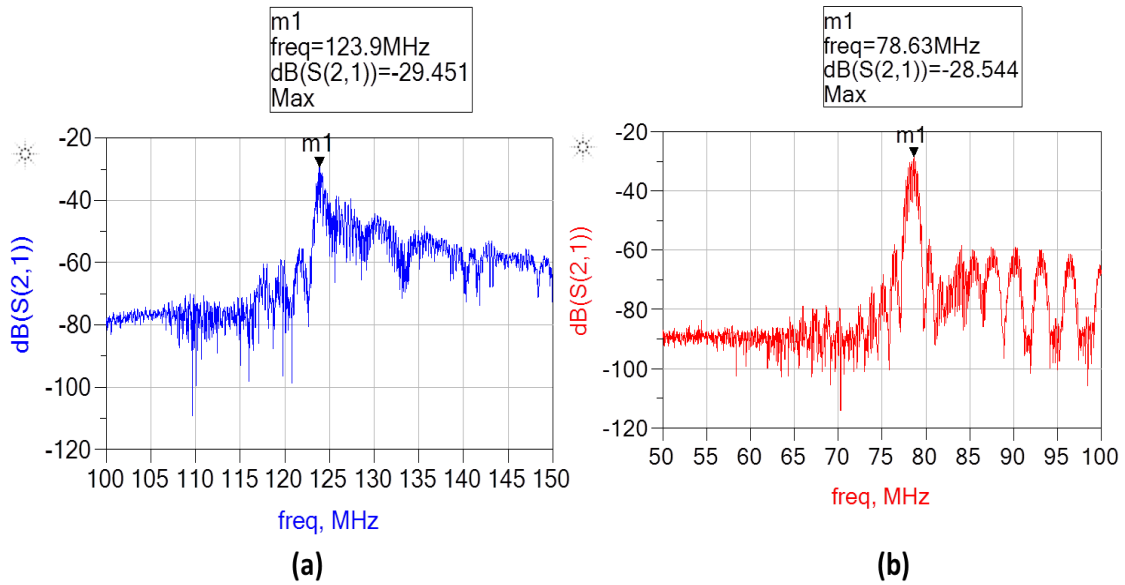


Figure 3.4 Frequency responses for (a) SH-SAW mode and (b) Rayleigh mode

Table 3.2 Comparison between theoretical and measured center frequency for each wave mode used

Wave mode	Theoretical Center Frequency ( $f_0$ )	Experimental Center Frequency ( $f_0$ )
SSBW	126.5 MHz	123.9 MHz
Rayleigh	78.95 MHz	78.65 MHz

Discrepancies between measured and theoretical values are due to mass loading of the IDTs and misalignment of the transducers with the crystalline axes (x and y-axis). Since IDT mass loading for the transducer thickness deposited only results in a negative frequency shift; it will not adversely affect device operation. However, improper alignment of the IDTs with the crystalline axes (x or y-axis) results in increased IL, which hurts sensor performance.

### 3.5. Application of a Waveguide

ST Quartz is known to support a surface skimming bulk wave (SSBW) [118]. This wave mode has SH particle displacements (parallel to the surface and perpendicular to the propagation direction), so it is suitable for liquid sensing. However, as the wave travels from the input IDT to the output IDT, it starts to propagate into the bulk of the substrate. The diminished wave energy at the surface decreases the sensor's sensitivity to perturbations. To improve its sensitivity a waveguide layer can be applied which converts an SSBW in Quartz to a Love Wave [12, 13]. There are various wave guide materials that can be used such as polymers (polyimide, polystyrene, PMMA) [53, 59], photoresist (Shipley 1813, SU8, Novolak) [52, 60, 61], dielectrics ( $\text{SiO}_2$ ) [62, 63] or piezoelectric thin films (ZnO) [64, 65].

There are several factors to consider before choosing a waveguide. First, the acoustic velocity of the layer must be smaller than the shear velocity of the substrate [12, 13]. When this condition is met, the layer slows down the acoustic velocity of the shear mode in the substrate. As a result, the penetration into the substrate is decreased and the wave is confined at the surface (Figure 3.5) [13]. For a given waveguide thickness, the confinement of the wave energy to the surface can be enhanced when the difference between waveguide and substrate velocities is large. Equally important to waveguide effectiveness is the thickness of the guiding layer. For instance, a waveguide with a thickness much smaller than the SAW wavelength has more energy confined within the substrate compared to a waveguide in which the thickness approaches the SAW wavelength [57]. In this case, the wave energy is more concentrated in the waveguide layer. Other factors to consider when choosing a waveguide material are its resistance to chemical attack, ability to be modified with functional groups for conjugation with biomolecules, and biocompatibility. Not to mention, materials such as polymers contribute losses due to

acoustic adsorption when the layer becomes too thick [57]. Therefore, film thickness must be carefully monitored for these materials.

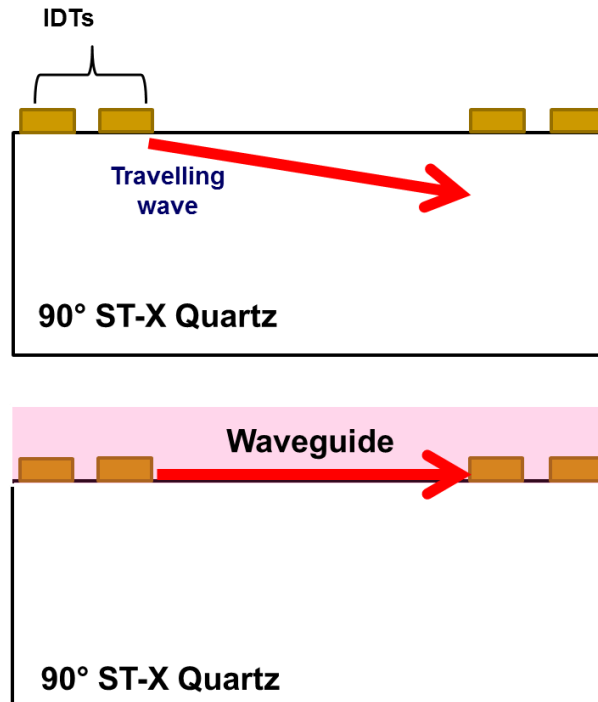


Figure 3.5 Illustration of how a SSBW is converted to a Love-wave when a waveguide material is applied to the sensor surface.

Novolac photoresist was chosen as the waveguide material to be used in studies where it was required. It was chosen due its low shear acoustic velocity, ease of deposition and patterning, and resistance to chemical attack. The following is the procedure used to add the waveguide layer to the sensor. Prior to waveguide deposition, the ST-Quartz wafer patterned with the SAW transducers was cleaned by rinsing with acetone, methanol, isopropanol, and DI water, then dried by an N<sub>2</sub> stream. This was followed by placing the wafer in O<sub>2</sub> plasma for 10-15 minutes to remove organic contamination. A Novolac based photoresist (AZ 1512, AZ Electronic Materials) was spun on the ST-Quartz substrate at 4000 rpm for 40 sec. Next the resist was soft baked by being placed on a hotplate, set at 115 °C, for 1 min. Exposure to broadband

UV for 3 sec at an intensity of 25 mW/cm<sup>2</sup> followed. Finally to open up windows to the underlying bond pads the wafer was immersed into AZ 726 developer (Microchemicals) for 30 sec. To remove any remaining solvent and to promote cross-linking of the polymer, the wafers were placed in an oven for 2 h at 190 °C. Waveguide thickness measurements were made with an Alphastep profilometer. The average measured thickness was approximately 0.8 μm.

One way to determine if the SSBW in Quartz is converted to a Love wave is to compare the device's IL before and after deposition of the waveguide [12]. A decrease in IL is verification that more energy is being confined to the surface. Figure 3.6 shows a typical result when a Novolac waveguide with a thickness of approximately 0.8 μm is used.

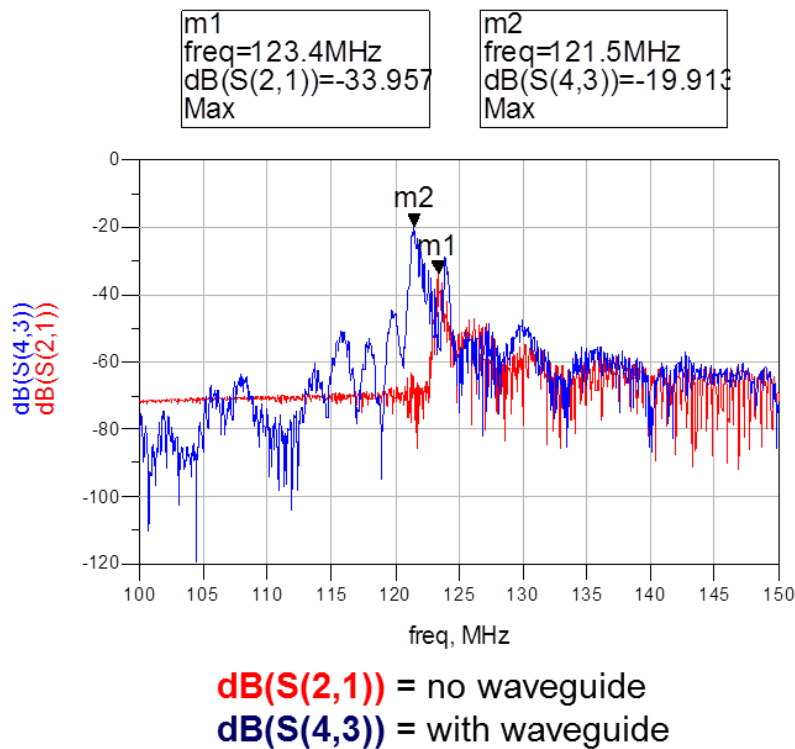


Figure 3.6 Comparison of the frequency responses for an ST-quartz sensor without a waveguiding layer (red) and with a waveguiding layer (blue)

As a result of applying the Novolac waveguide, the IL was decreased by 14.044 dB. In addition, there was a slight decrease in the acoustic velocity from 4936 m/sec to 4860 m/sec. The decrease in velocity was expected because the presence of the waveguide slows down the shear wave in the substrate and confines it the surface. These results indicate that the SSBW mode is converted to a Love wave as expected.

### **3.6. Immobilization of Biorecognition Elements**

A critical aspect of sensor development is the integration of a biorecognition layer with the transducer. For SAW sensors, this is typically done by immobilizing a biomolecule that has high specificity for the intended target. It is imperative that this step in the process is done correctly because it directly affects the sensor's specificity, sensitivity and reproducibility. There are various methods that have been reported in the literature to immobilize a biorecognition element which include physical adsorption [53, 119], covalent binding [120-122], and entrapment in a 3-D matrix [123, 124]. A description of the two immobilization methods used in this work is given below.

#### **3.6.1. Physical Adsorption**

When the sensor surface consists of the following combinations, piezoelectric substrate/waveguide/gold film or piezoelectric substrate/gold film, the method used to attach the sensing film is physical adsorption (Figure 3.7). Physical adsorption of proteins onto a surface occurs via electrostatic and hydrophobic interactions, and van der Waals forces [125]. This is the easiest and quickest way to immobilize proteins onto a deposited gold film. However, the biosensing layer is not reproducible and reliable. Therefore, if the sensors used in this study are to be commercialized then another immobilization method should be implemented. In any case, the process begins by allowing protein A, which has a large affinity for gold [51], to physically adsorb onto the surface from solution. Protein A is used because it has two binding sites specific

to the Fc region of IgG antibodies [119]. Thus, the antibody is oriented in such a way that its binding site is easily accessible. By simply ensuring that antibodies are oriented in this way, sensor performance can be improved as high as 200 fold [126]. The remaining component of the sensing layer is the capture antibody which will bind its target with high selectivity.

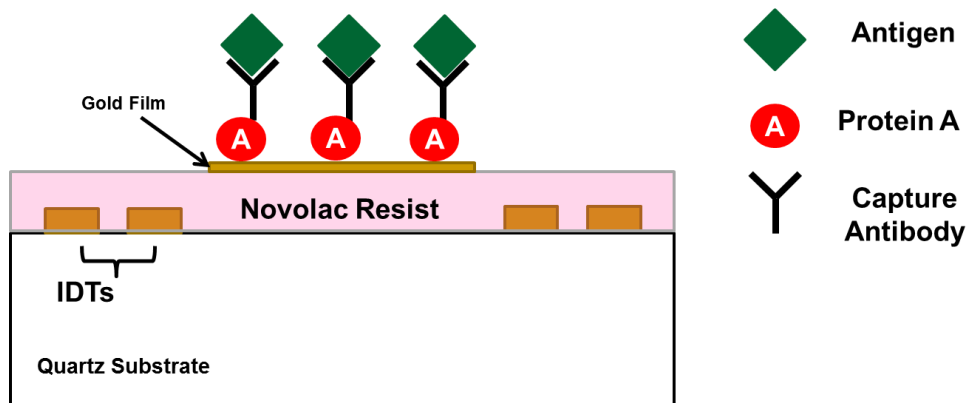


Figure 3.7 Illustration of the biosensing layer used when the sensor has the following configuration: piezoelectric substrate/waveguide/gold film.

### 3.6.2. Covalent Immobilization Using Silane Chemistry

Covalent attachment of biomolecules offers several distinct advantages over physical adsorption such as the formation of ordered structures at the molecular scale, the ability to have access to numerous functional groups, and stable attachment of biorecognition elements [127]. When investigations were conducted with sensors that didn't possess a waveguide and a gold film, (3-glycidoxypropyl) trimethoxysilane (3-GPS) or (3-glycidoxypropyl) dimethylethoxysilane (3-GPDMS) was used to covalently attach antibodies to the surface. This organosilane was chosen over other popular cross-linkers like (3-aminopropyl) trimethoxysilane because of its reported robustness and ease of chemistry [128]. The end functional group of 3-GPS contains an epoxide ring which is reactive towards nucleophiles such as amines, thiols, and

hydroxyls [129]. The relative reactivity of epoxide is thiol > amine > hydroxyl. For functional groups with low reactivity, the pH can be made higher to increase efficiency [129].

To modify the surface with 3-GPS (Sigma Aldrich), a 1 v/v % in toluene solution was prepared. First, the sensor chip was cleaned by rinsing with acetone, methanol, and isopropyl alcohol and then sonicating in ethanol for 10 minutes. Then the device was rinsed with ethanol and blown dry with N<sub>2</sub> before placing in an oven for 15-30 minutes at 110 °C to ensure the sensor surface was dry. After baking in the oven the devices were put in a Harrick plasma cleaner for 10-15 minutes on the medium setting. Upon removal from the plasma cleaner the sensor chip was placed in the 3-GPS solution and left covered for 15-20 minutes. Next, the device was rinsed with toluene and blown dry with N<sub>2</sub>. In the final step the chip was placed in an oven for 30 min at 110 °C for 30 min to complete the reaction.

The deposition of a 3-GPS layer was confirmed by water contact angle measurements. To measure the water contact angle, a small drop of DI water was applied to the surface with a Hamilton syringe. A KSV CAM 100 optical goniometer was used to measure the contact angle. Figure 3.8 shows an illustration of a SAW sensor modified with a 3-GPS layer for biosensing.

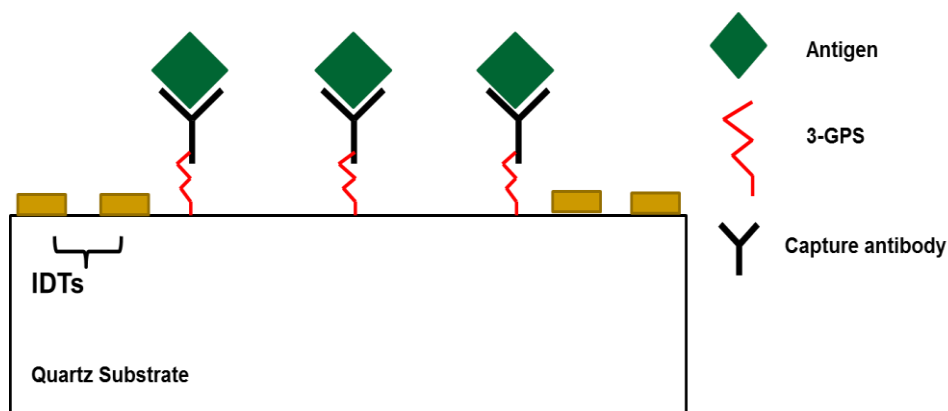


Figure 3.8 Illustration of the bare ST-quartz substrate modified with a 3-GPS layer to covalently attach antibodies for biosensing.

### 3.7. Integration of a Microfluidic Device with a SAW Sensor

When developing a biosensor platform that will handle liquid samples, proper design of a flow cell is extremely important so that noise levels are reduced and stability is enhanced [130]. Both of these aspects contribute to improving the limit-of-detection of the sensor platform. To deliver reagents to the delay path, we used a PDMS microfluidic device. The process of making the mold and the PDMS device can be found in numerous places in the literature [131, 132]. To minimize excessive damping of the acoustic wave, the wall thickness in contact with the SAW delay path must be optimized as well as the area exposed to the sample during sensing. PDMS can seal itself irreversibly to surfaces that are Si based materials which have been oxidized because a covalent O-Si-O bond is formed [132]. This would apply for ST-Quartz SAW sensors. However, permanent attachment of the PDMS device is not possible when the SAW sensor has been modified with a waveguide layer and gold film because Si-O bonding is no longer possible. Therefore, a machined acrylic piece allows pressure to be applied on top of the PDMS device had to be utilized to keep it in constant contact with the surface. A 2-D schematic of one of the microfluidic devices developed is shown along with the SAW IDTs in Figure 3.9.

Equation 2.1 gives the penetration depth,  $\delta$  [m], of a shear wave in contact with a liquid, which is a function of liquid viscosity,  $\eta_L$  [Pa s], liquid density,  $\rho_L$  [kg m<sup>-3</sup>], and SAW frequency,  $f_0$  [s<sup>-1</sup>]. In order to avoid interference with the moving fluid, this parameter is used to determine the height of the channel [133]. For an operating frequency of approximately 125 MHz and water as the liquid, the penetration depth is 50.46 nm. Therefore, the channel height was designed to be 100  $\mu$ m. Two air cavities were placed above the IDTs to avoid attenuating generated waves and their height was also 100  $\mu$ m. In addition, the channel width is 1500  $\mu$ m and the wall thickness in contact with the delay path is 100  $\mu$ m.

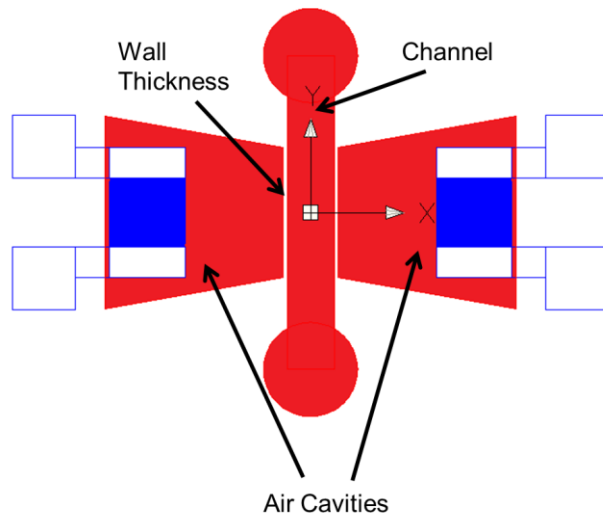


Figure 3.9 Illustration of microfluidic device design for a SAW sensor chip. The design includes the channel and air cavities above the IDT (red). PDMS wall thickness is the white space between the air cavities and the channel.

To ensure that the PDMS device was designed properly to allow sensing in liquids to occur, the transmission characteristics of the SAW device was measured under three different conditions. The first condition was without the microfluidic device, the second was with the microfluidic device, and the third was with the microfluidic device with liquid in the channel. The frequency response for each condition is shown in Figure 3.10.

The base line for comparison is the measured frequency response of the bare ST-quartz sensor, which shows the device center frequency at 124.2 MHz with -29.352 dB IL. Loading the sensor with the microfluidic device shifted the center frequency to 123.9 MHz and decreased IL by 0.275 dB. The decreased center frequency is expected because the loaded surface would decrease the acoustic velocity. What is not expected is the decrease in IL. Another study in which a SAW sensor is combined with a microfluidic device also showed a slight decrease in IL [134]. From this report a possible explanation can be derived; the decreased IL was due to the

PDMS walls reducing reflections that destructively interfere with the main signal. When fluid was inserted in the channel the center frequency shifted upwards ( $\Delta f_0 = 0.3$  MHz) and was accompanied by a further decrease in IL ( $\Delta IL = 0.105$  dB). Since the measurements shown in Figure 3.10 are done on bare ST-Quartz, an acoustoelectric interaction occurs when the surface is in contact with a liquid. More specifically, when a metal film is not present on the surface the piezoelectric potential generated along the surface from the propagating SAW penetrates into the liquid. Thus, the dielectric and conductivity properties of the liquid cause changes in SAW amplitude and velocity. The results from Figure 3.10 suggest that the acoustoelectric interaction causes an increase in wave velocity and amplitude. Similar results were obtained using several different devices as long as the IDTs were protected from the liquid. As can be seen from the results in Figure 3.10, a microfluidic device capable of delivering a liquid sample to the delay path of a SAW sensor has been successfully designed.

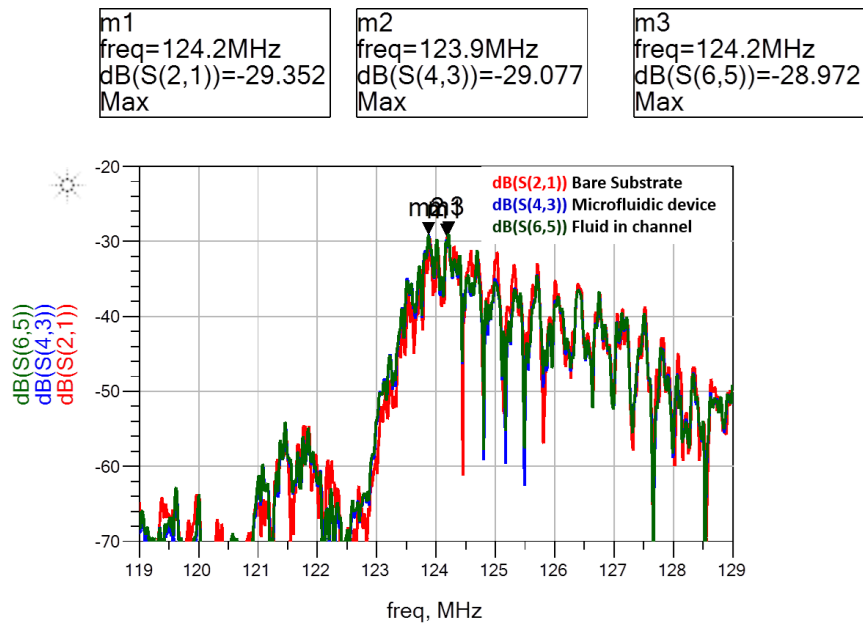


Figure 3.10 Frequency response curves for an ST-quartz sensor under three conditions. The red curve is the sensor by itself. The blue curve is the sensor loaded with the microfluidic device. The green curve is the sensor loaded with the microfluidic device and with DI water inside the channel.

### 3.8. Measurement Setup for Orthogonal SAW Experiments

The experimental focus of this dissertation is to perform removal and sensing on the same device. Therefore the measurement setup related only to those experiments is given. Performing removal and sensing simultaneously required placing the SAW IDTs orthogonally to each other to generate two different wave modes. The first wave mode considered is a Rayleigh wave, which has particle displacements normal to the surface and will be used for biofouling removal. The other wave mode is a SSBW, in which particle displacements are parallel to the surface and normal to the direction of propagation. It will be used for sensing. A schematic of the orthogonal SAW chip is shown in Figure 3.11.

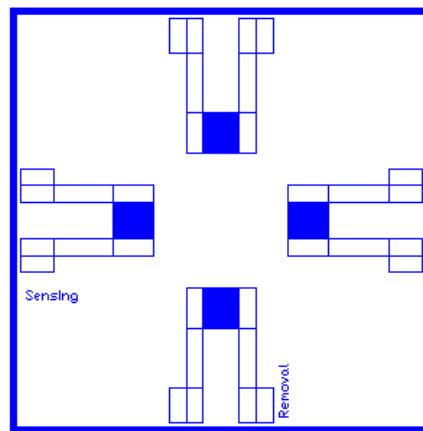


Figure 3.11 Schematic of a SAW sensor with orthogonally placed transducers.

The measurement setup is illustrated in Figure 3.12. Initially the devices were characterized using an Agilent 8753ES network analyzer (Agilent) to verify if Rayleigh and SSBW modes were being generated. For sensing and removal experiments, the network analyzer provided the input signal for the sensing direction and was used to monitor the phase and IL at a fixed frequency. A PC connected to the network analyzer via a GPIB interface running a custom LabView program (LabVIEW 2010, National Instruments) was used for instrument control and

to acquire data by sampling and recording the phase of the  $S_{21}$  signal at discrete time steps. In the removal direction, an SMA 100A signal generator (Rhode & Schwarz) applied the RF input which was split using a Z99SC-62+ 2-way  $0^\circ$   $50 \Omega$  power splitter (Mini-Circuits). This allowed the excitation of both IDTs. For experiments that required higher power, a TIA RF amplifier (Mini-Circuits) was inserted in the path between the signal generator and power splitter.

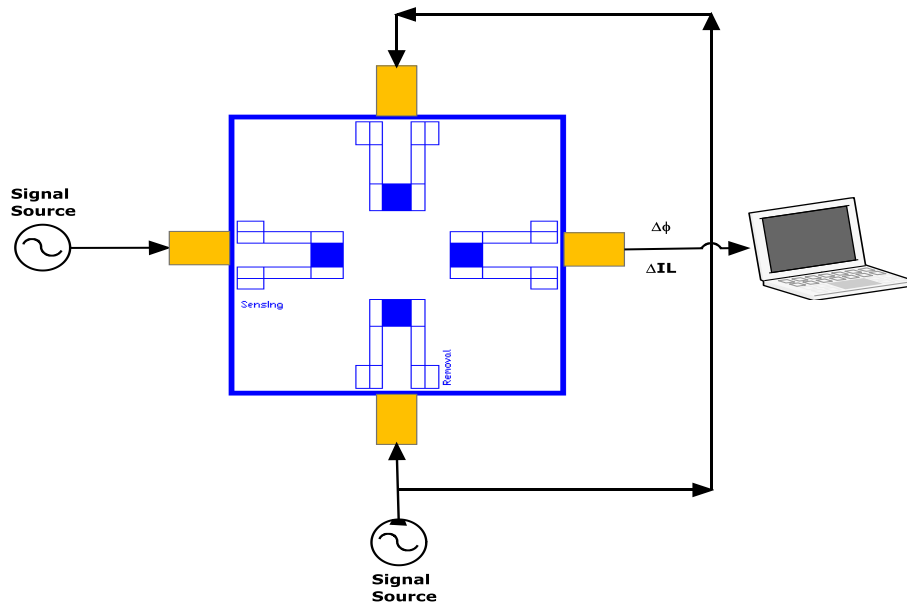


Figure 3.12 Illustration of measurement setup for removal and sensing experiments.

Samples were introduced to the SAW delay path by two different methods. One method was to place a drop of the liquid sample directly on the delay path. Use of an o-ring prevented the liquid droplet from spreading. The second method was to employ a microfluidic device for sample handling. In this scenario the liquid was delivered using a Harvard PHD 2000 syringe pump (Harvard Apparatus).

### 3.9. Finite Element Model (FEM) of SAW Sensor

A 3-D structural finite element model (FEM) of a SAW device was prepared in ANSYS and is shown in Figure 3.13. The model represents a two-port delay line SAW device with

substrate geometry of 1600 $\mu\text{m}$  length, 200  $\mu\text{m}$  width, and 500  $\mu\text{m}$  depth. The depth was chosen to represent the thickness of an actual SAW substrate, while the length was chosen to limit the amount of reflections from the substrate edges. The coupled field element Solid 226 is used in the simulation. To mesh the 3-D structure, tetrahedral elements having 4 degrees of freedom (DOF) are used. Three of the DOFs define displacements in the x, y, and z directions. The fourth DOF is voltage. To reduce the number of nodes generated, a non-uniform mesh was used, with a larger meshing density near the surface and towards the center. Both the input and output IDTs are composed of three finger pairs having a periodicity of 40  $\mu\text{m}$  and aperture width of 60  $\mu\text{m}$ . To simplify the analysis, the IDT fingers were defined to be mass-less elements, represented by a set of nodes coupled through the voltage degree of freedom (DOF). This allowed second order effects due to mass loading to be ignored. The distance between the IDTs ( $4\lambda$ ) sets the delay path length.

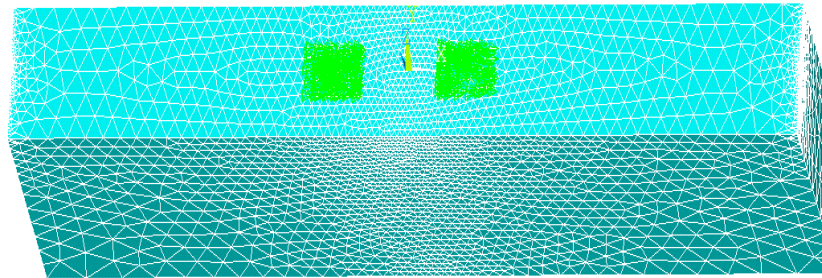


Figure 3.13 Image of the SAW delay line model used in ANSYS FEM simulations.

The SAW frequency response was obtained by taking the Fourier transform of the impulse response. To obtain the impulse response, an impulse voltage signal, having amplitude of 100 V, is applied to the transmitting IDT. The structure was simulated for 200 ns using a time

step of 0.95 ns. Once the analysis is complete the output voltage from one of the nodes on the output IDT is recorded vs. time. The voltage vs. time data is converted into the frequency response by applying an FFT algorithm using a custom Matlab code.

The frequency response obtained for the SSBW on ST-Quartz is shown in Figure 3.14. To validate that the proper wave mode was being simulated the theoretical center frequency was compared to the one obtained from simulations. For an IDT periodicity of  $40\ \mu\text{m}$  and a SAW velocity of  $5060\ \text{m/sec}$ , the theoretical center frequency is  $126.5\ \text{MHz}$ . Analysis of the frequency response shown in Figure 3.14 indicates the simulated center frequency was  $126.63\ \text{MHz}$ . This value is in close agreement with the theoretical value for this substrate and orientation.

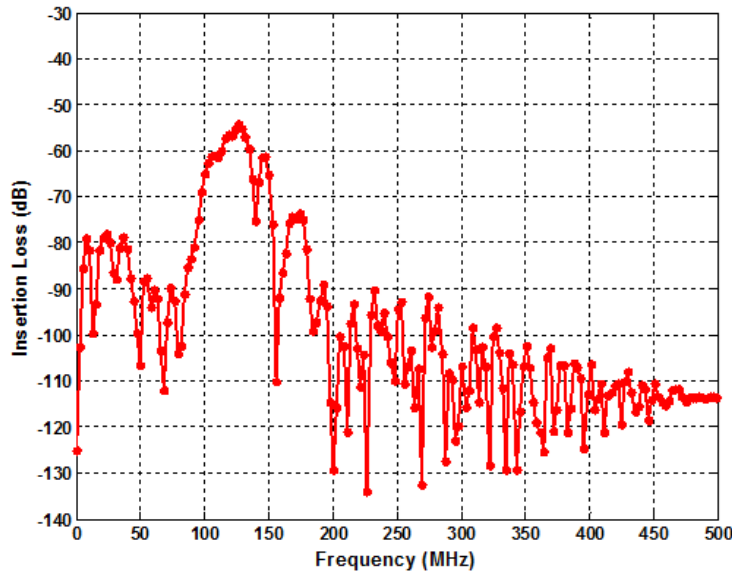


Figure 3.14 Simulated frequency response of the SSBW on ST-quartz using ANSYS.

Further validation is obtained by looking at displacements associated with the wave generated. Nodes on the output IDT were selected and the average displacements in the x, y, and z directions were plotted vs time. Figure 3.20 shows the SH-displacement (x direction),

longitudinal displacement (y direction) and surface normal displacement (z direction). From the figure it is apparent that displacements are more prominent in the x direction (SH displacement).

This is indicative of SSBW propagation.

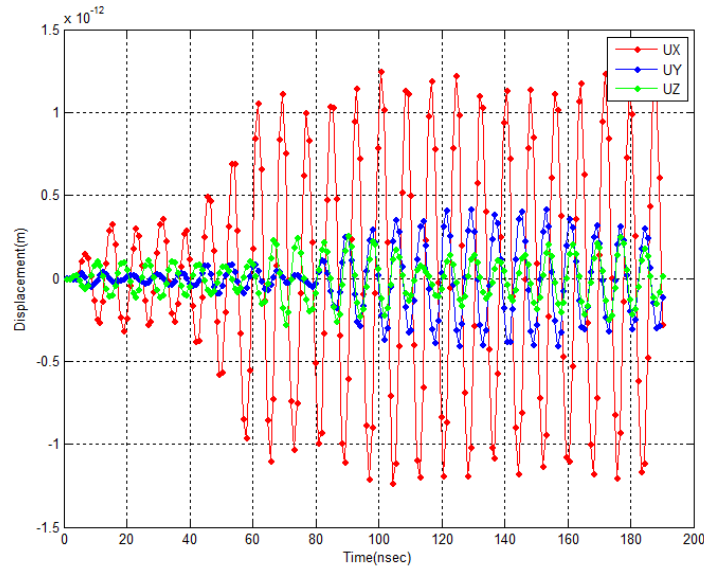


Figure 3.15 Simulated nodal displacements at the output IDT for SSBW propagating in ST-quartz.

Acoustic wave propagation characteristics in terms of displacement contours and mass loading data were obtained by doing an AC analysis at the device center frequency acquired from the impulse response. For each device configuration, an AC voltage with amplitude of 2.5 V at a frequency,  $f_0$ , was applied to the input IDT, using a time step of 0.95 ns and a duration of 200 ns.

## **CHAPTER 4: LOW INSERTION LOSS AND HIGHLY SENSITIVE SH-SAW SENSORS BASED ON 36° YX LiTaO<sub>3</sub> THROUGH THE INCORPORATION OF FILLED MICROCAVITIES<sup>1</sup>**

Reduction in power consumption and improvement in mass sensitivity are important considerations for surface acoustic wave (SAW) devices used in various sensing applications. Detection of minute quantities of a particular species (clinical sensing) and power requirements (wireless sensing) are two key metrics that must be optimized. In this study, a three-dimensional (3-D) finite element model (FEM) was employed to compare insertion loss (IL) and mass sensitivity of SAW sensors having microcavities filled with ZnO and nanocrystalline diamond (NCD) to a standard two-port SAW design. Initial simulation results show that ZnO filled cavities (depth = 5 $\mu$ m) were most effective at reducing power loss ( $\Delta$ IL = 6.03 dB) by increasing particle displacement (acoustoelectric to mechanical transduction) at the output transducer. A 100 pg/cm<sup>2</sup> load was applied to the sensing area of each device to evaluate mass sensitivity. Our simulations suggest that ZnO filled cavities with shallow depth (2.5  $\mu$ m) have the greatest sensitivity. The FEM simulations are used to understand the acoustic wave propagation in microcavity based SAW sensors. The observed enhancement in mass sensitivity and power transfer are attributed to waveguiding effects and constructive interference of the scattered acoustic waves from the microcavities. Devices fabricated with microcavities  $\sim$  1  $\mu$ m deep

---

<sup>1</sup>Copyright © 2015, IEEE. Reprinted, with permission, from M. Richardson, S. K. R. S. Sankaranarayanan, and V. R. Bhethanabotla, "Low Insertion Loss and Highly Sensitive SH-SAW Sensors Based on 36° YX LiTaO<sub>3</sub> Through the Incorporation of Filled Microcavities," *Sensors Journal, IEEE*, Feb. 2015. Permission is included in Appendix A.

decreased IL by 3.306 dB compared to a standard SAW device. Additional simulations were conducted for each device configuration using the same depth in order to make a direct comparison between measured and simulated results. Our findings offer encouraging prospects for designing low insertion loss, highly sensitive microcavity based SAW biosensors.

#### **4.1. Introduction**

Surface acoustic wave (SAW) devices can be used as direct, label free biosensors to monitor the interaction between a receptor and its target in real time, through changes in the properties of the traveling wave (i.e., frequency, velocity, and amplitude) [20, 53, 135, 136]. An ideal biosensor will be selective to the species of interest, robust, have high sensitivity, and consume a small amount of power. Thus, key challenges for developing efficient biosensors include factors such as selectivity, sensitivity, and power consumption.

With the increasing use of biosensors in clinical applications to aid in the early diagnosis of disease, the sensing of clinically relevant biomarker concentrations has become a key area of focus. A recent study by Gruhl *et al.*, serves as a prime example where the detection of the breast cancer marker HER-2/*neu* at a concentration of 10ng/ml was marginally within the cut-off value (13-20ng/ml) for diagnostic applications [22]. Early detection of biomarkers remains a major problem because the initial biomarker concentrations in the blood are typically lower than the current detectable limits (ng/ml) of SAW biosensors. This is especially true for a disease like colorectal cancer, where patient survival is directly related to early detection. Another objective of current sensor research is addressing how to move biosensing from a clinical laboratory that requires expensive bulky equipment and highly skilled personnel, to point-of-care testing (POCT). An example would be a wireless sensor that can monitor a physiological signal, such as blood glucose levels in a patient [137]. A major challenge to the incorporation of wireless

sensors for biosensing/medical applications is power consumption. Currently most devices are battery operated. So, a portable system that consumes less power or is totally passive is required.

Power consumption in a portable SAW device remains a major problem and depending on the substrate used, the losses can be as high as 10-30 dB. In existing SAW based technologies, the common methods of decreasing insertion loss include the incorporation of reflective gratings [10], grooves and corrugated surfaces [11], the application of waveguide materials [12], and optimization of transducer designs that support unidirectional wave propagation [138]. In all of these methods, the underlying physics involved in reducing the SAW device power loss stems from the efficient conversion of bulk waves into surface waves and enhanced entrapment of energy near the surface that would otherwise be lost to bulk waves.

For biosensing applications, SAW based on  $36^\circ$  YX LiTaO<sub>3</sub> are widely used because it generates shear-horizontal waves that propagate with minimal dissipation of energy to a liquid at the surface. In addition,  $36^\circ$  YX LiTaO<sub>3</sub> has a high electromechanical coupling coefficient ( $k^2$ ) and a relatively low temperature coefficient of delay (TCD)[139]. The wave mode generated for this substrate is a leaky SAW (LSAW), which penetrates into the bulk of the substrate during propagation. This causes the device to be less sensitive to perturbations at the surface. It has been reported that sensitivity of SAW based sensors can also be improved through the addition of a guiding layer to create Love-wave devices. Application of guiding layers with acoustic velocities less than that of the substrate convert LSAW to Love waves [20, 53]. This increases energy confinement at the surface and improves its sensitivity. Recently, we have demonstrated that a micro-cavity based SAW sensor holds the promise to positively impact sensitivity and power consumption [9, 140]. Motivated by these findings, further investigations on the use of microcavities with different SAW substrates and wave modes are warranted.

In this work, we introduce an improved micro-cavity based sensor design that is much more sensitive to mass loading and consumes far less power than currently used SAW sensors including our previously reported micro-cavity based devices. The dramatic improvements reported in sensitivity and power consumption in this work are brought about by filling the micro-cavities with piezoelectric material such as ZnO and material with high density/stiffness such as nanocrystalline diamond (NCD) in the delay path. In particular, we use a Finite Element Method (FEM) to compute power consumption and mass sensitivity for a given sensor configuration. We systematically evaluated and compared the performance of several different SAW device configurations based on air, ZnO and Diamond filled microcavities to determine a design that will yield the best sensor performance. The use of FEM offers several distinct advantages in designing sensors which employ complex geometries (such as microcavities). Using a FEM, we were able to compare IL and sensitivity to mass loading of a clinical relevant concentration ( $100\text{pg}/\text{cm}^2$ ) without employing complex analytical techniques and avoiding the costs associated with fabricating many devices. The FEM approach also allowed us to gain a fundamental understanding of the acoustic physics underpinning our results. In addition, we present a fabricated SAW device with microcavities etched in the delay path. Comparison of the frequency responses between a bare SAW sensor and one that contains cavities shows how power consumption is affected. The experimental findings are also shown to corroborate simulations and prove that actual devices can be realized.

## **4.2. Computational Details**

### ***4.2.1. Choice of Substrate, Geometry and Materials***

SAW sensors with an array of microcavities in the delay path having square cross-sectional areas,  $\lambda/2 \times \lambda/2$ , with  $2.5\ \mu\text{m}$  and  $5\ \mu\text{m}$  depths were evaluated. The dimensions of the

microcavities simulated in this work are chosen keeping in mind the practical limitations. Due to the issues associated with etching holes in  $\text{LiTaO}_3$  because of the moderately slow etch rates compared to that of other materials, the depths chosen ensure the future fabrication of devices. Previous simulations have been done on microcavity/SAW structures with an isotropic filling material (polystyrene) [9]. However, the emphasis was placed on the combined effect of mutually interacting IDTs and microcavities [140], or only one filling material was studied [99]. In this work, we studied the effect different filling materials have on acoustic wave propagation and how this correlates to power transfer and device sensitivity. This includes a more thorough examination of why power transfer is increased and how an acoustic wave interacts with the array of microcavities. In addition, preliminary experimental results are included which show the addition of microcavities without filling material can improve power transfer. There exists several candidate filling materials that we could have studied. For example,  $\text{SiO}_2$  has been readily used as a waveguide material for Love wave sensors [13, 57, 58]. The application of an  $\text{SiO}_2$  guiding layer increases sensitivity [13, 57, 58], decreases IL [53] and presents a positive temperature coefficient of frequency (TCF) that can compensate the negative TCF of the substrate to realize temperature stable devices [141, 142]. However, the film thicknesses required are relatively large. For this work we chose to study an anisotropic material such as ZnO and a high acoustic velocity material, nanocrystalline diamond (NCD). ZnO has been utilized as a thin film to generate SAWs for sensing [143] and electronic applications [144], as well as a waveguide for SAWs travelling on ST-Quartz [64] and  $36^\circ$  YX  $\text{LiTaO}_3$  [67]. We chose ZnO because theoretical and experimental results show that when employed as a waveguiding layer, power transfer and sensitivity is increased compared to the aforementioned  $\text{SiO}_2$  [63, 67]. This is believed to be caused by the piezoelectric nature of ZnO, since the difference in wave

velocities is minimal, 2747 m/s (ZnO) to 2850 m/s (SiO<sub>2</sub>). Furthermore, ZnO also has a negative TCF value which can compensate for ST-Quartz's positive TCF value [145, 146]. Due to its high acoustic velocity which allows the realization of devices operating at GHz frequencies [147], diamond has been an attractive material for SAW devices. It has also been shown that a layered SAW device that includes a diamond film will cause dispersion of the electromechanical coupling coefficient, and by designing the center frequency on the local maximum of the k<sup>2</sup> dispersion curve gives low IL [5]. Therefore, diamond was also chosen as a filling material because we hypothesized its inclusion would increase operating frequency and subsequently sensitivity. Also, it is biocompatible and chemically stable. Most importantly, these materials were chosen because practical devices can be realized since both can be deposited and characterized by established techniques [148-152].

#### 4.2.2. Theory

A system of four coupled wave equations for the electric potential and the three components of displacement in piezoelectric materials are solved for the piezoelectric substrate or the solid domain [103]:

$$-\rho \frac{\partial^2 u_i}{\partial t^2} + c_{ijkl}^E \frac{\partial^2 u_k}{\partial x_j \partial x_l} + e_{kij} \frac{\partial^2 \varphi}{\partial x_k \partial x_j} = 0, \quad (4.1)$$

$$e_{ikl} \frac{\partial^2 u_k}{\partial x_i \partial x_l} - \varepsilon_{ik}^S \frac{\partial^2 \varphi}{\partial x_i \partial x_k} = 0. \quad (4.2)$$

Here  $c_{ijkl}^E$ ,  $e_{ikl}$ , and  $\varepsilon_{ik}^S$  are the elastic constant tensor for a constant electric field, the piezoelectric constant tensor, and the permittivity tensor respectively for constant strain;  $\rho$  is the density;  $u_i$  are the mechanical displacements;  $\varphi$  is the electric potential;  $t$  is the time; and  $i, j, k$ , and  $l = 1, 2, 3$ .

These coupled wave equations can be discretized and solved for generating displacement profiles

and voltages at each element/node. The piezoelectric material displacements obtained from the above equations are applied to the solid model at each time step.

#### ***4.2.3. Finite Element Model***

A 3-D structural finite-element model of a SAW device is shown in Figure 4.1. The model represents a two-port delay line SAW device with substrate geometry of 1600 $\mu\text{m}$  length, 200  $\mu\text{m}$  width, and 500  $\mu\text{m}$  depth. The depth was chosen to represent the thickness of an actual SAW substrate, while the length was chosen to limit the amount of reflections from the substrate edges. The coupled field element Solid 226 is used in the simulation. To mesh the 3-D structure, tetrahedral elements having 4 degrees of freedom (DOF) are used. Three DOF define displacements in the x, y, and z directions. The fourth DOF is voltage. To reduce the number of nodes generated, a non-uniform mesh was used, with a larger meshing density near the surface and towards the center. Both the input and output IDTs are composed of three finger pairs having a periodicity of 40  $\mu\text{m}$  and aperture width of 147  $\mu\text{m}$ . To simplify the analysis, the IDT fingers were defined to be mass-less elements, represented by a set of nodes coupled through the voltage degree of freedom (DOF) allowing second order effect due to mass loading to be ignored. The distance between the IDTs ( $4\lambda$ ) sets the delay path length. For comparison to a standard SAW substrate a 4 x 4 array of microcavities having square cross-sectional area,  $\lambda/2$  x  $\lambda/2$ , and depths of 2.5 $\mu\text{m}$  and 5  $\mu\text{m}$  was implemented in the center of the delay path. Additionally, in the case of filled microcavities, material (ZnO or NCD) was added as plugs to fill the entire depth of the cavities.

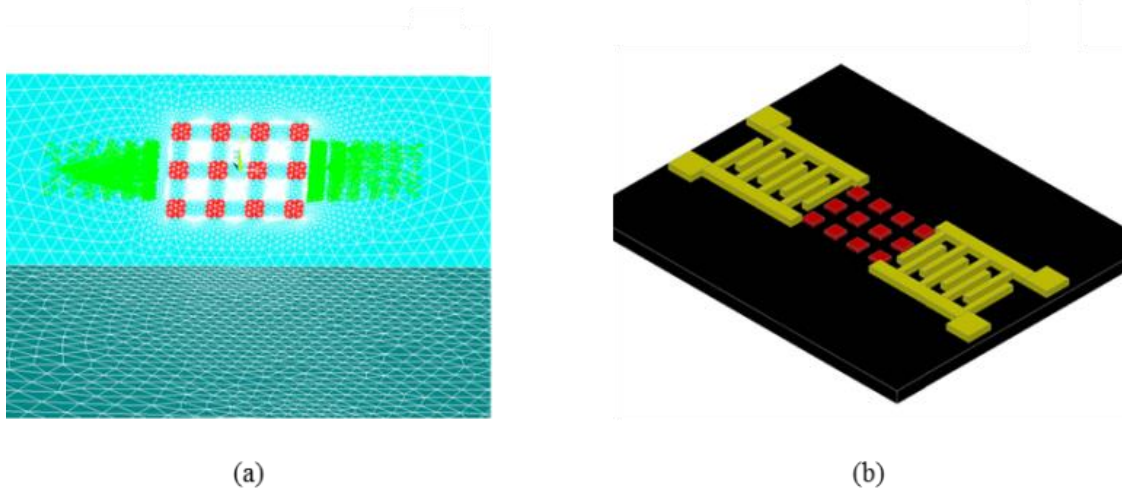


Figure 4.1 (a) Image of FE model of SAW device with filled microcavities used in ANSYS simulations and (b) illustration of SAW device with filled microcavities

#### 4.2.4. Simulation Analysis

The SAW frequency response was determined by taking the Fourier transform of the impulse response. To obtain the impulse response, an impulse voltage signal, having amplitude of 100 V, is applied to the transmitting IDT. The structure was simulated for 200 ns using a time step of 0.95 ns. Once the run is complete, the output voltage from the nodes on the output IDT is recorded vs. time. The voltage vs. time data is converted into the frequency response by applying an FFT algorithm using a custom Matlab code.

We also performed AC analysis to study the acoustic wave propagation and interaction with the various microcavity designs. Displacement and mass loading data was obtained by doing an AC analysis at the device center frequency acquired from the impulse response. For each device configuration an AC voltage with amplitude of 2.5 V at a frequency,  $f_0$ , was applied to the input IDT, using a time step of 0.95 ns and a duration of 200 ns.

#### ***4.2.5. Fabrication of SAW Devices with Microcavities***

A SH-SAW device with microcavities in the delay path was fabricated using standard photolithography techniques, metal evaporation and lift-off, and deep reactive ion etching (DRIE) on a 36° YX lithium tantalate (LiTaO<sub>3</sub>) wafer 0.5 mm thick and 76.2 mm diameter. Before applying photoresist, the wafer was solvent cleaned, rinsed with DI water and dried with N<sub>2</sub>. NR9 1500PY (Futurrex) negative tone photoresist was applied using a spin coater at 3000 rpm/s for 40 s to achieve a thickness of 1.4 μm. The photoresist was baked on a hotplate for 60 s at 150 °C. Next the wafer was exposed to broadband UV light for 4 s at 20 mW/cm<sup>2</sup>. After exposure the photoresist was hard baked on a hotplate for 60 s at 100 °C followed by immersion in RD6 (Futurrex) developer for 12 s, rinsing with DI water and drying with N<sub>2</sub>. A Ti/Au film 20/100 nm thick was evaporated over the entire wafer using e-beam evaporation. The IDTs were formed by placing the wafer in an acetone bath to lift-off excess metal. To remove any remaining metal between IDT fingers, ultrasonication in acetone for 1 min was used. A second lithography step was employed to create a photoresist etch mask. The wafer was solvent cleaned, rinsed with DI water, dried with N<sub>2</sub> and placed in O<sub>2</sub> plasma for 5 min. AZ 4620 (Clariant) was spin coated onto the wafer at 1600 rpm/s for 35 s and placed in a vacuum oven for 20 min. After rehydration of the photoresist it was exposed to broadband UV light for 18 s at 20 mW/cm<sup>2</sup>. To open up the holes for the microcavities the resist was developed in 1:4 AZ400K (Clariant) for 3-4 min. To ensure good etch selectivity the resist was hard baked for 4 h in a vacuum oven at 70°C. In order to avoid cracking of the wafer, internal stress within the substrate caused by heating during the etch process was alleviated by dicing the wafer into individual devices prior to etching. LiTaO<sub>3</sub> was etched by DRIE for 11.5 min (p = 6 mTorr, CH<sub>4</sub> = 13 sccm, He = 149.7

sccm,  $C_4F_8 = 17$  sccm,  $P = 2800$  W, bias  $P = 400$  W, substrate temp =  $-20$  °C). The photoresist mask was removed by soaking in acetone and cleaning with  $O_2$  plasma.

#### ***4.2.6. Device Measurement and Characterization***

The depth of the microcavities was determined with an alphastep profilometer. An Agilent 8753ES network analyzer was used to measure the frequency response of the SAW devices. To eliminate reflections and unwanted bulk modes, time gating was applied.

### **4.3. Results and Discussion**

#### ***4.3.1. Frequency Response and Material Displacements for 36° YX LiTaO<sub>3</sub>***

To validate our simulation model and to verify that we are simulating the proper acoustic wave mode for this particular substrate, we compared the simulated center frequency from the impulse response to the expected theoretical value for this substrate. For an IDT periodicity equal to  $40$   $\mu\text{m}$  and a SAW velocity of  $4212$  m/sec, the theoretical center frequency is  $105.3$  MHz. Figure 4.2 is the frequency response obtained from our simulation of bare  $36^\circ$  YX LiTaO<sub>3</sub> and it shows a center frequency of  $100.25$  MHz. The shifted center frequency is due to the small delay path length ( $4\lambda$ ) which causes multiple reflections between input and output IDTs and destructive interference of the fundamental wave mode. This can be alleviated by increasing the delay path length to  $10\lambda$ . The center frequency is  $105.53$  MHz which is close to the theoretical value for this substrate and orientation. However, IL is increased from  $-13.1344$  dB to  $-15.9536$  dB because of increased propagation losses and diffraction. The results of the simulation model accurately depict the physics and proper acoustic wave mode, but we will use the smaller delay path for the rest of the simulations to decrease node number and simulation time.

To capture the nature and type of displacements associated with the wave generated, we ran an AC analysis at the center frequency. Nodes on the output IDT were selected and the

average displacement data in the x, y and z directions was plotted vs. time. Figure 4.3 shows the surface normal (z), longitudinal (x) and shear-horizontal (y) displacements vs. time. Comparison of the various displacement amplitudes reveals that the polarization is most prominent in the y direction (SH polarization) and confirms that the wave is indeed shear-horizontal. This is indicative of a LSAW known to propagate in  $36^\circ$  YX LiTaO<sub>3</sub>. Based on the simulated center frequency and nature of particle displacements associated with the propagating wave, we are confident that the simulation is accurately portraying the correct wave mode for this particular substrate.

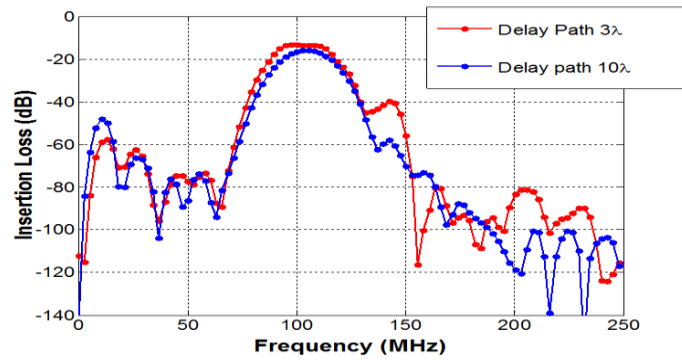


Figure 4.2 Simulated frequency response for a two-port SAW device based on bare  $36^\circ$  YX LiTaO<sub>3</sub>, where delay paths equal to  $3\lambda$  and  $10\lambda$  are compared.

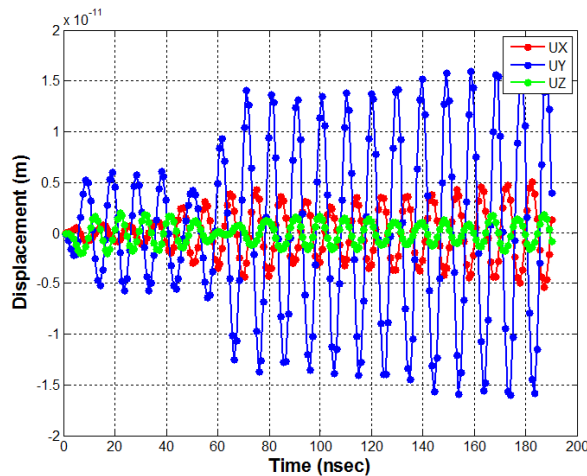


Figure 4.3 Displacements vs. time for  $36^\circ$  YX LiTaO<sub>3</sub>

### 4.3.2. Comparison of Insertion Loss

To compare the acoustic energy dissipation and power consumption in a SAW device, we systematically compare the insertion loss (IL) for all device configurations. Based on the frequency response of the various devices, the insertion loss was obtained at the respective center frequency of the various devices and was compared to determine the effect of various ZnO, diamond and air filled microcavities on the resulting power transfer. Figure 4.4 shows the frequency response for each design.

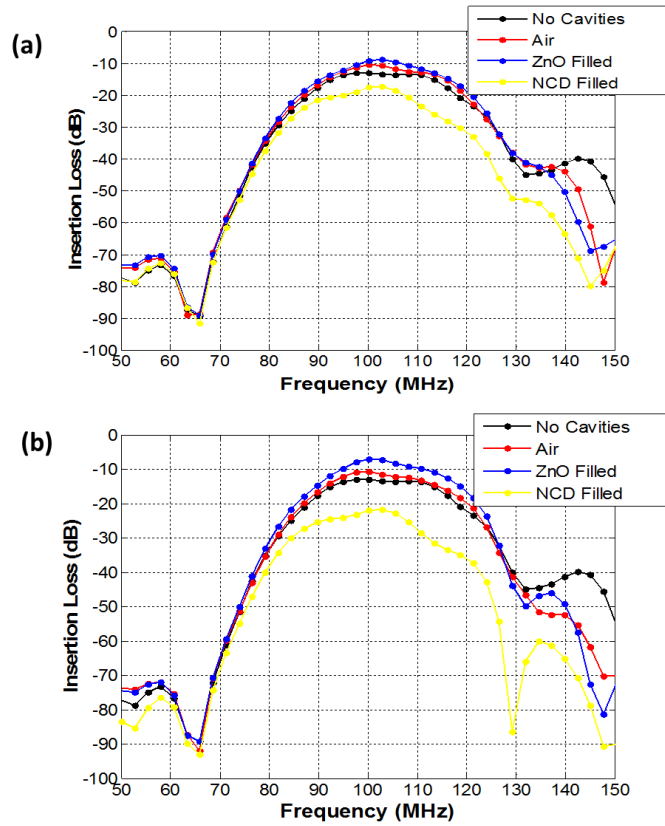


Figure 4.4 Comparison of the simulated frequency responses for the different device with microcavity depth equal to (a) 2.5  $\mu\text{m}$  and (b) 5  $\mu\text{m}$ .

In Fig 4.4 (a), the insertion loss for microcavities having a shallow depth of 2.5  $\mu\text{m}$  and filled with air, ZnO and NCD are compared to a standard delay line setup. A summary of the simulation results is given in Table 4.1. An increase in power transfer occurs for air filled and

ZnO filled microcavities. Of the two, the ZnO filled cavities performs best, decreasing the loss by 4.26 dB, which is more than a 50% enhancement in power transfer. On the contrary, for this depth, NCD filled cavities lead to a reduction in power transfer ( $\Delta IL = -4.22$  dB). The frequency responses for devices with microcavity depths of  $5\mu\text{m}$  are show in Fig 4.4 (b). As was the case for  $2.5\mu\text{m}$  deep cavities, ZnO and air filled microcavities increase power transfer, while the incorporation of NCD increases loss. It was mentioned in the introduction that the piezoelectric nature of ZnO enhances the wave guiding effect. Using our FE model, we set the piezoelectric constants to zero and re-ran the ZnO simulations. As expected, larger decreases in IL occurred for all depths when the piezoelectric nature of ZnO was included. A comparison of the results is shown in Table 4.1. Again the inclusion of ZnO as a filling material in the microcavities has the greatest effect on power transfer decreasing IL by 6.03 dB. This is 1.5 times the value for  $2.5\mu\text{m}$  cavity depth. Our simulations show that a sensor with  $5\mu\text{m}$  depth microcavities filled with ZnO is the most effective at increasing power transfer and this design should be used for systems that require low power consumption.

Table 4.1 Results from frequency response simulations for the various device configurations

Filling Material	Microcavity depth = $2.5\mu\text{m}$				Microcavity depth = $5\mu\text{m}$			
	IL (dB)	$\Delta IL$ (dB)	$f_0$ (MHz)	$\Delta f_0$ (MHz)	IL (dB)	$\Delta IL$ (dB)	$f_0$ (MHz)	$\Delta f_0$ (MHz)
No Cavities	-13.1344	N/A	100.2506	N/A	-13.1344	N/A	100.2506	N/A
Air	-10.5193	2.6151	100.2506	0	-10.8194	2.315	100.2506	0
ZnO	-8.8732	4.2612	102.8888	2.8888	-7.1021	6.0323	100.2506	0
ZnO ( $d_{ij} = 0$ )	-8.9072	4.2272	102.8888	2.8888	-7.2163	5.9181	100.2506	0
Diamond	-17.3557	-4.2213	102.8888	2.8888	-21.7930	-8.6586	102.8888	2.8888

### 4.3.3. Mass Sensitivity Analysis

To measure each device's response to a surface perturbation, a force equivalent to  $100\text{pg}/\text{cm}^2$  was uniformly applied to an area of  $6600\ \mu\text{m}^2$ . Similar to the approach taken by Atashbar *et al.*, in which an FEM was used to study an  $\text{H}_2$  SAW gas sensor [34], the impulse response of each device to the applied load was simulated and the IL data before and after the perturbation was compared. The change in the propagation characteristics (i.e. amplitude and velocity) to the above-applied load is evaluated. Several types of perturbations of interest to SAW sensor research are application of a rigid mass layer, a purely viscous fluid and a viscoelastic film. In biosensing applications, the perturbation can be a combination of these three, depending on the biological material used [153]. For a rigid mass layer with a thickness less than the acoustic wavelength, the layer moves synchronously with acoustic oscillations in the substrate without dissipation of wave energy [116]. Thus, for this scenario of pure mass loading, there will only be a change in the acoustic velocity without a corresponding change in its amplitude. For viscoelastic films, which are similar to the case of an analyte attaching to a biorecognition layer, amplitude and velocity changes occur and must be monitored to accurately determine the sensor's response. For this reason, the change in resonant frequency and amplitude of the acoustic wave to mass loading for each sensor design was studied. Additionally, we recognize that biosensing applications require sensing of an analyte contained in a liquid sample. One reason for choosing the simplified mass-perturbation over an actual liquid loading is due to the computational intensity required. Secondly, our goal was to obtain trends in mass-sensitivity to mass loading and make qualitative comparisons between the various device configurations. Since the type of wave that propagates is a leaky SAW with a primary SH component (see Figure 4.3), the wave does not couple strongly with the liquid loading the

surface. Hence, the trends between the different devices even in a liquid environment are likely to be the same since the propagating wave mode is unchanged with the addition of the microcavities.

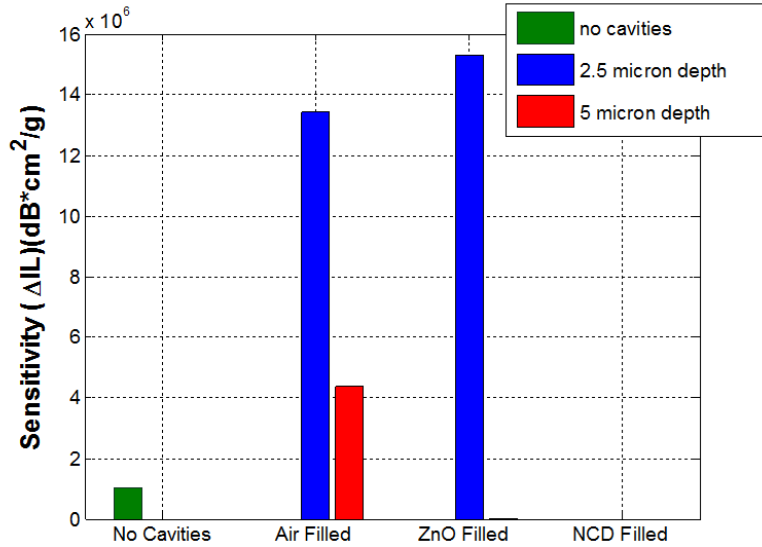


Figure 4.5 Comparison of mass sensitivity with respect to change in IL ( $\Delta IL$ ) for all the device configurations studied, where microcavity depths are 2.5  $\mu m$  and 5  $\mu m$  deep. Note that the NCD filled cavities are insensitive to the surface perturbation.

Figures 4.5 and 4.6 show the sensitivity to a  $100 \text{ pg}/\text{cm}^2$  load applied uniformly to a  $6600 \mu\text{m}^2$  area between the transmitting and receiving IDTs. Analysis of Figures 4.5 and 4.6 shows that microcavities having a depth of  $2.5 \mu\text{m}$ , filled with air and ZnO, are highly sensitive to an applied 100 pg mass for both changes in the acoustic wave's amplitude and resonant frequency. In particular, when ZnO is used as the filling material, mass sensitivity to changes in the resonant frequency is 3 times greater than that for a standard delay line, and mass sensitivity to changes in IL is 15.2 times greater. For the amount of mass applied to the delay path, diamond filled cavities are insensitive to surface loading, which is shown by the zero change in the resonant frequency and wave amplitude. Thus, we can conclude that for the device

configurations studied at this depth, ZnO filled cavities are optimal for detecting mass perturbations occurring at the surface. This can be attributed to the greater confinement of acoustic energy at the surface due to waveguiding effects and the larger surface particle displacements occurring from constructive interference of the forward and reflected waves in the delay path.

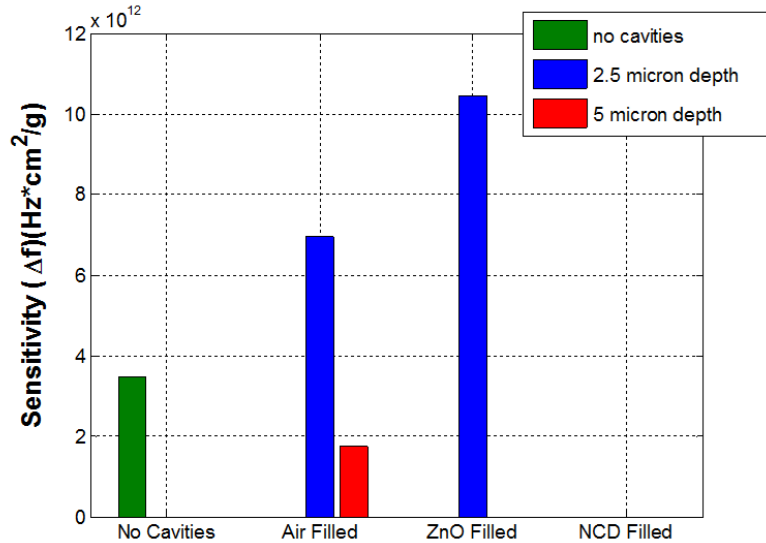


Figure 4.6 Comparison of mass sensitivity with respect to change in resonant frequency ( $\Delta f_0$ ) for all the device configurations studied, where microcavity depths are 2.5  $\mu\text{m}$  and 5  $\mu\text{m}$  deep

The red bars in Figures 4.5 and 4.6 show the mass sensitivity for microcavities that are 5  $\mu\text{m}$  deep. We find at this depth air filled cavities clearly outperform the other designs. Unlike the case for 2.5  $\mu\text{m}$  deep cavities, when filled with ZnO the sensitivity to mass loading is less than that of air filled cavities. This is due to density effects, whereby filling the cavities with the higher density ZnO pushes that wave into the substrate as it travels. This conversion from surface to bulk mode leaves less acoustic energy available at the surface to interact with the mass being applied. However, for the two depths studied (2.5  $\mu\text{m}$  and 5  $\mu\text{m}$ ), cavities filled with ZnO had the highest sensitivity to mass loading for changes in both resonant frequency and wave

amplitude. In addition, we see the same result for the 5  $\mu\text{m}$  deep cavities filled with NCD as we did for 2.5  $\mu\text{m}$  deep cavities filled with NCD; the device is non-responsive to the 100 pg mass loaded onto the surface. To gain a clearer understanding of the mass sensitivity results, a visual representation of acoustic wave propagation for the various devices is presented in the next section.

#### ***4.3.4. Comparison of Displacement Contours and Profiles***

We analyzed the acoustic wave propagation characteristics in terms of the temporal evolution of the displacement contours and profiles. Contour plots and surface displacement profiles for the various device configurations shown in Figures 4.7, 4.8 and 4.9 elucidate how the presence of cavities with and without filling material affect acoustic wave propagation. Figure 4.7 shows that the displacement contours for all the devices studied at a time step = 110 ns. This corresponds to the time it takes for a wave to travel between input and output IDTs and transmission of the triple transit signal. Values represented in the contour plots shown in Figure 4.7 and 4.8 are the square root of the sum of the squares of x, y and z displacements, which correspond to the longitudinal, shear-horizontal and surface normal directions, respectively. Red on the color bar indicates where material displacements are the largest and blue is where they are the smallest. To better view how the wave is affected by the presence of the microcavities, a sectional view is provided in Figure 4.7 in which the substrate is sliced down the middle along its length.

When microcavities are introduced into the delay path (Figure 4.7 (b)-(d) and Figure 4.8 (b)-(d)) it has two significant effects on wave propagation, the extent of which depend on the depth of the cavities and the nature of the filling material: 1) acoustic radiation into the bulk is minimized in the direction of the output transducer and 2) displacements in the center of the

delay path where the microcavities are present are enhanced due to constructive interference between forward and scattered/reflected waves.

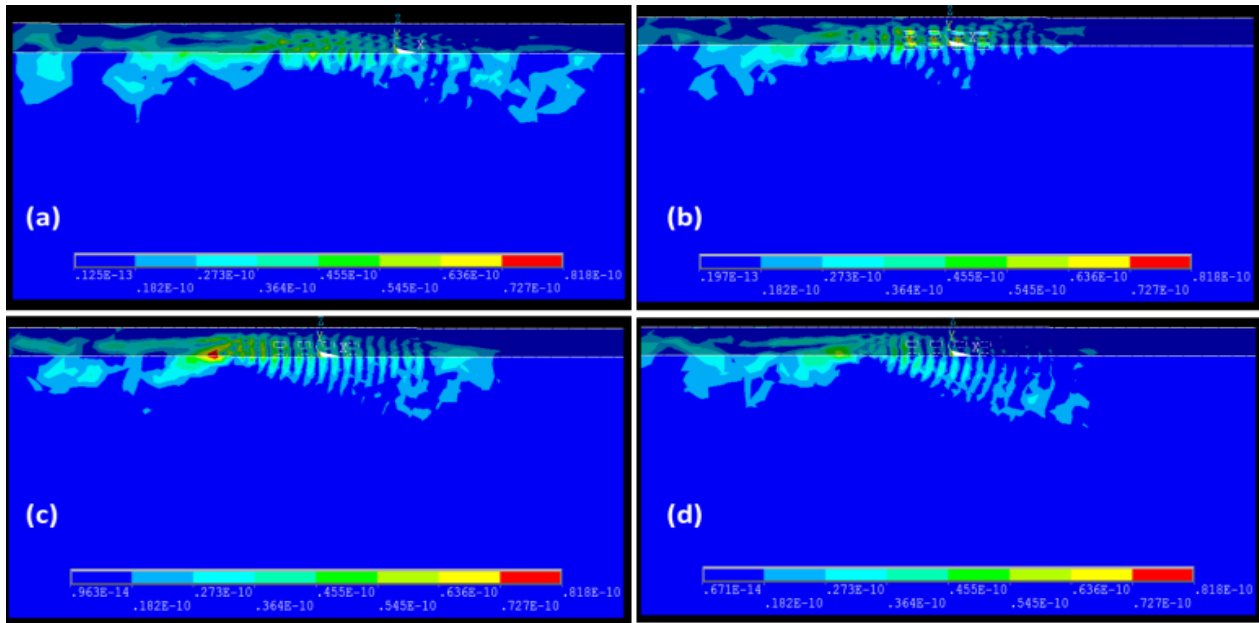


Figure 4.7 Nodal contour plots of sum of  $x$ ,  $y$  and  $z$  displacements at a time step of 110 ns for (a) device with no microcavities in the delay path, (b) air filled cavities, (c) ZnO filled cavities and (d) NCD filled cavities; the microcavity depths are  $2.5 \mu\text{m}$

It is clear in Figure 4.7 (b) and (c) that if the material inserted into the cavity has a lower velocity than the substrate, waveguiding occurs and the energy is trapped at the surface.

However, in the case of diamond filled cavities (Figure 4.7 (d)), where the acoustic velocity is much greater than that of the substrate, the wave is refracted into the bulk of the crystal as soon as it reaches the microcavity array. Because there is a lack of acoustic energy available at the surface, the device is insensitive to mass loading.

In Figure 4.8 a top view of each device focused at the center of the delay path is provided. The same time step (110ns) used in Figure 4.7 was used to generate these contour plots.

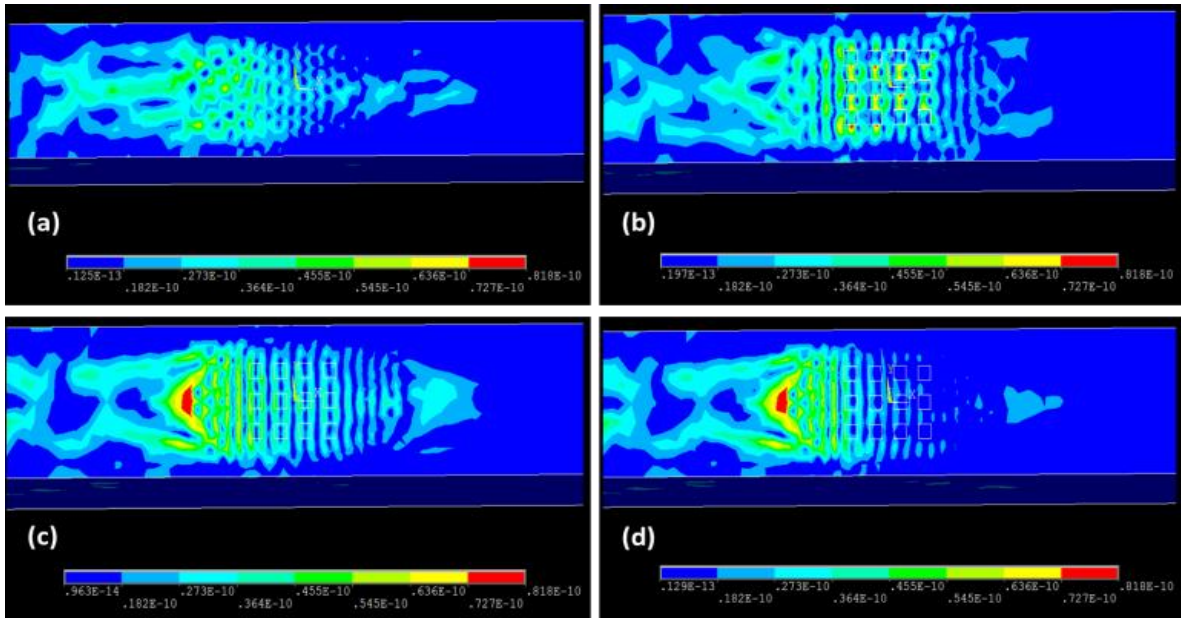


Figure 4.8 (Top view) Nodal contour plots of sum of x, y, and z displacements at a time step of 110 ns for (a) bare SAW device, (b) air filled cavities, (c) ZnO filled cavities and (d) NCD filled cavities; the microcavity depths are 2.5  $\mu\text{m}$

In Figure 4.8 ((b) and (c)) it clear that air and ZnO filled cavities enhance displacements within the center of the delay path. The observed enhancements in the mass sensitivities arise from higher confinement of acoustic energy near the surface when compared to the no-cavity case. A closer inspection of Figure 4.8 ((b) and (c)) shows that the air filled cavities caused some dispersion of the wave and distortion of the wave front while filling the cavities with ZnO causes limited dispersion. Also, the wave front is focused and better defined. This focusing effect provided by the ZnO filled cavities produces larger sensitivity values at this depth (2.5 microns). In Figure 4.8 (d) we see that there are minimal displacements in the cavity region. This view corroborates what we saw in Figure 4.7 (d); when the acoustic wave encounters the NCD filled cavity array it is refracted into the bulk of the substrate.

The particle displacement profiles for each of the device configurations are compared in Figure 4.9. Displacement data in the longitudinal (x), SH (y) and surface-normal (z) directions

vs. time was obtained by selecting a set of nodes on the output IDT after excitation of the input transducer with an AC signal at the center frequency found from each device's respective IL plot.

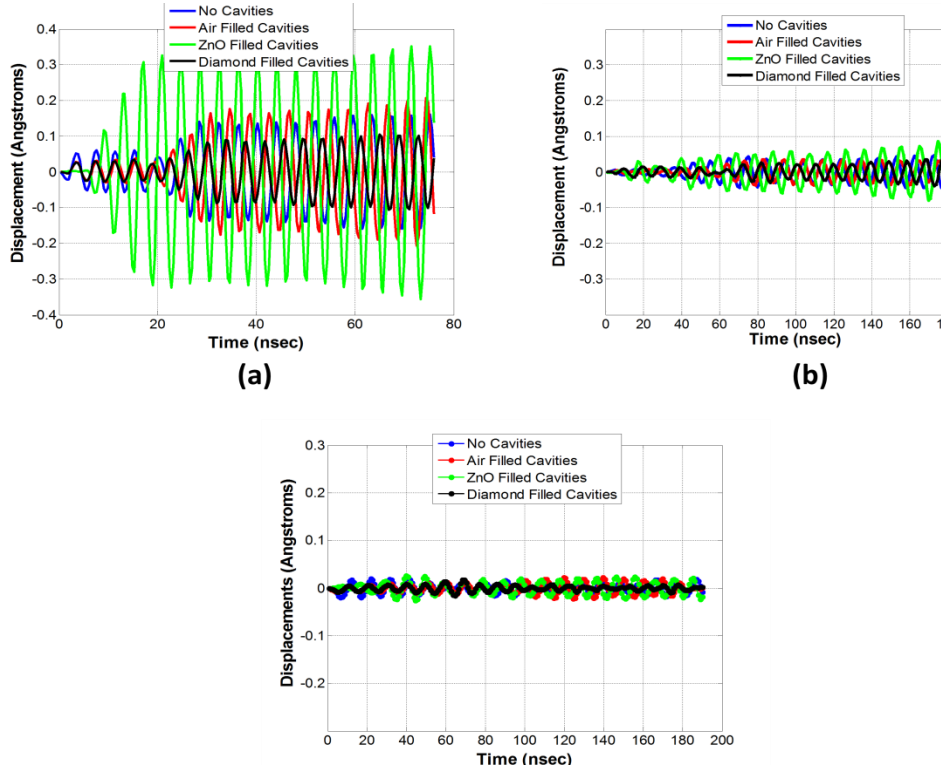


Figure 4.9 Nodal displacements at the output IDT vs. time for all the different device configurations in the (a) SH (y) direction, (b) longitudinal (x) direction and (c) substrate normal (z) direction; the microcavity depth is  $2.5 \mu\text{m}$

When microcavities are absent, displacement is most prominent in the SH direction (y-direction), and less prominent in the direction of propagation (x-direction) and normal to the surface (z-direction) as shown in Figure 4.9 (a)-(c). Results in Figure 4.9 further show that the SH displacement for  $2.5 \mu\text{m}$  cavities is increased for ZnO and Air filled cavities with the largest displacements occurring when ZnO is present. Because of the piezoelectric effect, current induced in the output transducer is proportional to material displacement underneath where it's deposited. The decreased IL values compared to the substrate with no microcavities for these

device configurations are due to these larger particle displacements. In contrast, SH displacement is decreased when NCD is plugged into the microcavities, possibly due to the high stiffness of the filling material. This reduction in displacements at the output IDT is responsible for the decreased IL for this design. Consistent with the results for the no-cavities case, SH displacement is still more prominent than displacements in the x and z directions for all devices with microcavities. Thus, we conclude that although the wave mode propagating is still a LSAW, its amplitude is a strong function of the filling material. A similar analysis was carried out for 5  $\mu\text{m}$  microcavity depths with similar trends seen for displacements at the output IDT.

#### 4.3.5. SAW Devices with Microcavities

Images of the SAW delay path after etching microcavities are shown in Figure 4.10. The total etch time was 11.5 minutes which resulted in an etch rate of  $834.78 \text{ \AA}/\text{min}$ . This etch rate is relatively low compared to materials such as quartz or silicon because etching is mainly a physical process for  $\text{LiTaO}_3$ . Thus the ability to etch large depths is negatively affected if a masking material with greater selectivity is not used. The final depth of the microcavities was  $\sim 1 \mu\text{m}$  which was determined using an alphastep profilometer.

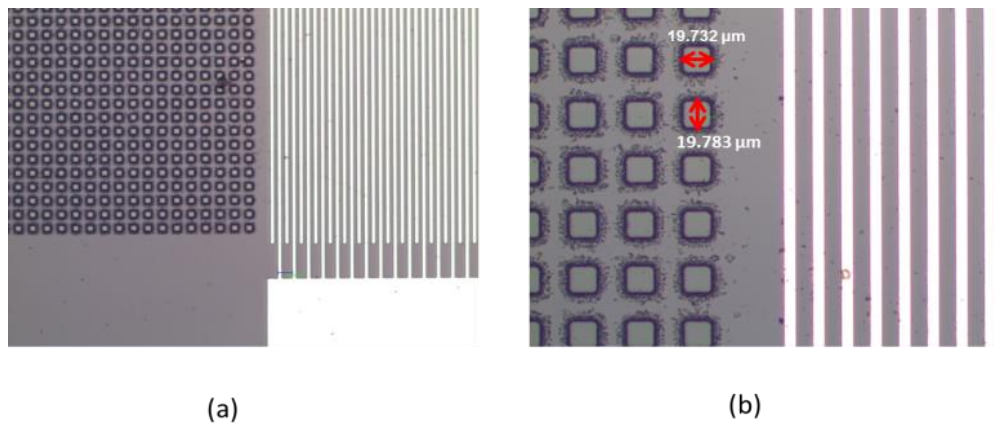


Figure 4.10 Image taken from a microscope of the SAW delay path showing etched microcavities next to an IDT at (a) 5X magnification and (b) 20X magnification

The frequency responses for a SAW device with and without unfilled microcavities in the SAW delay path are compared in Figure 4.11 to determine how the addition of microcavities effect power transfer. Analysis of the plot shows that microcavities increase power transfer by 3.306 dB. Since experimental results were successful, we ran additional simulations for air, ZnO, and NCD filled cavities having 1 $\mu$ m depth. The frequency response data is shown in Table II. For each device configuration, the IL is decreased compared to a standard device, with air filled cavities having the largest  $\Delta$ IL. The comparison of  $\Delta$ IL for measured and simulated devices (air cavities) show that power transfer is greater in the simulations [ $\Delta$ IL = 6.5043 (simulation),  $\Delta$ IL = 3.306 dB (experiment)]. Possible explanations are the manufacturing tolerances, mass of IDTs, visible surface roughness and the need for an appropriate scaling factor. It is expected that the acoustic velocity should be slightly lower due to cavities present in the delay path. The acoustic velocities can be derived using the measured center frequencies. Indeed, the cavities decrease the acoustic velocity from 4212 m/sec to 4164 m/sec. The acoustic velocity for the simulated device is 4116 m/sec which is in close agreement with the measured value. The combined simulation/experimental results for 1  $\mu$ m deep cavities indicate that further work is needed to optimize the cavity depth for each design configuration. Further studies are underway to determine the optimal depths for each case along with experimental verification of sensitivity. Future work will also include ways to remedy issues that occur during fabrication.

Table 4.2 Simulation results comparing IL for air, ZnO, and NCD filled cavities to a standard device where the cavity depth is 1 $\mu$ m

<b>Filling Material</b>	<b>IL (dB)</b>	<b><math>\Delta</math>IL (dB)</b>
<b>No Cavities</b>	-13.1344	N/A
<b>Air</b>	-6.6301	6.5043
<b>ZnO</b>	-7.7270	5.4074
<b>NCD</b>	-12.1497	0.9847

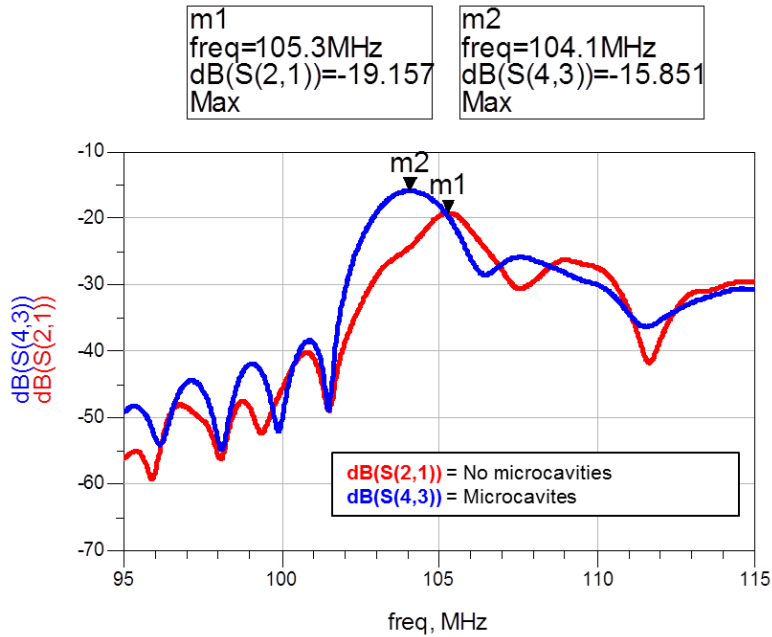


Figure 4.11 Measured frequency responses for a device with air filled microcavities in the delay path (blue curve) and a device with no microcavities in the delay path (red curve).

#### 4.4. Conclusions

In summary, we have performed a systematic study of SAW sensors with delay path modification in the form of various filled microcavities. An FEM model was used to compare power consumption and mass sensitivity for SAW sensors based on  $36^\circ$  YX LiTaO<sub>3</sub>. Several different designs were studied which includes a standard SAW delay line, devices with microcavities in the delay path filled with ZnO or NCD, and a device with microcavities with no filling material. We also showed experimentally that microcavities can be etched in LiTaO<sub>3</sub> and they increase power transfer compared to a standard SAW sensor.

To compare power consumption for each design, IL values were obtained from a Fourier transform of the impulse response. For both 2.5  $\mu$ m and 5  $\mu$ m cavity depths, ZnO and Air filled

cavities increase power transfer compared to a standard delay line design. In contrast, NCD filled cavities decreases IL for both depths studied. Results of our initial simulations show that 5  $\mu\text{m}$  deep microcavities filled with ZnO was most effective at increasing power transfer ( $\Delta \text{IL} = 6.04 \text{ dB}$ ). Thus, for applications where power consumption is a concern, this design would be preferred over a standard delay line sensor.

To evaluate mass sensitivity a force equal to  $100 \text{ pg/cm}^2$  was applied to the area between the two transducers. For a microcavity depth of  $2.5 \mu\text{m}$ , air and ZnO filled cavities showed a high sensitivity to mass loading, with ZnO filled cavities being the most sensitive. This is a result of waveguiding effects and larger surface particle displacements occurring from constructive interference of the forward and reflected waves in the delay path. However, for  $5 \mu\text{m}$  deep cavities we observe that the density of the filling material plays a key role in influencing the mass sensitivity; low-density material such as air results in higher sensitivities compared to ZnO. Of all the designs studied for sensitivity to mass loading, a device with  $2.5 \mu\text{m}$  depth filled with ZnO is the best.

The combined insertion loss and sensitivity results show that ZnO is better suited to improve sensor characteristics compared to NCD. However, there are other materials worth studying based on their usefulness in other SAW sensor designs. For example, other waveguide materials like  $\text{SiO}_2$  or PMMA, and several metals typically used in grating structures are all worth investigating as filling materials.

To better understand physically what is happening to acoustic wave propagation from insertion of microcavities, an AC analysis was performed to obtain contour plots and displacement profiles. We see from the contour plots that air and ZnO filled microcavities effectively limit transmission of acoustic energy into the bulk of the substrate and cause larger

displacements in the region where the microcavities are placed because of constructive interference. It is the combination of increased particle displacements and energy entrapment at the surface that is responsible for the enhanced sensitivity of these designs. This effect is also evident for air filled cavities 5  $\mu\text{m}$  deep, but is reduced for ZnO filled cavities at this depth. We conclude that the higher density of the ZnO filling material pushes the wave into the substrate bulk as it propagates limiting the amount of energy available at the surface. The same analysis of contour plots for devices containing cavities filled with NCD show that as soon as the acoustic wave comes in contact with NCD microcavity array it is refracted into the bulk because of the larger acoustic velocity of NCD compared to  $36^\circ$  YX LiTaO<sub>3</sub>. Lastly, an increase in particle displacements at the output IDT for devices with air and ZnO filled microcavities, determined by x, y and z displacement data, is responsible for the decrease in power consumption when compared to a bare SAW sensor.

We fabricated devices containing 1  $\mu\text{m}$  deep microcavities in the delay path and ran additional simulations with an equivalent cavity depth to compare. Fabricated SAW sensors with  $\sim 1\mu\text{m}$  deep cavities left unfilled, reduced IL by 3.306 dB. In comparison to simulated air filled cavities the reduction was not as high [ $\Delta\text{IL} = 6.5043$  (simulation)]. Several factors can account for this such as IDT mass, manufacturing tolerances and the need for an appropriate scaling factor. For air and NCD filled cavities, the simulation results for 1  $\mu\text{m}$  depth cavities indicates a trend—decreasing cavity depth increases power transfer. However, this trend doesn't carry over to ZnO. Thus, an additional study is needed to determine the optimal cavity depth for each filling material. Furthermore, we are currently optimizing the fabrication process to etch all the cavity depths presented in the simulations and will fill them with ZnO and diamond. We conclude from this study that the incorporation of microcavities in the delay path of a SAW

sensor is beneficial to decreasing power loss and increasing mass sensitivity. Since air and ZnO-filled microcavities with relatively shallow depths are found to be beneficial and we showed that cavities can be etched in 36° YX LiTaO<sub>3</sub> fairly easily, our simulations offer encouraging prospects for designing ultra-low power and highly sensitive biosensors that can reliably and easily detect numerous interactions at the surface.

## **CHAPTER 5: SHEAR-HORIZONTAL SURFACE ACOUSTIC WAVE PHONONIC DEVICE WITH HIGH DENSITY FILLING MATERIALS FOR ULTRA-LOW POWER SENSING APPLICATIONS<sup>2</sup>**

Finite element simulations of a phononic shear-horizontal surface acoustic wave (SH-SAW) sensor based on ST 90°-X Quartz reveal a dramatic reduction in power consumption. The phononic sensor is realized by artificially structuring the delay path to form an acoustic meta-material comprised of a periodic microcavity array incorporating high-density materials such as tantalum or tungsten. Constructive interference of the scattered and secondary reflected waves at every microcavity interface leads to acoustic energy confinement in the high-density regions translating into reduced power loss. Tantalum filled cavities show the best performance while tungsten inclusions create a phononic bandgap. Based on our simulation results, surface acoustic wave (SAW) devices with tantalum filled microcavities were fabricated and shown to significantly decrease insertion loss (IL). Our findings offer encouraging prospects for designing low power, highly sensitive portable biosensors.

### **5.1. Introduction**

Surface acoustic wave (SAW) biosensors based on a shear horizontal wave have been developed to detect breast cancer markers [22], E. Coli bacteria [68], and in DNA hybridization studies [72]. A current trend in these biosensing systems is to move away from clinical

---

<sup>2</sup>Reprinted with permission from M. Richardson, S. K. R. S. Sankaranarayanan, and V. R. Bhethanabotla, "Shear-horizontal surface acoustic wave phononic device with high density filling material for ultra-low power sensing applications," *Applied Physics Letters*, 104, 253501, 2014. Copyright 2014, AIP Publishing LLC. Permission is included in Appendix A.

laboratories where expensive bulky equipment and highly skilled personnel are needed and move to point-of-care-testing (POCT). Monitoring a physiological signal such as blood glucose level in a patient with a wireless sensor provides a good example [137]. A major challenge to the incorporation of wireless sensors for biosensing/medical applications is power consumption. In most of the active sensors, the power source is on-board (i.e. battery operated) and it is critical for these devices to operate in the low power limit for longer life. An alternative to battery-operated devices is a passive wireless sensor. A switch to passive wireless sensors over active devices (battery operated) has several other advantages: fewer complications, smaller size, little to no maintenance and lower cost [154]. In either active or passive sensors, new paradigms in low power and multifunctional electronics are sought.

Realizing SAW based portable devices remains problematic due to their high losses  $\sim 10$ -30 dB. Traditional approaches undertaken to combat this problem include the incorporation of reflective gratings [10], grooves and corrugated surfaces [11], the application of waveguide materials [12, 108] and optimization of transducer designs that support unidirectional wave propagation [138]. Our approach to reduce power consumption is to utilize a new class of artificially structured materials (termed phononic crystals), which allow controlled manipulation of fundamental acoustic wave properties. In a phononic crystal, a periodic variation in the density and/or elastic constant of the structure is typically utilized to control wave scattering and interference to form either acoustic band-gaps or propagation bands. Phononic devices based on high density filling materials such as tungsten have been recently utilized to realize wide band-gap devices [155, 156].

A potential breakthrough in device power consumption can be realized by controlling the dispersion relation for phonons both inside and outside the band gap. For example, we recently

demonstrated that periodic air inclusions (microcavities) contained within the delay path of a SAW sensor simultaneously increased sensitivity and decreased power consumption.[9, 140] Motivated by these findings and exploiting the concept of phononic crystals, we introduce a SH-SAW phononic device by filling the cavities in the delay path with high density materials. Depending on properties of the filling material, we can minimize propagation losses and realize ultra-low power SAW biosensors or create a complete band-gap.

## 5.2. FEM of Tungsten and Tantalum Filled Microcavities

Finite element (FE) models have been successfully used to study SAW sensors and their characteristics [108, 114]. Thus, a 3-D structural FE model of a SAW device based on ST 90°-X Quartz containing filled microcavities (cross-sectional area =  $\lambda/2 \times \lambda/2$ , depth 2.5  $\mu\text{m}$  or 5  $\mu\text{m}$ ) in the delay path was used to determine the frequency response and visualize acoustic wave propagation. Each cavity was filled with a high-density material (tantalum or tungsten). The computational details are provided in the supplementary information [157]. The figure of merit that determines the degree of power consumption is insertion loss (IL). In Figure 5.1 (a) and (b), the simulated frequency response for the substrate without microcavities is compared to devices having microcavities filled with either tungsten or tantalum. Figure 5.1 (a) and (b) show that for both depths, microcavities filled with tantalum significantly reduce IL [ $\Delta\text{IL} = 17.3693 \text{ dB}$  (2.5 $\mu\text{m}$  depth) and 18.113 dB (5 $\mu\text{m}$  depth)]. Further inspection of Figure 5.1 (a) also indicates a narrowed passband, increased power to higher frequency modes, and a downward shift of the fundamental frequency due to decreased acoustic wave velocity. When the depth is increased to 5  $\mu\text{m}$  the frequency response for tantalum filled cavities becomes more complex (Figure 5.1 (b)). Ripples in the passband and reduced out-of-band suppression occur because of interference of bulk waves and SH-SAWs at the receiving IDT. Microcavities filled with tungsten have the

opposite effect on power transfer than those filled with tantalum. IL is increased for the range of frequencies that make up the original SAW passband. The largest IL occurs at the center frequency of the sensor without microcavities. This is evident by a notch in the frequency response for tungsten filled cavities for both depths.

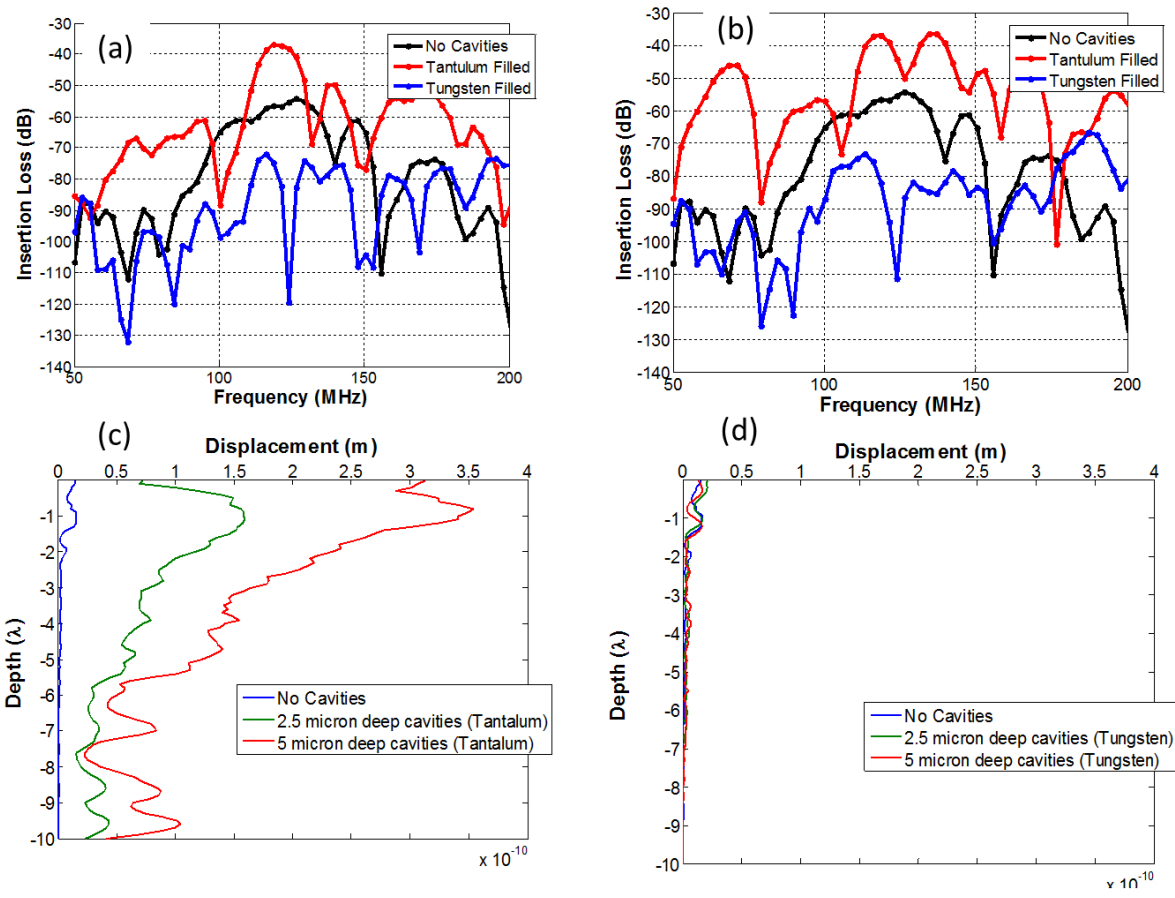


Figure 5.1 Simulated results for IL vs. frequency is plotted and compared for a device without microcavities and devices having microcavities filled with tungsten or tantalum where the cavity depth is (a) 2.5  $\mu\text{m}$  and (b) 5  $\mu\text{m}$ . Sum of the displacements vs. depth is plotted for (c) tantalum filled cavities and (d) tungsten filled cavities.

We analyzed nodal displacements vs. depth at the output IDTs [Figure 5.1 (c) and (d)] to determine the role of microcavities in influencing power transfer. Tantalum inclusions in the SAW delay path increased displacements at the substrate surface by 2 orders of magnitude over a bare sensor [Figure 5.1 (c)]. Displacements are further enlarged when the cavity depth is

increased from 2.5  $\mu\text{m}$  to 5  $\mu\text{m}$ . The larger displacements at the output IDT from the addition of the tantalum filled cavities are the reason IL is decreased. We conclude that the presence of cavities filled with tantalum in the SAW delay path is analogous to applying a waveguide to confine acoustic energy to the substrate surface and prevent its dissipation within the bulk of the material [9, 140]. A good example of a waveguide is the application of a ZnO Layer on ST-Quartz [145]. The addition of ZnO confined acoustic energy within the layer, which resulted in larger particle displacements and increased mass sensitivity. In order for a material to act as a waveguide, the acoustic velocity of the overlayer must be less than the acoustic velocity of the substrate. The average acoustic velocity,  $V_{avg}$ , of the area that contains Ta filled microcavities can be estimated by[158]:

$$V_{avg} = \left(\frac{w}{\Lambda}\right)^2 V_i + \left(1 - \left(\frac{w}{\Lambda}\right)^2\right) V_M, \quad (5.1)$$

where  $V_i$  is the velocity of the inclusion (Ta),  $V_M$  the velocity of the substrate,  $w$  is the length of microcavity and  $\Lambda$  is the microcavity periodicity. Because  $V_{avg}$  of the composite material (4630 m/sec) is less than the substrate (5060 m/sec), acoustic energy is confined to the surface in the microcavity region. Similarly, we analyzed displacement data for tungsten filled cavities [Figure 5.1 (d)]. At the substrate surface, displacements are decreased by a factor of two with respect to the standard SAW sensor. The smaller displacements at the output IDT explains the larger insertion loss when tungsten inclusions are added. Additionally, nodal surface displacements were obtained at the center of the delay path for each device configuration. The results were similar to those obtained at the output IDT. Tantalum filled cavities enhanced surface displacements by 2 orders of magnitude compared to devices with tungsten filled cavities and no

cavities. Since sensor sensitivity is proportional to surface displacements [116], then incorporating tantalum filled cavities in the SAW delay path will increase its sensitivity. To better understand acoustic wave propagation and interaction with the microcavities, we plotted the displacement contours at a time step of 110 ns (Figures 5.2, 5.3). First, we evaluated substrate displacements along a plane normal to the surface (Figure 5.2). Tantalum filled cavities confine wave energy close to the surface and in the center of the delay path [Figure 5.2 (a), (b)]. As the depth is increased to 5  $\mu\text{m}$  [Figure 5.2 (b)], mass loading effects begin to compete. The displacements are still primarily confined to the substrate's center region but the displacements below the surface are greater, indicating that bulk mode conversion is also higher. A stark contrast exists when the filling material is tungsten instead of tantalum [Figure 5.2 (c) and (d)]. An incoming wave at the tungsten cavity interface is reflected at an angle away from the surface into the bulk material. Thus, displacements within the cavity region and at the receiving IDT are minimized. Next, we utilized a top view to closer inspect FEM displacement contours around the microcavity region (Figure 5.3). We start with an analysis of the plots for tantalum filled cavities. The composition of alternating layers of two different materials, suggests that at every cavity interface, an incoming wave transfers part of its energy into secondary, reflected and scattered waves, which then interfere with each other. In the case of shallow tantalum filled cavities, there is constructive interference of the secondary waves, which minimizes bulk dissipation and results in significant acoustic confinement to the surface [Figure 5.2 (a) and Figure 5.3 (a)]. The same effect can be seen for the larger depth (5  $\mu\text{m}$ ), but as we previously mentioned, mass loading effects start to dominate. Plots for tungsten filled cavities show almost total reflection of acoustic energy at the cavity interface with a small amount of

energy that leaks through the spacing between cavities. This result corroborates the behavior shown in Figure 5.1.

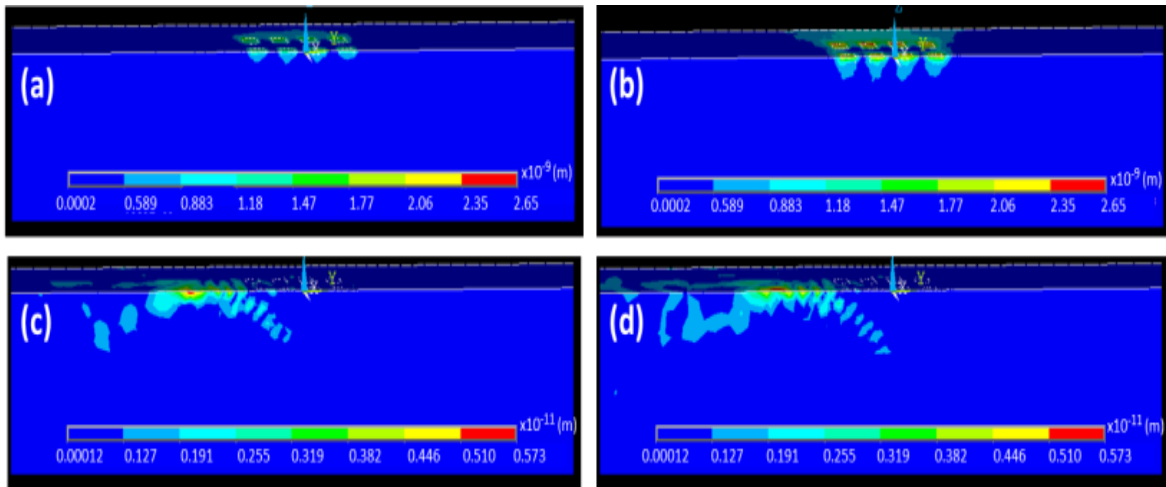


Figure 5.2 Sectional view of substrate showing displacements at a time step = 110 ns for (a) 2.5  $\mu\text{m}$  deep cavities filled with tantalum, (b) 5  $\mu\text{m}$  deep cavities filled with tantalum, (c) 2.5  $\mu\text{m}$  filled cavities filled with tungsten and (d) 5  $\mu\text{m}$  cavities filled with tungsten. Note that displacements are analyzed at  $t=110$  ns which is enough for the wave to travel from the input to output IDTs, along with the triple transit signal and ensures that there are no significant interference from reflected waves coming from the substrate edges.

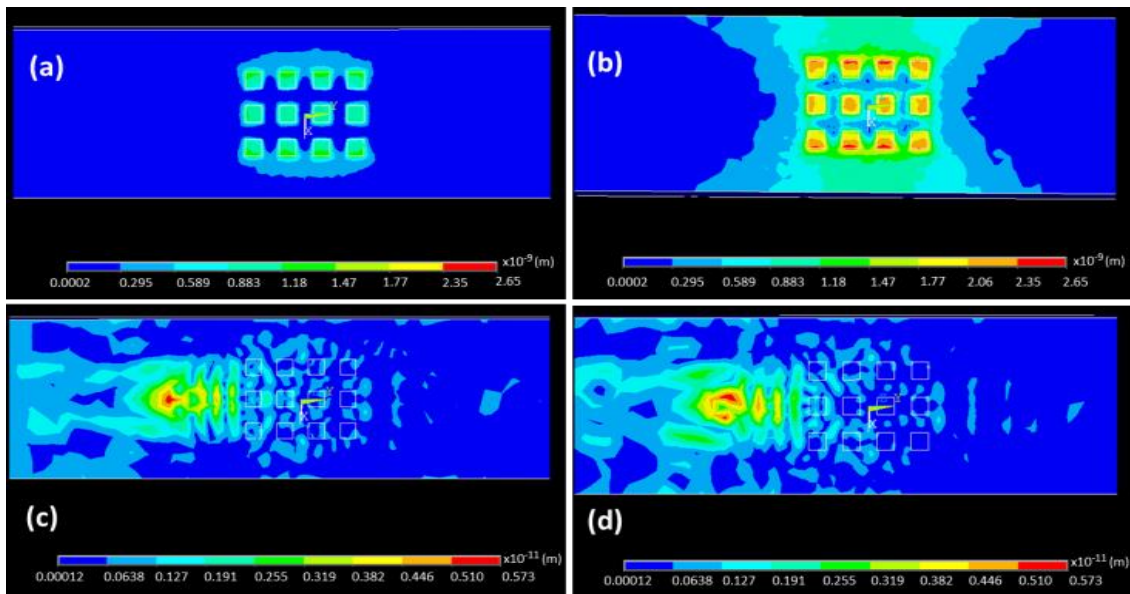


Figure 5.3 Top view of substrate showing displacements at a time step = 110 ns for (a) 2.5  $\mu\text{m}$  deep cavities filled with tantalum, (b) 5  $\mu\text{m}$  deep cavities filled with tantalum, (c) 2.5  $\mu\text{m}$  deep cavities filled with tungsten and (d) 5  $\mu\text{m}$  deep cavities filled with tungsten.

From a materials perspective, it is interesting to note that although tungsten has a higher density than tantalum, the performance of the latter is better. To better understand the observed differences in the wave interactions between the tungsten and tantalum filled cavities, we determine the acoustic impedance mismatch between the matrix (substrate) and the inclusions (filling material). The acoustic impedance,  $Z$ , for a particular material is

$$Z = \rho V \quad (5.2)$$

where  $\rho$  and  $V$  are the density and velocity. Based on equation (5.2), high acoustic impedance can be obtained using a high-density material or a material with a large acoustic velocity. To promote the wave-guiding effect, which requires an overlay material to have a lower acoustic velocity than the substrate; materials with high acoustic velocities are not desirable and are therefore not considered.

Note that the substrate material used in this study is ST-Quartz which has very high acoustic impedance compared to air. If microcavities are inserted into the delay path and left unfilled, a large impedance mismatch occurs; this would result in the reflection of the acoustic wave as it approaches the array of inclusions. By filling the cavities with materials with high acoustic impedance, we observe that wave reflections and destructive interference of the scattered and reflected wave are minimized. Inserting the values of acoustic impedance for the matrix and inclusions into equation 5.3, gives us the amount of acoustic power reflected at the interface between the two.

$$\Gamma^2 = \left( \frac{Z_i - Z_m}{Z_i + Z_m} \right)^2 \quad (5.3)$$

Here  $Z_i$  and  $Z_m$  are the acoustic impedance of the inclusions and host material respectively. As  $\Gamma^2$  approaches 1, there will be less energy traveling from the input to output transducer. Relevant material properties, acoustic impedance and reflection coefficients are presented in Table 5.1.

Table 5.1 Relevant material properties for the substrate and filling materials under study

Filling Material	Density	Young's Modulus	Velocity	Acoustic Impedance	$\Gamma^2$	Velocity Mismatch ( $V_m/V_i$ )
None (ST 90°-X Quartz)	2684 kg/m <sup>3</sup>	Anisotropic	5060 m/sec	13.58 MΩ	N/A	1
Tantalum	16,650 kg/m <sup>3</sup>	186 GPa	3342.33 m/sec	55.42 MΩ	0.368	1.51
Tungsten	19,300 kg/m <sup>3</sup>	411 GPa	4614.69 m/sec	87.86 MΩ	0.536	1.096

The observed differences in the acoustic wave interaction with the microcavity array, pictured in Figures 5.3 and 5.4, can be explained on the basis of reflection coefficient values for each substrate/filling material combination along with the ratio of the substrate velocity to the filling material velocity ( $V_m/V_i$ ), both given in Table 5.1. When the microcavities are filled with tantalum the reflection coefficient,  $\Gamma^2$ , is 0.368. As a result, minimal acoustic energy is reflected at the interface and since the velocity of the filling material is less than the substrate velocity, we see that the acoustic energy is confined to the cavities. In comparison,  $\Gamma^2$  is 0.536 when tungsten is the filling material. Thus, the wave is partially reflected/scattered as it interacts with the microcavity array. In addition, the velocity of the filling material is close to substrate's velocity. Therefore, there is no entrapment of acoustic energy within the cavities as with tantalum.

### 5.3. Fabrication and Measurement of Tungsten and Tantalum Filled Microcavities

To confirm our theoretical predictions, SAW devices with tantalum and tungsten filled microcavities (Figure 5.4) were fabricated using standard photolithography techniques, e-beam

deposition, metal lift-off and deep reactive ion etching (DRIE). Detailed information on the fabrication process can be found in the supplementary information [157]. Since enhanced power transfer is theoretically predicted for shallow cavities, only 0.5  $\mu\text{m}$  deep cavities were etched and filled with tantalum. In addition, devices with tungsten filled cavities were also fabricated for comparison. The frequency response of the SAW was measured using an Agilent 8753 ES network analyzer. To eliminate spurious responses due to reflected waves and bulk wave generation, time gating was applied. Frequency response measurements show that the tantalum filled microcavities reduce IL by 7.615 dB [Figure 5.4 (d)], while tungsten filled cavities increase IL by 4.343 dB. Further analysis of Figure 5.4 (d) shows that the center frequency is increased when cavities are present compared to the no cavity case. For tungsten this can easily be explained by referring to Figure 5.2 (c) and (d). The acoustic wave is deflected into the bulk of the substrate as it encounters the microcavity array. Because bulk waves have higher velocities than surface waves, the center frequency is increased. Also, the effective stiffness of the propagating path is increased for tantalum and tungsten filled cavities. This could've caused an increase in the SAW velocity and thus the center frequency [48]. The discrepancy in IL values between devices with tantalum and tungsten filled cavities indicate acoustic damping due to mass loading is nullified. If an equivalent metal film was deposited onto the delay path, the SAW amplitude would be attenuated, but measured and simulated results for tantalum filled microcavities contradicts this assumption. Although the assumption appears to apply for tungsten filled cavities, the depiction of the acoustic wave being reflected from the microcavity region [Figure 5.2 (c) and (d)] indicates otherwise. In conclusion, the trend observed in simulations is evident in our experimental results. While theoretical results were predicated on microcavity depths equal to 2.5  $\mu\text{m}$  and 5  $\mu\text{m}$ , optimization of the fabrication process is currently underway

to obtain these metrics. In addition, the cross-section of the microcavities is slightly larger than  $\lambda/2 \times \lambda/2$  utilized in our simulations. Future modification of the etching process should yield tighter tolerances.

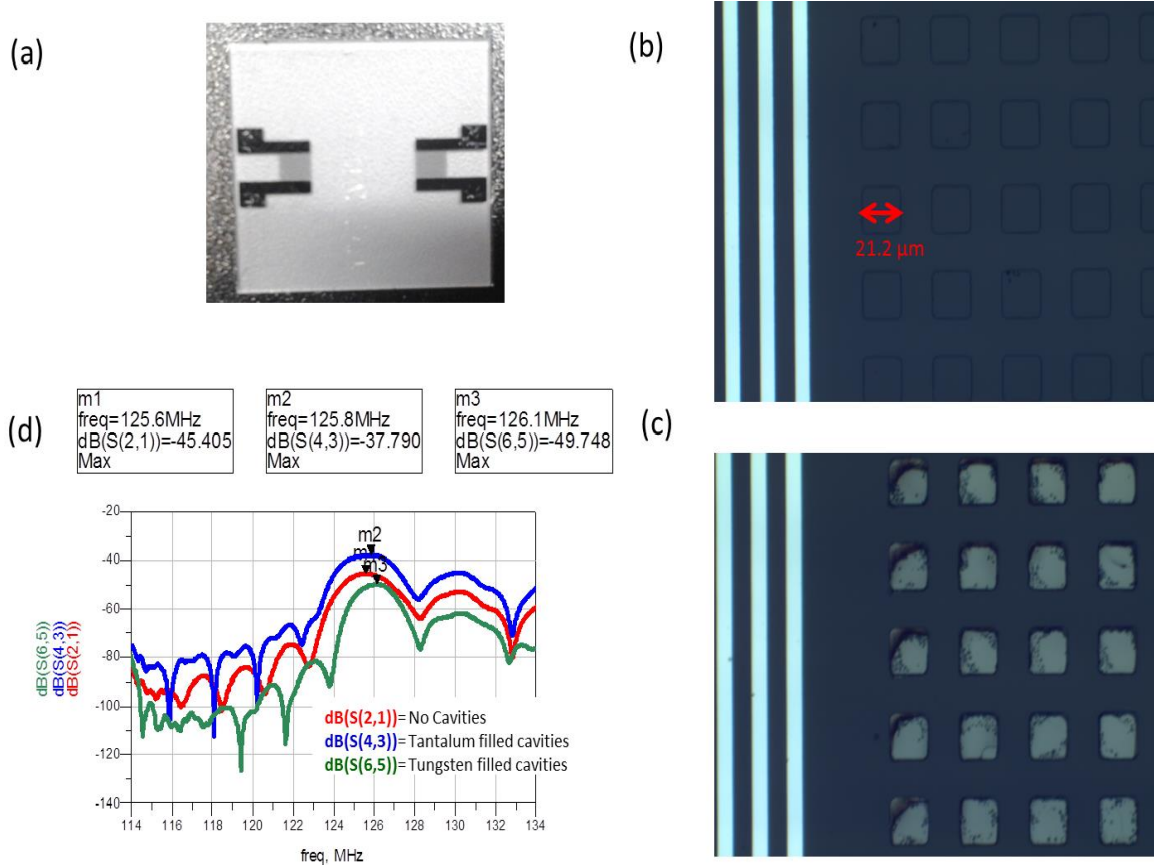


Figure 5.4 (a) SAW chip is shown prior to etching microcavities and filling with Ta. (b) Image from microscope taken near the input IDT after etching microcavities into the quartz substrate. (c) Image from microscope taken near the input IDT after the microcavities in (b) was filled with tantalum. (d) Experimental comparison of frequency response for a SAW device with no microcavities in the delay path to SAW devices with  $\sim 0.5 \mu\text{m}$  deep microcavities in the delay path filled with tantalum or tungsten.

## 5.4. Conclusion

In summary, our simulations and experiments show that the concept of a phononic crystal can be exploited to realize a low-power SH-SAW sensor. The SH-SAW phononic sensor contained an array of microcavities filled with high density materials such as tungsten and

tantalum. The filled microcavities decrease power consumption significantly compared to standard SAW. Power transfer is optimal when the cavity depth is 2.5  $\mu\text{m}$  and filling material is tantalum. Simulations show higher acoustic wave energy entrapment at the surface for tantalum filled cavities due to its small  $\Gamma^2$  and lower acoustic impedance mismatch compared to tungsten. The combination of these findings will allow the production of a highly sensitive wireless sensor that can be used in various biosensing applications.

## **CHAPTER 6: REMOVAL OF NON-SPECIFICALLY BOUND PROTEINS USING RAYLEIGH WAVES ON AN ST-QUARTZ SUBSTRATE**

Label-free biosensors are plagued by the issue of non-specific protein binding which negatively affects sensing parameters such as sensitivity, selectivity, and limit-of-detection. In the current work, a coupled-field finite element (FE) fluid structure interaction (FSI) model of a surface acoustic wave (SAW) device based on an ST-Quartz substrate in contact with a liquid loading was used to predict trends in forces related to SAW-induced acoustic streaming. Based on model predictions, it is found that the computed SAW body force is sufficient to overcome adhesive forces between particles and a surface while lift and drag forces prevent reattachment for a range of SAW frequencies. We further performed experiments to validate the model predictions and observe that the excitation of Rayleigh SAWs removed non-specifically bound (NSB) antigens and antibodies from sensing and non-sensing regions, while rinsing and blocking agents were ineffective. An amplified RF signal applied to the device input disrupted the specific interactions between antigens and their capture antibody as well. ST-quartz allows propagation of Rayleigh and leaky SH-SAW waves in orthogonal directions. Thus, the results reported here could allow integration of three important biosensor functions on a single chip, i.e., removal of non-specific binding, mixing and sensing in the liquid phase.

## 6.1. Introduction

Non-specific binding (NSB) can occur when macromolecules attach to a sensor surface via weak interactive forces (i.e. Van der Waals, hydrophobic and ionic) when it is in contact with a complex biological fluid (i.e. blood, urine or serum). This is problematic for label-free sensing techniques because non-specific interactions cannot be distinguished from specific interactions. Current methods to reduce non-specific binding involve creating inert/resistant surfaces through modifications. Some examples are chemical attachment or physisorption of self-assembled monolayers (SAMs) with appropriate head groups and/or chain length [159, 160], zwitterionic materials [161, 162], blocking proteins (BSA) [163, 164], or polymer films [i.e. poly(vinyl alcohol) (PVA), poly(vinylpyrrolidone) (PVP) and poly(ethylene glycol) (PEG)] [165-168]. Typical problems with these methods are increased setup time and costs due to additional steps and reagents, and incompatibility with common sensing materials.

The physical removal of (NSB) proteins has been accomplished by using acoustic energy [98, 99, 169] and the physical processes involved have been elucidated using finite element simulations [105, 106, 169, 170]. A study by Meyer et al [98] showed that the shear waves generated by a quartz crystal microbalance (QCM) can remove weakly attached proteins by lowering the activation energy of desorption through the generation of mechanical stress at the interface. However, the relatively high power levels used (3.5 W) can generate heat that could result in loss of protein activity. In another study by Cular et al. [99, 169] it was determined that NSB proteins could be removed via surface acoustic wave (SAW) induced acoustic streaming. Despite the success shown with this technique, the piezoelectric substrate used ( $128^\circ\text{YX LiNbO}_3$ ) only supports Rayleigh waves, which have shown to be ineffective in liquid sensing

applications. Therefore, another transduction mechanism would need to be employed for sensing, which would result in increased complexity.

In this work, the removal of NSB proteins is demonstrated theoretically and experimentally using Rayleigh SAWs generated on an ST-quartz substrate. A coupled-field finite element (FE) fluid structure interaction (FSI) model of a SAW device in contact with a liquid loading was used to predict trends in forces related to SAW induced acoustic streaming. Model predictions were utilized to compute the various interaction forces involved to determine if they are sufficient to remove non-specifically bound (NSB) proteins for a range of SAW frequencies. Experimentally, a micropattern of immobilized antibodies was applied to the delay path to segregate sensing and non-sensing areas. In successive steps, the removal of NSB antigens and an interfering protein from both areas, using SAWs, was studied. Lastly, an amplified RF signal was used to excite SAWs to examine if higher input power could disrupt antigen-antibody binding. Based on our results, a multifunctional “lab on a chip” device, with sensing and removal capabilities can be realized because quartz supports both shear-horizontal SAW (SH-SAW) used in biosensing, and Rayleigh SAW modes useful for NSB removal, on the same substrate.

## 6.2. Mechanism of NSB Protein Removal

The removal of non-specifically bound proteins depends on the relative magnitudes of the adhesive and the removal forces involved. The principal forces that non-specifically bind proteins immersed in a liquid to the SAW device surface are van der Waals and electrical double layer. For simplicity, proteins can be modeled as spherical particles with radius  $R$ . The van der Waals attraction force for a spherical particle near a flat surface is given by

$$F_{vdW} \approx \frac{AR}{6z^2}, \quad (6.1)$$

where  $A$  is the Hamaker constant for the non-retarded force and  $z$  is the distance where the force of adhesion is maximal. Typical values of  $A$  in a liquid environment are  $\sim 10^{-20}$  J. As  $z$  increases the van der Waals force becomes less significant. Typical values of  $z$  are in the range of 0.2-0.4 nm. Electrical double layer forces are typically associated with particles whose effective diameters are smaller than  $5 \mu\text{m}$  [171]. In aqueous solutions, a surface contact potential is created between two different materials based on each material's respective local energy state. To preserve charge neutrality, surface charges build up causing a double layer charge region. This results in electrostatic attraction between the materials. Since the magnitudes of these forces are similar, especially for sub-micron particles [172], it is usually sufficient to consider only the van der Waals force [173].

The forces responsible for removal of particles are the direct SAW force and the lift and drag forces that result from the mean velocity field in the fluid. The magnitude of the direct force is given by [169].

$$F_{SAW} \approx \sqrt{F_x^2 + F_z^2} R^2, \quad (6.2)$$

Here  $R$  is the particle radius and the equations for the force components  $F_x$  and  $F_z$  can be found in [169]. The fluid circulation around a particle results in inviscid lift forces, whose surface normal components act to remove the attached protein. The lift forces are given by

$$F_L \approx \rho(u_x R)^2, \quad (6.3)$$

where  $u_x$  and  $R$  refer to the surface normal component of velocity and the particle radius, respectively. These forces can be estimated based on the Bernoulli's equation by utilizing the pressure difference that exists between the bottom and top of the particle. The acoustic-streaming motion generated by SAWs leads to a drag force, caused by the interaction between the fluid

mean flow and the particles. The drag force results from the boundary layer-generated acoustic-streaming and is given by:

$$F_{ST} \approx \mu R u_z \quad (6.4)$$

Here,  $u_z$  and  $\mu$  refer to the tangential component of velocity and the fluid viscosity, respectively.

Based on our previous coupled field FE FSI simulations [169, 170] and the forces described above, the mechanism for ultrasonic removal of NSB proteins is elucidated (Figure 6.1). The SAW direct force ( $F_{SAW}$ ) simultaneously detaches NSB proteins from the SAW surface and moves them away from the region strongly influenced by adhesive forces (van der Waals). However, the SAW direct force decays rapidly with distance into the fluid—in the direction of wave propagation. To ensure removal occurs continuously and at distances where the direct force has diminished, a steady force is required. The hydrodynamic forces play a crucial role in this respect; the horizontal streaming-induced drag force ( $F_{ST}$ ) helps to push the NSB proteins away from the fouled area whereas the vertical streaming force or the lift force ( $F_L$ ) helps to prevent the re-adhesion of the proteins to the surface. As mentioned earlier, the van der Waals adhesion forces decrease rapidly with distance from the SAW surface. Thus, once the SAW force overcomes the adhesive forces and removes particles away from the surface, some distance  $z$  into the fluid, less force is required to prevent particle reattachment. At this point lift ( $F_L$ ) and drag forces ( $F_{ST}$ ) are sufficient to keep the removal process ongoing. To remove NSB proteins for a particular system requires optimization of design parameters such as input power (or voltage) and SAW frequency.

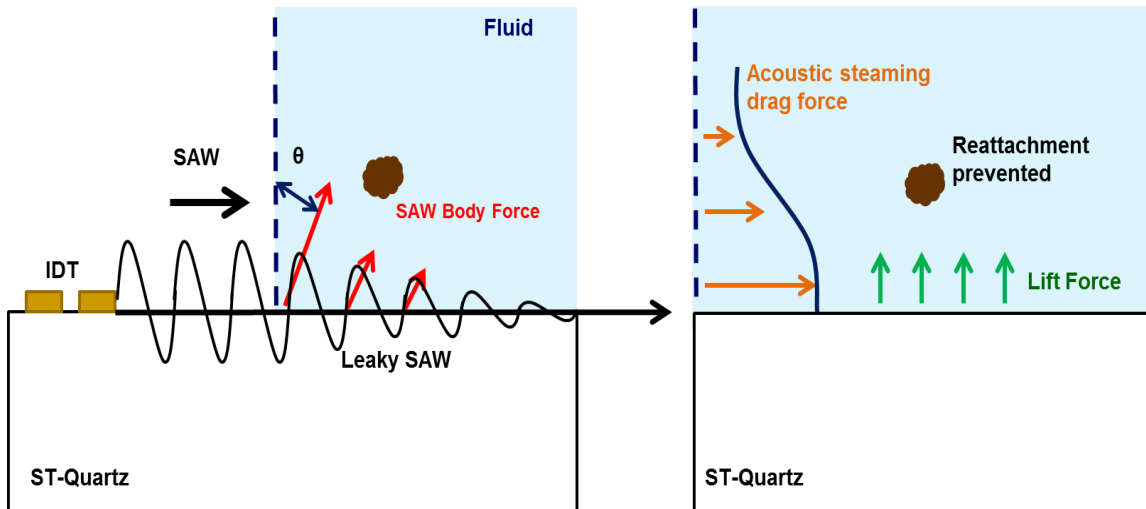


Figure 6.1 Coupled field FE FSI predicted mechanism of ultrasonic removal of particles weakly bound to a surface (i.e. NSB proteins). Simulations suggest that the interaction of the Rayleigh wave with the fluid medium results in a wave mode conversion into leaky SAW. This leaky SAW propagates along the boundary between the piezoelectric and the fluid loading and excites longitudinal waves into the fluid at a Rayleigh angle  $\theta$ . SAW direct forces result in initial particle detachment whereas hydrodynamic forces (i.e drag ( $F_{ST}$ ) and lift ( $F_L$ ) forces) prevent their reattachment.

### 6.3. Computational Details

A coupled-field FE FSI model previously developed by Sankaranarayanan *et al.* [169] with modifications was used to study acoustic steaming induced forces caused by SAW-fluid interaction. FE modeling of the fluid and solid domains require a complex mathematical model function of the node shaped factors and the equations of motion for each domain. Obtaining a solution to the FSI model involves sequentially solving the piezoelectric and fluid domains and transferring loads between each domain until convergence is achieved. The fluid fields are then computed to determine the various forces that act on particles in the system (i.e. non-specific proteins). The magnitude of these computed forces are compared to the adhesive forces on particles to discern if they are sufficient in strength to cause removal of NSB proteins.

### 6.3.1. Model Setup

The model consisted of a SAW device based on an ST-quartz substrate 400  $\mu\text{m}$  wide x 800  $\mu\text{m}$  long x 200  $\mu\text{m}$  deep in contact with a 50  $\mu\text{m}$  thick fluid. The input and output interdigital transducers (IDTs) each contained two finger pairs and were coupled by the voltage degree of freedom. The excitation of the piezoelectric solid was provided by applying an AC voltage at two different center frequencies (50 and 100 MHz) on the transmitter IDT fingers. The structure was simulated for a total of 100 nanoseconds (ns) with a time step of 1 ns.

### 6.3.2. Piezoelectric Domain

A system of four coupled wave equations for the electric potential and the three displacement components for a piezoelectric material are solved for the piezoelectric substrate or the solid domain [174]:

$$-\rho \frac{\partial^2 u_i}{\partial t^2} + c_{ijkl}^E \frac{\partial^2 u_k}{\partial x_j \partial x_l} + e_{kij} \frac{\partial^2 \phi}{\partial x_k \partial x_j} = 0, \quad (6.5)$$

$$e_{ikl} \frac{\partial^2 u_k}{\partial x_i \partial x_l} - \varepsilon_{ik}^s \frac{\partial^2 \phi}{\partial x_i \partial x_k} = 0. \quad (6.6)$$

Here  $c_{ijkl}^E$ ,  $e_{ikl}$ , and  $\varepsilon_{ik}^s$  are the elastic constant tensor for a constant electric field, the piezoelectric constant tensor, and the permittivity tensor, respectively for constant strain;  $\rho$  is the density;  $u_i$  are the mechanical displacements;  $\phi$  is the electric potential;  $t$  is the time; and  $i, j, k$ , and  $l = 1, 2, 3$ . These coupled wave equations can be discretized and solved for generating displacement profiles and voltages at each element/node. The piezoelectric material

displacements obtained from the above equations are applied to the solid model at each time step.

### 6.3.3. Fluid Domain

The Fluid domain was modeled using the Navier-Stokes equation; the arbitrary-Lagrangian-Eulerian approach was employed to handle the mesh distortions arising from the motion of the solid substrate.

$$\rho \left( \frac{\partial \mathbf{v}_f}{\partial t} \right) + \mathbf{v}_f \cdot \nabla \mathbf{v}_f + \nabla P - 2\eta \nabla \cdot \mathbf{D} = 0, \quad (6.7)$$

$$\nabla \cdot \mathbf{v}_f = 0, \quad (6.8)$$

here,  $\mathbf{v}_f$ ,  $P$ ,  $\rho$  and  $\eta$  denote the fluid velocity, pressure, density, and viscosity, respectively.  $\mathbf{D}$  is the rate of deformation tensor given by:

$$\mathbf{D} = \frac{1}{2} (\nabla \mathbf{v}_f + (\nabla \mathbf{v}_f)^t). \quad (6.9)$$

### 6.3.4. Coupling from Solid Domain to Fluid Domain

The fluid-solid coupling was established by maintaining stress and displacement continuity at the fluid-structure interface. The input velocity to the fluid domain is the velocity transferred from the piezoelectric domain at the interface. The boundary of fluid towards the atmosphere was kept as open with the following boundary condition:

$$\mathbf{u}_{open} = \vec{n}_x \mathbf{u}_x + \vec{n}_y \mathbf{u}_y, \quad (6.10)$$

where  $\mathbf{n}$  is the normal vector to the boundary.

### 6.3.5. Coupling from Fluid Domain to Solid Domain

The structural deformations were solved using an elastic formulation and a nonlinear geometry formulation to allow large, time varying deformations. The piezoelectric device is fixed to the bottom of the fluid channel and boundaries common between fluid and solid experience a load from the fluid, given by:

$$F_T = -\vec{n}(-p\vec{I} + \eta(\nabla u + \nabla u^T)), \quad (6.11)$$

where  $\vec{n}$  is the normal vector to the boundary. This load term represents a summation of pressure and viscous forces acting on the substrate due to velocity.

## 6.4. Computational Results and Discussion

To determine if Rayleigh SAWs generated on ST-Quartz are able to remove NSB proteins a coupled field FE FSI model was used to predict the various SAW induced acoustic streaming forces. The main mechanisms responsible for overcoming adhesive forces (van der Waals and electrical double layer) are the direct SAW force ( $F_{SAW}$ ), lift ( $F_L$ ) and drag forces ( $F_{ST}$ ) that result from the mean velocity field in the fluid [170]. An AC voltage (1V) of varying frequency (1, 10, 50 and 100 MHz) was applied to the transmitting IDT, and the streaming velocities were obtained along the fluid film thickness at distances  $0.5\lambda$  and  $2.5\lambda$  ( $\lambda$  = SAW wavelength) along the delay path (Figure 6.2).

Our simulated results show that the streaming velocity increases with the SAW frequency (Figure 6.2). The simulated streaming velocities are in the  $\mu\text{m/s}$  range for the frequencies studied, which are consistent with experimental values found in literature for streaming flows induced by SAW devices [175-177]. As the frequency of the surface-acoustic-wave device increases, it would lead to an increase in the irrotational velocity. This in turn results in an increase in the acoustic-streaming velocity, which is proportional to the square of the irrotational

velocity. Note, however, that the acoustic-streaming velocity is also proportional to the square of the amplitude of SAW displacement. The simulated SAW amplitudes tend to increase with decreasing device frequency. This has also been observed in the experimental studies of Sano *et al.* [178] and Shiokawa *et al.* [179]. Therefore, the increase in SAW amplitude somewhat offsets the corresponding decrease in the device frequency. As a result, the simulated SAW streaming velocities shown in Figure 6.2 exhibit a near linear variation.

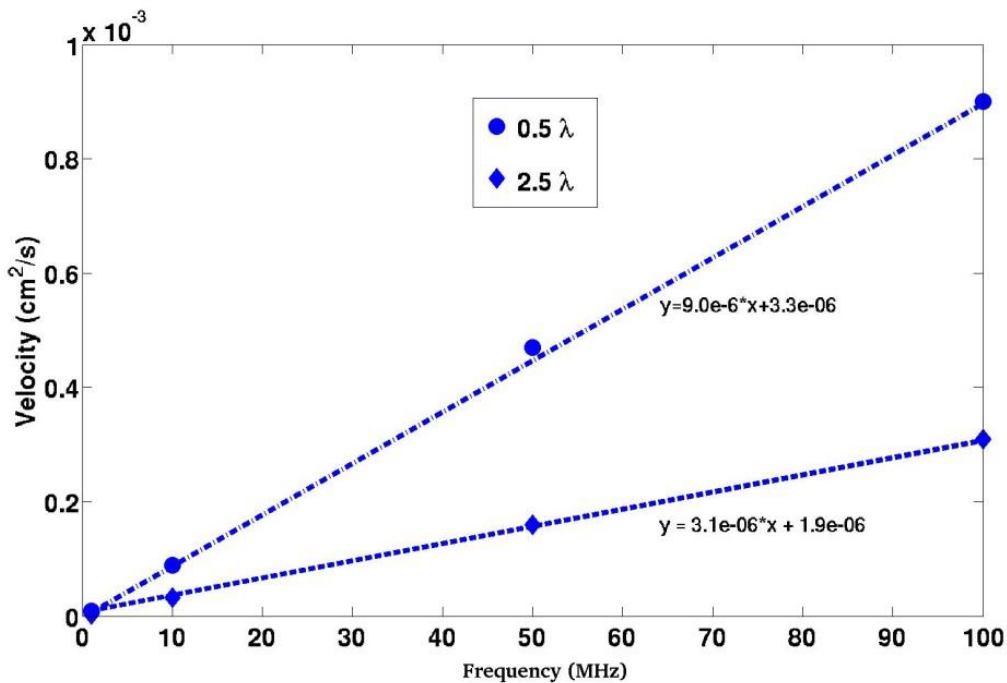


Figure 6.2 Streaming velocities along the delay path with respect to device frequency. Variation along two different region in the delay path is shown (a)  $0.5 \lambda$  (b)  $1.5 \lambda$ .

For a given applied voltage and device frequency, the removal of non-specifically bound proteins depends on the relative magnitudes of the adhesive and the removal forces involved. The principal adhesive forces are the van der Waals and electrical double layer involved in the binding of specific and non-specific proteins to the SAW surface. The magnitudes of these forces

are similar, especially for sub-micron particles and hence for the sake of comparison, it is usually sufficient to consider only the van der Waals force which is provided in Table 6.1 [172, 180].

The removal forces involved in NSB protein removal were estimated based on the streaming velocities given in Figure 6.2 (see section 6.2 for calculation details). The SAW direct force ( $F_{SAW}$ ) as well as lift ( $F_L$ ) and drag forces ( $F_{ST}$ ) generated for several SAW frequencies are given in Table 1. Our results show that for each frequencies studied, the direct SAW force ( $F_{SAW}$ ) is greater than adhesive forces ( $F_{vdw}$ ) by several orders of magnitude. Comparison of the computed direct SAW force ( $F_{SAW}$ ) at different frequencies shows this force increases as frequency decreases. Therefore, particles would be ejected into the fluid a greater distance at 10 MHz. Analysis of the other forces (lift ( $F_L$ ) and drag ( $F_{ST}$ )) presented in Table 6.1 reveal their magnitudes are insufficient to overcome adhesive forces at the surface by themselves. However, it was mentioned in section 6.2 that van der Waals force ( $F_{vdw}$ ) decreases with increasing  $z$  into the fluid. Thus, initial removal would occur via the direct SAW force ( $F_{SAW}$ ). Subsequently, particles would be removed from the surface, some distance  $z$ , to a region where the van der Waals force ( $F_{vdw}$ ) has diminished to a point where lift ( $F_L$ ) and drag forces ( $F_{ST}$ ) are strong enough to prevent particle reattachment. As a result, particle removal is maintained.

Table 6.1 Forces (in Newtons) as a function of device frequency. The particle radius is taken to be 1  $\mu\text{m}$  and applied voltage is 25 V.

<b>Force</b>	<b>10 MHz</b>	<b>50 MHz</b>	<b>100 MHz</b>
$F_{vdw}$	$2 \times 10^{-8}$	$2 \times 10^{-8}$	$2 \times 10^{-8}$
$F_{SAW}$	$2 \times 10^{-4}$	$8 \times 10^{-5}$	$1 \times 10^{-5}$
$F_L$	$4 \times 10^{-10}$	$2 \times 10^{-9}$	$4 \times 10^{-8}$
$F_{ST}$	$4 \times 10^{-10}$	$8 \times 10^{-10}$	$2 \times 10^{-9}$

## **6.5. Materials and Methods**

### ***6.5.1. SAW Device Fabrication***

A Rayleigh SAW device was fabricated on a ST-X Quartz wafer 0.5 mm thick and 100 mm diameter using standard lithography, metal evaporation and lift-off. Each IDT consisted of a Ti/Au film 20/80 nm thick and contained 60 finger pairs. The aperture height =  $50\lambda$  and the distance between IDTs is  $200\lambda$ . The operating wavelength,  $\lambda$ , is 40  $\mu\text{m}$ . This corresponds to an operating frequency of 78.95 MHz.

### ***6.5.2. Micropatterning the SAW Delay Path***

A square micropattern was applied to the entire delay path to differentiate between sensing and non-sensing areas (Figure 6.3 (a)) [98, 99]. Before applying the micropattern, SAW chips were rinsed with acetone, methanol, isopropanol, DI water, and dried with an  $\text{N}_2$  stream. Next, positive tone Microposit S1813 photoresist (Shipley) was spun on to the wafer at 3000 rpm for 40s followed by soft baking on a hotplate at 115°C for 60s. After cooling for ~ 5 min, the resist was exposed to broad band UV for 3 sec, at 25  $\text{mW}/\text{cm}^2$ . The substrate was then immersed in AZ 300 MIF Developer (Clariant) for 45s to define square windows to the substrate surface. This was followed by rinsing with DI water, drying with a stream of  $\text{N}_2$ , and plasma descumming (Harrick Plasma) for 5 min at the lowest setting. Lastly, the wafer was diced into individual die to be utilized in subsequent experiments.

### ***6.5.3. Surface Modification and Attachment of Capture Antibody***

An organosilane film ((3-glycidoxypropyl) dimethylethoxysilane (3-GPDMS) (Sigma Aldrich)), was used to functionalize exposed areas on the SAW device surface to immobilize the capture antibody (rabbit IgG (Sigma Aldrich)) (Figure 6.3 (b)). First, the SAW chip was immersed in 3-GPDMS (1 v/v %) in toluene for 1 hour. Next, the devices were thoroughly

rinsed with toluene, dried with a stream of N<sub>2</sub> and baked in an oven at 125°C for 1 hour to complete the hydrolysis reaction. Upon cooling, the photoresist was removed by immersing devices in acetone. Afterward, rabbit IgG (10 μL, 100 μg/mL) in PBS (pH 7.4) was applied to the center of the delay path for 45 minutes. This was followed by rinsing 3 times with PBS (pH 7.4) and drying with a stream of N<sub>2</sub>. To block the non-sensing regions BSA (10 μL, 1 mg/mL) in PBS (pH 7.4) was applied to the surface for 45 minutes (Figure 6.3 (c)), followed by rinsing three times with PBS (pH 7.4) and drying with N<sub>2</sub>.

#### ***6.5.4. Determination of Specific and Non-Specific Binding***

The determination of specific and non-specific binding in both sensing and non-sensing regions was accomplished by using fluorescently labeled antibodies. Thus, the extent that binding occurred was quantified from fluorescent intensity measurements. The specific protein (Alexa Fluor 488 goat anti- rabbit IgG (Molecular Probes)) was immobilized by covalent attachment to the silane layer (Figure 6.3 (c)). Alexa Fluor 488 goat anti-rabbit IgG (10 μL, 100 μg/mL) in PBS (pH 7.4), was applied to the SAW delay path center and left for 30 minutes. After incubation the devices were rinsed 3 times with PBS and imaged using a fluorescent microscope (Leica). After imaging, we applied a control (Alexa Fluor 488 donkey anti-mouse IgG (Molecular Probes)) to ascertain the degree in which non-specific binding occurs. Alexa Fluor 488 donkey anti-mouse IgG (10 μL, 100 μg/mL) in PBS (pH 7.4) was applied to the delay path center and left for 30 minutes. Similarly, after incubation the device was rinsed 3 times with PBS (pH 7.4) and fluorescent images were taken.

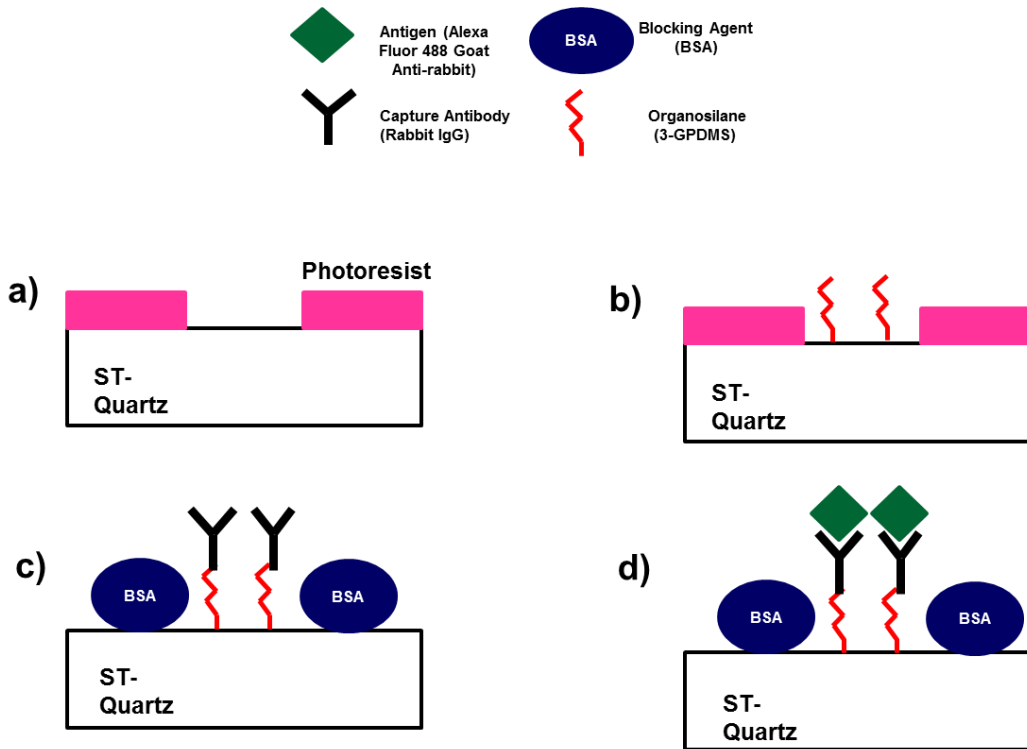


Figure 6.3 Processing steps to create patterned areas where specific binding occurs. (a) Photoresist is patterned to expose areas on ST-Quartz substrate. (b) Exposed areas are functionalized with organosilane film (3-GPDMS). (c) Capture antibody (rabbit IgG) is covalently immobilized and BSA is applied to block non-sensing areas. (d) Fluorescently tagged antigen (Alexa Fluor 488 goat anti-rabbit IgG) is specifically attached to capture antibody (rabbit IgG)

### 6.5.5. Fluorescent Imaging

Fluorescent images were taken with a Leica DMI 4000B fluorescent microscope (Leica Microsystems). Prior to imaging, the SAW device was inverted and mounted on a glass slide covered with a thin PBS film. A 20X objective lens along with a Leica DFC340-FX monochrome digital camera (Leica Microsystems) were used for all image capturing. The microscope had the following settings;  $\Gamma = 1.0$ , gain = 1.3, and exposure time = 3.6 sec. For Alexa Fluor 488 we used the I3 filter cube with an excitation filter having a band pass of 450-490 nm. Image analysis was done using ImageJ software. For quantitative analysis, we defined

signal as the fluorescent intensity of the sensing regions and background as the fluorescent intensity of the non-sensing regions.

#### **6.5.6. Protein Removal with Acoustic Energy**

An RF signal from an Agilent 8753 ES network analyzer (Agilent) was used to excite the SAW device at its center frequency in order to remove non-specifically bound proteins. To account for frequency shifts due to liquid loading or non-specific protein detachment, a 1 MHz bandwidth around the center frequency was used. The initial input power supplied to the device was 0 dBm. The input power multiplied by the excitation time (10 minutes) defines the dose. To see if the sensor surface could be regenerated, an amplified signal provided by a TIA-1000-1R8 RF broadband amplifier (Mini-Circuits) was inserted into the input signal path. The amplifier provided a 35 dB signal gain over the frequency range used to interrogate the SAW device. After application of RF power, the liquid was removed from the SAW device. Fluorescent images of the SAW delay path were taken and compared to images taken after a standard rinsing step.

### **6.6. Experimental Results and Discussion**

In this section we discuss the results from experimental trials involving a SAW device based on ST-Quartz that generates a Rayleigh wave mode in which its ability to remove non-specifically bound proteins from its surface was determined. Three scenarios were examined where protein removal with sound waves is desirable: 1) non-specific attachment of antigens in sensing and non-sensing areas; 2) non-specific attachment of an interfering species in sensing and non-sensing areas; and 3) specific attachment of antigens to its corresponding antibody in sensing areas.

### ***6.6.1. Removal of Non-Specifically Bound Antigen from Sensing and Non-Sensing Regions***

During biosensing, the antigen of interest can weakly bind to other antigens on the surface and to non-sensing areas producing an inflated response. Antigen (Alexa 488 goat anti-rabbit IgG) non-specifically bound to sensing and non-sensing areas were assessed by creating a micropattern, containing the capture antibody (rabbit IgG) in defined areas. To compare the amount of non-specific interaction two images were taken. First, a fluorescent image was taken after application of the antigen and completion of a standard rinsing step with PBS (Figure 6.4 (a)). Then, PBS (10  $\mu$ L) was placed on to the delay path and RF power was applied to the input of the SAW device for 10 minutes. After rinsing we obtained a second image of the SAW delay path (Figure 6.4 (c)). Figure 6.4 (a) shows that the square pattern we tried to obtain is occluded by a fluorescent signal of higher intensity occurring randomly over the entire surface, which is due the agglomeration of antigen molecules. In Figure 6.4 (c), taken after the application of acoustic energy, the fluorescent signal in random locations shown in Figure 6.4 (a) has been reduced significantly and the desired square pattern is clearly visible. The results suggest that antigens bind to other antigen molecules, which is evident by the high intensity signal caused by their agglomeration (Figure 6.4 (a)). In addition, antigens will also bind to sensing and non-sensing regions indiscriminately as seen by the randomness of the fluorescent signal shown in Figure 6.4 (a). After comparing the results in Figure 6.4 (a) and (c) we conclude that the antigen binding is relatively weak and can be characterized as non-specific. Furthermore, the results show that acoustic energy has the ability to remove weakly bound antigens where rinsing alone has failed. Not only has non-specifically bound material been removed, but antigens covalently immobilized to the patterned region stay intact (Figure 6.4 (c)). Thus, removal can be accomplished without disrupting specific binding between an antigen and its capture antibody.

To quantitatively determine the amount of antigen removed in both sensing and non-sensing regions, we averaged the fluorescent intensity for both areas before and after application of acoustic energy. The intensity values were normalized to values obtained before excitation of SAWs. Results given in Figure 6.4 (d) show that the fluorescent intensity decreased by 83% in the sensing areas and 86% in non-sensing areas.

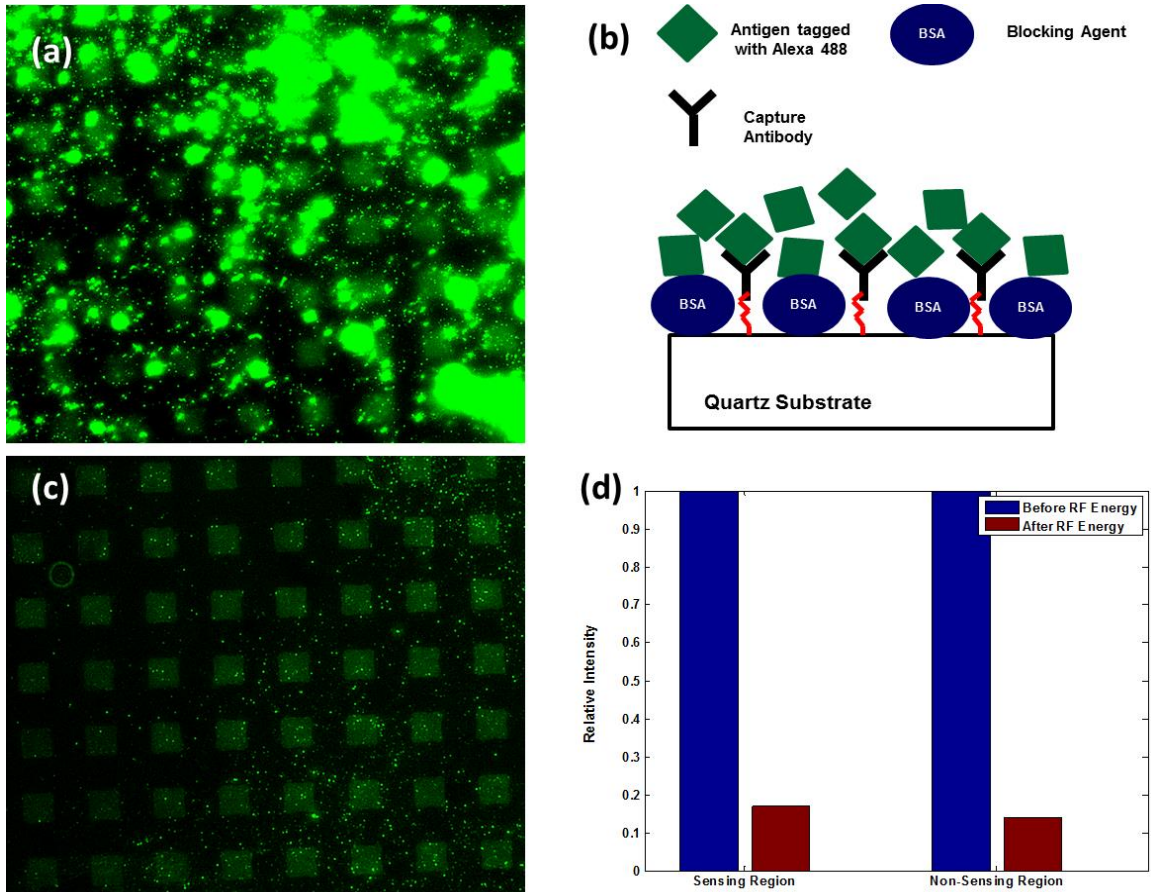


Figure 6.4 Results indicating the removal of non-specifically bound antigens (goat anti-rabbit IgG) from the SAW delay path. (a) Fluorescent intensity image shows binding of Alexa 488 tagged antigen (goat anti-rabbit IgG) to sensing and non-sensing regions after incubation and rinsing. (b) Illustration of experimental setup. (c) Fluorescent intensity image taken at the center of the delay path after applying acoustic energy to remove non-specifically bound antigen (goat anti-rabbit IgG) from sensing and non-sensing regions. (d) Plot of relative fluorescent intensity for sensing and non-sensing regions with respect to values obtained before application of acoustic energy.

### ***6.6.2. Removal of an Interfering Protein from Sensing and Non-Sensing Regions***

In many biosensing applications an interfering species will be present in the sample to be analyzed and these species can non-specifically bind to the sensor surface. Using a similar approach to the one in section 6.6.1., sensing and non-sensing regions are differentiated with a micropattern. To determine what extent an interfering species would non-specifically bind to sensing and non-sensing areas we applied Alexa Fluor 488 donkey anti-mouse IgG to the SAW delay path. To establish if a SAW can remove proteins that weakly bind to the surface we compared a fluorescent image after a standard rinsing step (Figure 6.5 (a)) to an image taken after applying acoustic energy (Figure 6.5 (c)). In this setup, antigens (goat anti-rabbit IgG) specifically bound in sensing regions were already present from the previous experiment. The results after application of the interfering species and rinsing with PBS are given in Figure 6.5 (a). Similar to the results presented in Figure 6.5 (a), we observed a fluorescent signal randomly distributed over the entire surface. A comparison of the Figure 6.5 (a) to Figure 6.5 (c) shows that the use of acoustic energy substantially reduces the fluorescent signal outside of the patterned region where specific binding occurs. Due to the reduction in the fluorescent signal over the entire area and maintenance of the fluorescent signal in areas where specific binding takes place, we attribute most of the randomly located signal to non-specific binding of the interfering species. Just like in section 6.6.1., these results show that SAWs removed non-specifically bound proteins and rinsing alone was not sufficient. To measure the reduction in fluorescent intensity due to the removal of non-specifically bound proteins, we plotted the intensities normalized to the value obtained before application of acoustic energy for both sensing and non-sensing regions (Figure 6.5 (d)). The fluorescent intensity was reduced by 35% in sensing regions and 94% in non-sensing areas. These results further indicate that non-specific

binding of the interfering species occurs in both areas and they can be effectively removed with acoustic energy.

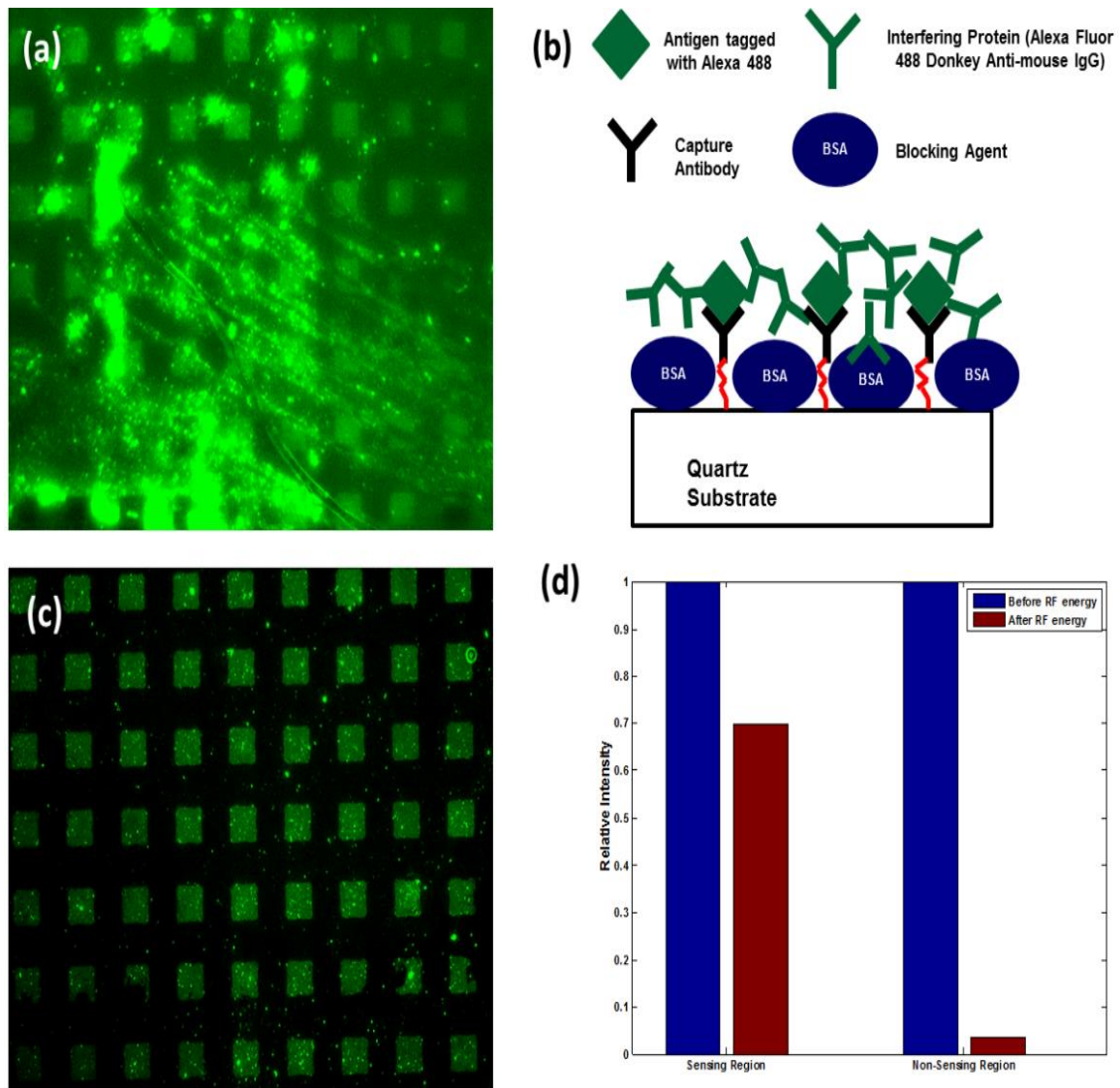


Figure 6.5 Results indicating the removal of an interfering protein (donkey anti-mouse IgG) from the SAW delay path. (a) Image of fluorescent intensity shows Alexa 488 tagged interfering protein (donkey anti-mouse IgG) binds to sensing and non-sensing regions after incubation and rinsing. (b) Illustration of the experimental setup. (c) Image of fluorescent intensity taken at the center of the delay path after applying acoustic energy. (d) Plot of relative fluorescent intensity for sensing and non-sensing regions with respect to values obtained before application of RF energy.

### ***6.6.3. Renewal of Sensor Surface***

Regeneration of a sensor surface for its subsequent reuse can reduce costs in certain instances. For immunosensing applications this would require rupturing the bond between the antigen and capture antibody. To determine if the antigen (goat anti-rabbit IgG) can be detached from its capture antibody (rabbit IgG) using acoustic energy, we increased the input signal to the SAW device by 35 while PBS (10  $\mu$ L) covered the delay path. To establish if the higher input power was effective in reversing antigen-antibody binding, we compared fluorescent images before and after generating SAWs. Figure 6.6 (a) is an image of the delay path after the conclusion of the experiment in section 6.6.2. At this point antigens are attached to their capture antibody in defined regions. Results after application of an amplified RF signal to the SAW input are shown in Figure 6.6 (b) and (c). The image in Figure 6.6 (b) is taken directly at the center of the SAW delay path. We observed that after application of acoustic energy the fluorescent intensity decreased. To quantify the relative decrease, we plotted the average intensity in the sensing areas normalized to the intensity before application of acoustic energy (Figure 6.6 (d)). Our results show that the average intensity in the sensing areas decreased by 71.6%. This indicates that antigen-antibody binding is disrupted. Because the SAW's energy is dissipated as it propagates into the fluid, removal efficiency is greater near the excitation source. This was tested by taking an image of the delay path close to the input IDT (Figure 6.6 (c)). Examination of Figure 6.6 (c) shows the fluorescent signal is barely visible. This illustrates that all antigens are possibly removed from their capture antibodies. However, it is conceivable that both capture antibodies and antigens have been removed from the organosilane film.

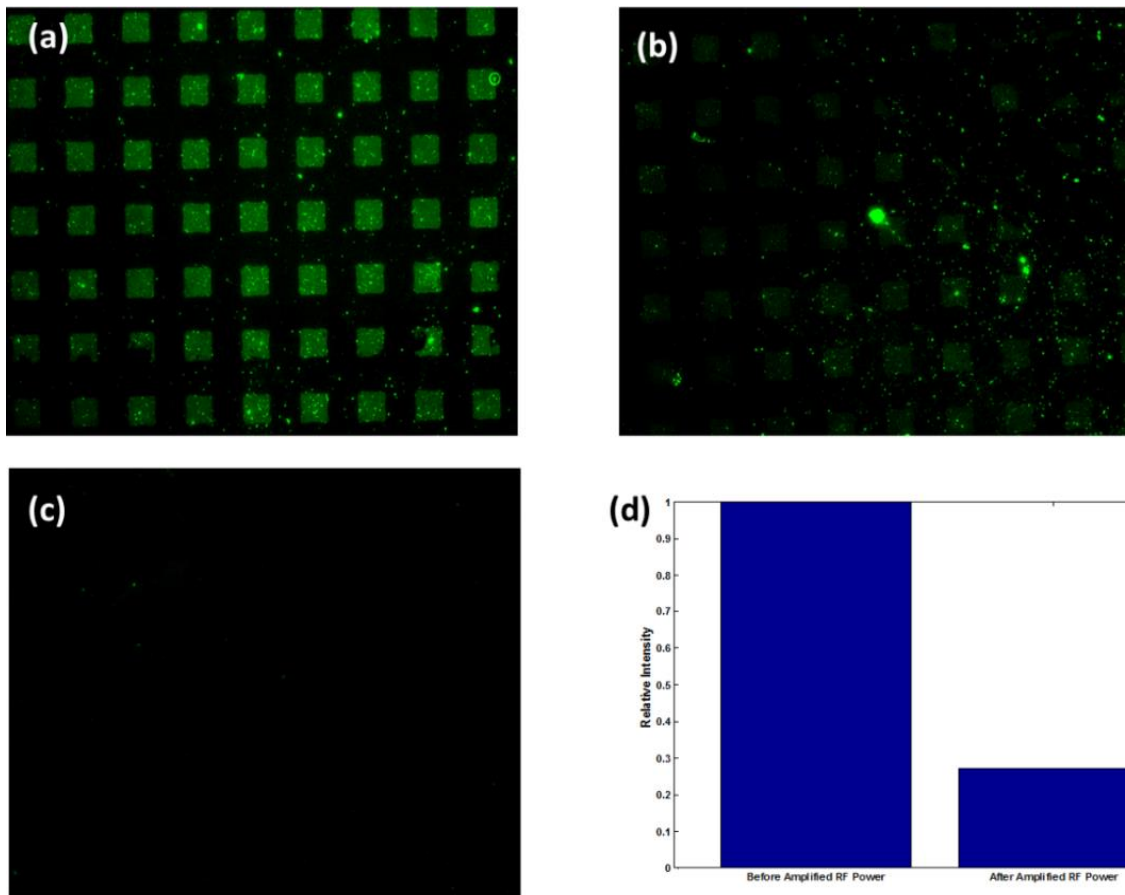


Figure 6.6 Results after applying an amplified RF signal to the SAW input. (a) Image of fluorescent intensity shows Alexa 488 tagged antigen (goat anti-rabbit IgG) bound to sensing regions after non-specifically bound proteins were removed with SAWs as outlined in section 5.2. (b) Image of fluorescent intensity at the middle of the delay path after applying an amplified RF signal. (c) Image of fluorescent intensity near the input IDT after applying an amplified RF signal. (d) Plot of relative fluorescent intensity for sensing regions with respect to values obtained before application of an amplified RF signal.

## 6.7. Conclusions

We performed a combined theoretical and experimental study to evaluate whether acoustically induced removal of non-specifically bound proteins is possible on a ST-Quartz substrate, which is a commonly used platform for biosensing. A coupled field FE FSI model was first used to predict SAW induced acoustic streaming forces. The various forces involved in NSB protein removal were computed based on predictions from our model and compared to adhesive

forces binding these non-specific proteins. For a range of SAW frequencies, computations show the SAW body force is sufficient to overcome adhesive forces between particles and the device surface. In addition, our models suggest that lift and drag forces permit continuous removal to occur by not allowing particle re-attachment.

Based on the predicted mechanism of removal, we carried out experimental investigations to successfully remove non-specifically bound antigens and interfering proteins using Rayleigh SAWs on ST-Quartz. A micropattern consisting of immobilized antibodies separated sensing areas from non-sensing areas, while the use of fluorescent tags allowed qualitative and quantitative verification. A comparison of fluorescent intensity values before and after acoustic excitation shows intensity is reduced by 83% in sensing areas and 86% in non-sensing areas, confirming the removal of NSB antigens using SAWs. Similarly, the removal of weakly bound interfering proteins was proved by a 35% and 94% reduction in fluorescent intensity in sensing and non-sensing areas respectively. Lastly, an amplified RF signal was applied to the SAW input to disrupt specific binding between antigens and capture antibodies. The corresponding fluorescent images showed that binding was disrupted in the middle of the delay path (71.6% reduction in fluorescent intensity) but was more effective near the input IDT (~100% reduction in fluorescent intensity).

The results presented in this work reveal that a standard rinsing technique and application of a blocking agent (BSA) are not adequate to prevent biofouling. Furthermore, the non-specific binding of interfering species and antigens produce an inflated response that can have negative implications in clinical applications. The demonstrated removal of NSB proteins using Rayleigh SAWs on ST-Quartz open up the possibility of an integrated SAW biosensor that can simultaneously eliminate biofouling and sense biomarkers.

## **CHAPTER 7: SIMULTANEOUS DETECTION AND REMOVAL OF NON-SPECIFICALLY BOUND PROTEINS USING ORTHOGONAL SURFACE ACOUSTIC WAVE TRANSDUCERS ON ST-QUARTZ**

The detection of adsorbed bovine serum albumin (BSA) and its subsequent removal was accomplished using orthogonally placed surface acoustic wave (SAW) transducers on ST-Quartz. The dual function SAW sensor was realized by fabricating two pairs of interdigital transducers (IDTs) on the same substrate. One IDT pair is aligned with the crystalline x-axis and excites a Rayleigh SAW mode, which was used for removal. The second pair of IDTs, oriented orthogonal to the x-axis, excites a shear-horizontally polarized wave and was used to detect surface changes from adsorption or de-adsorption of BSA. Removal efficiency was improved through the design of an input/output matching circuit for the Rayleigh wave mode. Our findings offer encouraging prospects for the design of a dual function biosensor that can be used to sense biomarkers in bodily fluids, where non-specific binding is presently an issue.

### **7.1. Introduction**

The field of clinical diagnostics is moving towards point-of-care testing (POCT) with miniaturized biosensors, where the sample is taken from the patient and placed onto a sensor in one step. The use of labels in sensing applications allows detection of analytes with high sensitivity and specificity. However, sensing can take up to several hours and detection cannot take place in real-time. In contrast, label-free sensing provides fast, real-time detection of a

biorecognition event that would be beneficial in POCT. The drawback is that label-free techniques do not have the ability to differentiate between responses caused by specific and non-specific interactions. Thus, sensor performance (i.e., limit of detection, sensitivity and dynamic range) is negatively affected. Currently, most reported sensing systems rely on a buffer solution containing an isolated antigen. However, for a biosensor to have commercial success in the clinical diagnostics market, sensing of biomarkers in complex fluids (i.e. serum, urine or blood) is required.

Surface acoustic wave devices have been routinely used as direct, label-free biosensors that monitor the interaction between a receptor and its target in real time through changes in the properties of the travelling wave (i.e. frequency, velocity, and/or amplitude)[53, 68, 72, 76, 85, 181]. Operation in liquid requires a shear-horizontal (SH) wave mode to minimize energy dissipation [46]. Several substrates with defined crystal cuts (i.e. 36° YX lithium tantalate (LiTaO<sub>3</sub>), ST-Quartz, 41° YX lithium niobate (LiNbO<sub>3</sub>), and langasite) meet this criterion and have been applied successfully in liquid sensing [56, 118, 136, 182]. Despite the advantageous properties of SH-SAW sensors, discrimination between specific and non-specific interactions is not possible. One approach to alleviate this problem is to use a dual-delay line setup [183, 184]. In this case, one delay-line is used for sensing and the other is used as a reference. This allows elimination of environmental effects common to both delay-lines from the final sensor response. However, this requires increased circuit complexity and would not account for the randomness of non-specific surface binding. Another alternative to eliminate unwanted interactions is to create inert/resistant surfaces through modification. Common approaches include use of detergents [185], blocking proteins (BSA) [163], or polymer films [165, 166]. Problems with these methods are increased setup time and costs, and compatibility issues with common sensing materials.

It is known that Rayleigh waves are not suitable for liquid sensing applications because mode conversion occurring from liquid loading causes severe attenuation [186]. However, acoustic streaming induced by Rayleigh SAWs in contact with a liquid has been shown to remove proteins weakly attached to the surface [99, 100, 106, 169]. The drawback of these studies is that the substrate ( $128^\circ$  YX LiNbO<sub>3</sub>) utilized does not support a SH-SAW. Thus, integration of removal with sensing requires a separate sensor platform. To address this issue, Singh *et al.* [100] simulated orthogonally placed transducers on langasite. By doing so, two different wave modes were shown to propagate (i.e. pure SH-SAW and Rayleigh wave). This would allow sensing and removal to be accomplished on the same substrate via SH-SAW and Rayleigh SAW respectively. However, an experimental device has not been realized to-date. Furthermore, langasite is expensive and extremely fragile so fabrication yield would be an issue. An alternative is to use ST-Quartz because it is more robust mechanically and less expensive. In addition, it supports both Rayleigh waves and a surface skimming bulk wave (SSBW) that has SH particle polarization [48, 187, 188]. Several investigators over the years have used the SSBW wave mode for biosensing in liquids [64, 69, 181]. Due to its propagation into the bulk of the substrate, a waveguide is usually applied to convert SSBW to a Love wave to increase sensitivity [12, 189]. Thus, ST-Quartz based biosensors usually exist in a layered configuration.

The mechanisms of ultrasonic removal of non-specifically bound proteins was elucidated by Sankaranarayanan *et al* [106, 169] using coupled field finite element (FE) fluid structure interaction (FSI) simulations. The simulations showed removal is possible if a SAW direct force is sufficient in strength to overcome adhesive forces (van der Waals and electrical double layer), and hydrodynamic forces (drag and lift) prevent particle re-attachment. A detailed description of the removal mechanism is given in Figure 7.1.

As elucidated in Figure 7.1, the force needed to initially overcome adhesive forces is based on SAW induced acoustic streaming. Most microfluidic applications that utilize SAWs are based on  $\text{LiNbO}_3$  instead of ST-Quartz [190]. This is due to its higher electromechanical coupling coefficient. With this in mind, it was unclear if Rayleigh waves generated on ST-Quartz could generate a force sufficient in strength to overcome NSB. In this study, it is shown that the Rayleigh waves generated in ST-quartz substrate are capable of removing NSB proteins.

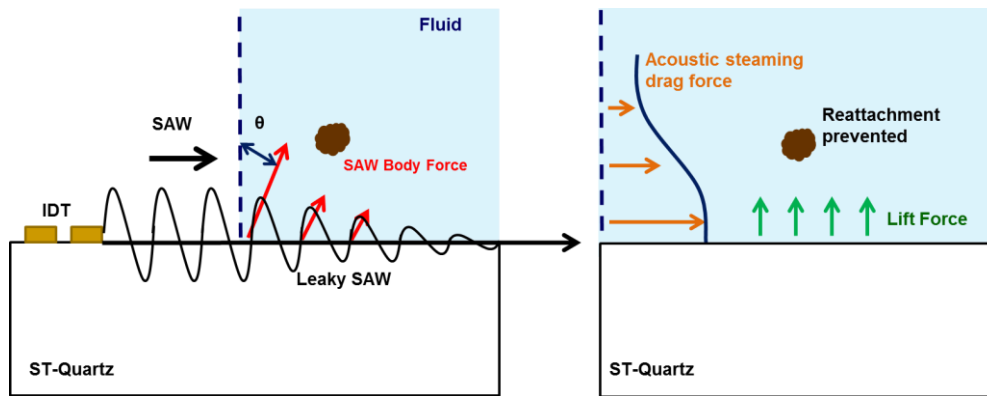


Figure 7.1 Coupled field FE FSI predicted mechanism of ultrasonic removal of particles weakly bound to a surface (i.e. NSB proteins). Simulations suggest that the interaction of the Rayleigh wave with the fluid medium results in a wave mode conversion into leaky SAW. This leaky SAW propagates along the boundary between the piezoelectric and the fluid loading and excites longitudinal waves into the fluid at a Rayleigh angle  $\theta$ . SAW direct forces result in initial particle detachment whereas hydrodynamic forces (i.e drag ( $F_{ST}$ ) and lift ( $F_L$ ) forces) prevent their reattachment. Image taken from Richardson *et al.* [191].

In the current work, two SAW delay lines are placed orthogonal to each other on an ST-Quartz substrate to simultaneously detect mass adsorption and de-adsorption, and to remove proteins non-specifically bound to the surface. One delay-line is oriented parallel to the crystalline x-axis and supports a Rayleigh wave (NSB removal) (Figure 7.2). The other delay-line is aligned normally to the first transducer along the y-axis and generates a SSBW (detection) (Figure 7.2). By combining removal and detection on a single substrate, utilizing one

transduction mechanism, a multifunctional Lab-on-a-Chip sensor is realized. The implication is that direct sensing of bodily fluids may be possible in the near future.

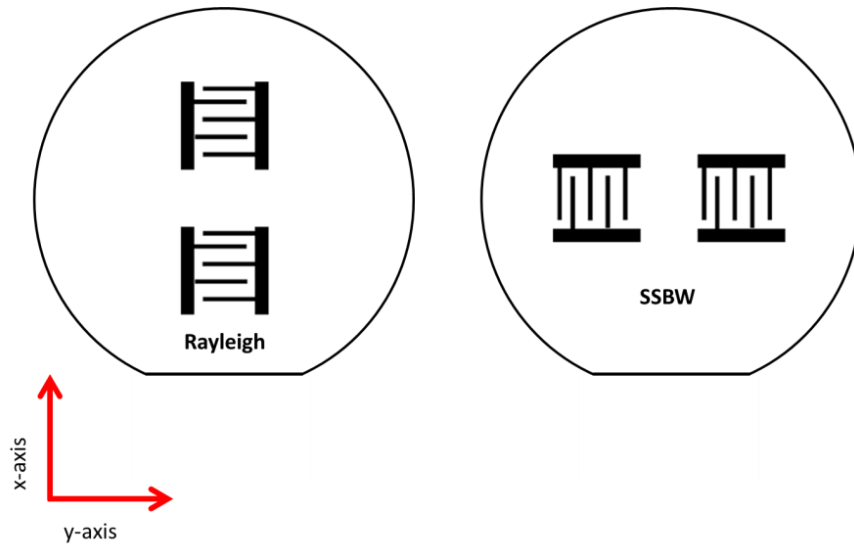
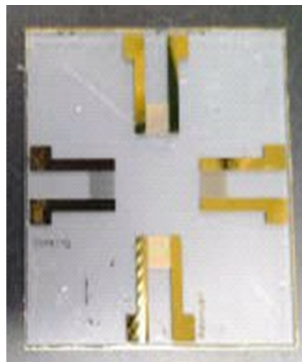


Figure 7.2 Illustration of the orientation of the SAW transducers for the two different wave modes with respect to the crystalline x-axis which is perpendicular to the wafer flat

## 7.2. Results and Discussion

The sensor was fabricated by a standard photolithography process and metal lift-off procedure (Figure 7.3 (a)). Identical SAW transducers comprised both delay lines. The IDTs have a split finger design with equal finger width and spacing ( $w = 10 \mu\text{m}$ ). The distance between IDTs for each delay line was 8 mm. The frequency response for each delay line was measured using an Agilent 8753ES network analyzer and are shown in Figure 7.3 (b) and (c). The measured center frequency was compared to theoretically derived values to verify if the expected wave modes are generated. Theoretical calculations were based on each mode's acoustic velocity (Rayleigh = 3158 m/sec and SSBW = 5060 m/sec) and acoustic wavelength ( $\lambda = 40 \mu\text{m}$ ). Comparisons between measured and theoretical values are shown in Table 7.1. Discrepancies between measured and theoretical values are due to mass loading of the IDTs and

misalignment of the transducers with the crystalline axes (x and y-axis). Since IDT mass loading for the transducer thickness deposited only results in a negative frequency shift, it will not adversely affect device operation. However, improper alignment of the IDTs with the crystalline axes (x or y-axis) results in increased IL, which hurts sensor performance. Steps to correct this issue are being addressed by inclusion of additional alignment marks on the photomask to align to the wafer flat.



(a)

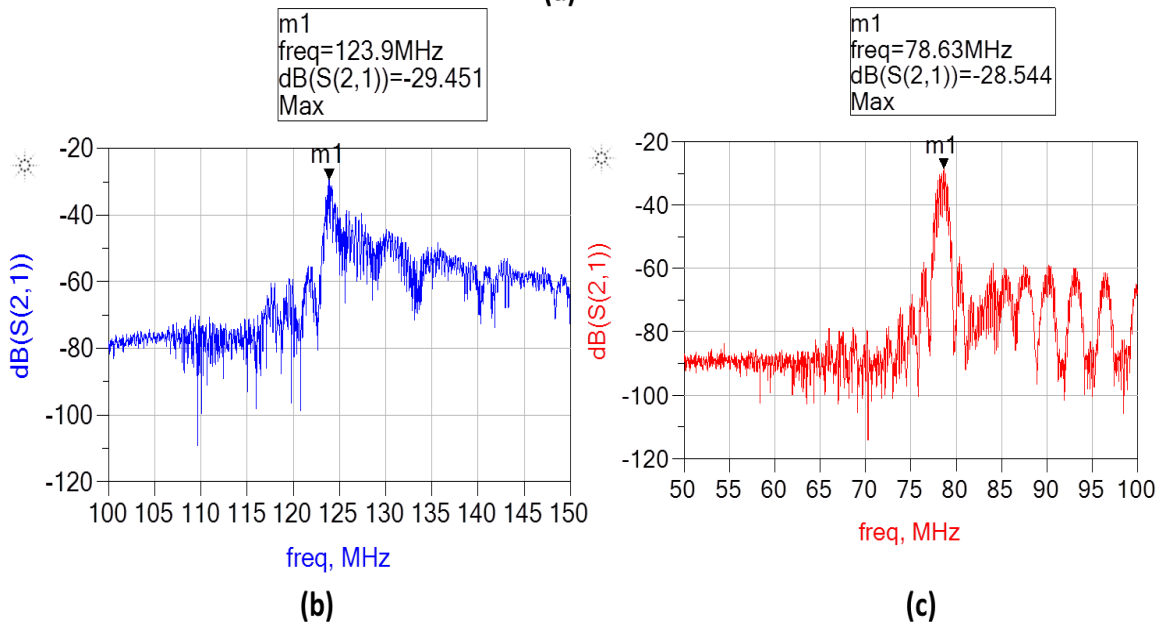


Figure 7.3 (a) Image of SAW device with orthogonally oriented transducers and measured frequency response of (b) SSBW wave mode and (c) Rayleigh wave mode

Table 7.1 Comparison between theoretical and measured center frequency values for each wave mode

<b>Wave mode</b>	<b>Theoretical Center Frequency (f<sub>0</sub>)</b>	<b>Experimental Center Frequency (f<sub>0</sub>)</b>
SSBW	126.5 MHz	123.9 MHz
Rayleigh	78.95 MHz	78.65 MHz

An investigation of the orthogonal SAW sensor to detect non-specific binding was carried out by applying a 5  $\mu\text{L}$  drop of BSA (200  $\mu\text{g}/\text{mL}$ ), in DI water, to the surface and monitoring the phase shift in real time. Before applying the BSA solution, the sensor had 15  $\mu\text{L}$  of DI water covering an area of 15.9  $\text{mm}^2$ . The use of an o-ring seal prevented the liquid from spreading. We used a droplet method over a flow through system to isolate removal due to SAW induced acoustic streaming. This eliminated the possibility of removal occurring from forces due to the flowing fluid. Experiments were conducted in which a 5  $\mu\text{L}$  drop of DI water was added to the system prior to applying the BSA solution to ensure no appreciable phase shift occurs from the added liquid volume. The sensing signal was provided by an Agilent 8753ES network analyzer and the phase was monitored with a computer interfaced with a GPIB and running a custom LabVIEW program. To determine removal of the non-specifically bound BSA, a separate signal source (Rhode & Schwartz SMA 100A signal generator) was used to excite the Rayleigh wave mode. The output power level was 15 dBm. This value was decided upon after running several experiments at various power levels (-5, 0, 5, and 10 dBm) and not getting any results. The signal from the source was applied to both IDTs by using a 50  $\Omega$ , 0° power splitter (Mini-Circuits Z99SC-62+). This was to ensure removal occurred over the entire delay path.

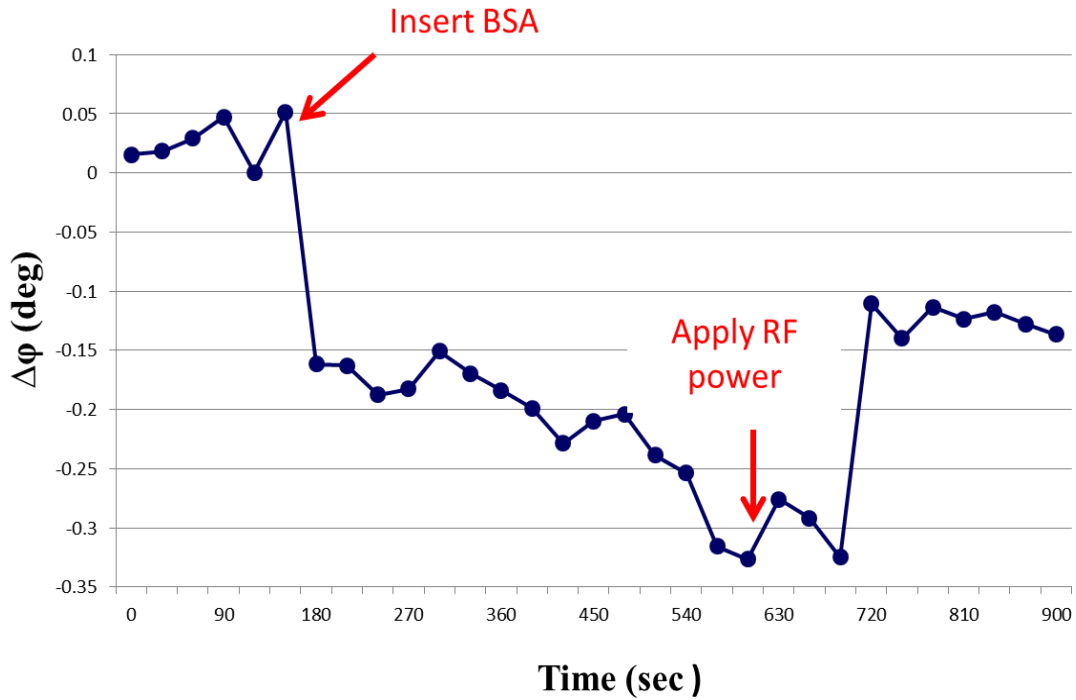


Figure 7.4 Plot of phase vs. time of the sensing path of the orthogonal SAW sensor during operation. The graph indicates when a 5  $\mu$ L BSA solution and RF signal are applied.

Figure 7.4 shows real-time binding and removal of BSA represented by the phase response curve for the SSBW mode. The plot shows soon after BSA is introduced the phase decreases, which corresponds to mass being adsorbed onto the surface. The phase continues to decrease until about 600 seconds after the experiment was initiated. At this time the Rayleigh wave is excited by applying an RF signal (15 dBm, 78.5 MHz) to the IDTs. After a delay of about 100 seconds, the phase shifts upwards due to mass being removed from the surface to a distance exceeding that where SAW sensing is effective. The absolute phase shift due to BSA adsorbing to the surface is approximately  $0.3^\circ$ . Removal of BSA from the surface results in an absolute phase shift of about  $0.2^\circ$ . The discrepancy between the phase shift obtained due to adsorption and that obtained due to removal indicates that all the mass is not removed from the surface.

To investigate if adsorbed BSA can be completely removed from the surface by increasing input power, we matched the Rayleigh wave delay line to 50  $\Omega$  impedances at each transducer port to reduce reflected power. Figure 7.5 shows the frequency response of the Rayleigh wave mode with and without matching.

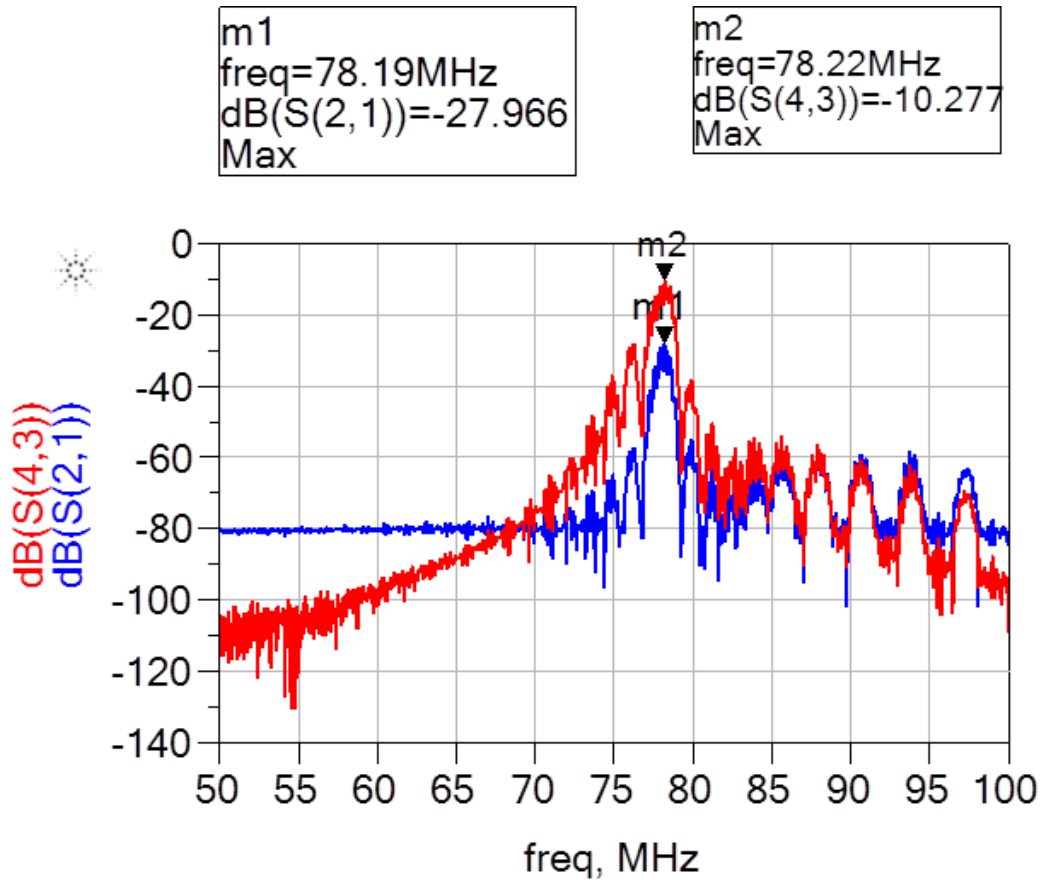


Figure 7.5 Frequency response of Rayleigh wave delay line with (red) and without (blue) conjugate matching of the input and output ports

The matching circuit was designed based on simultaneous matching of the SAW input and output using the measured 2-port S-parameters. We utilized an L section matching network with a series capacitor (4.7 pF) and a shunt inductor (222 nH). Application of the matching circuit decreased insertion loss by 17.689 dB. This method is preferred over amplifying the input signal because it keeps the power requirements low and prevents high power reflections back to the

source. In addition, excessive heating due to resistive losses at the IDT as a result of increased power from the source can be avoided. Figure 7.6 shows the real-time binding curve when the matching circuit is implemented. Similar to Figure 7.4, introduction of BSA immediately caused a decrease in phase that corresponds to its adsorption onto the surface. After the signal had stabilized (~600s), RF power (15 dBm, 78.5 MHz) was applied to the IDTs of the Rayleigh wave delay line. Immediately the phase increased due to removal of BSA from the surface. It is apparent from the plot that after excitation of the Rayleigh mode there is an overshoot past the original phase value. This can be attributed to decreased mass loading due to atomization or evaporation of some liquid because of the increased acoustic energy. At approximately 810 seconds, the RF power to the Rayleigh wave delay line was turned off. Analysis of the phase curve at this point indicates all the adsorbed mass is removed from the surface beyond the height where SAW detection is possible. Inspection of the curve shows that once the RF power is terminated, the phase decreases and eventually returns to phase value shown when BSA was completely adsorbed onto the surface. The process was run several times and the results were the same, thus confirming the repeatability of the process. To conclude, the phase shift due to BSA adsorption was  $\sim 0.3^\circ$ . This value is consistent with the result from the previous experiment. However, the phase shift due to removal was  $\sim 0.5 - 0.6^\circ$ , which demonstrates complete removal of BSA. The return of the phase curve to pre-RF input values is evidence that BSA re-adsorbed onto the surface. Thus, permanent removal of non-specifically bound species would require a rinsing step or continuous flow during operation.

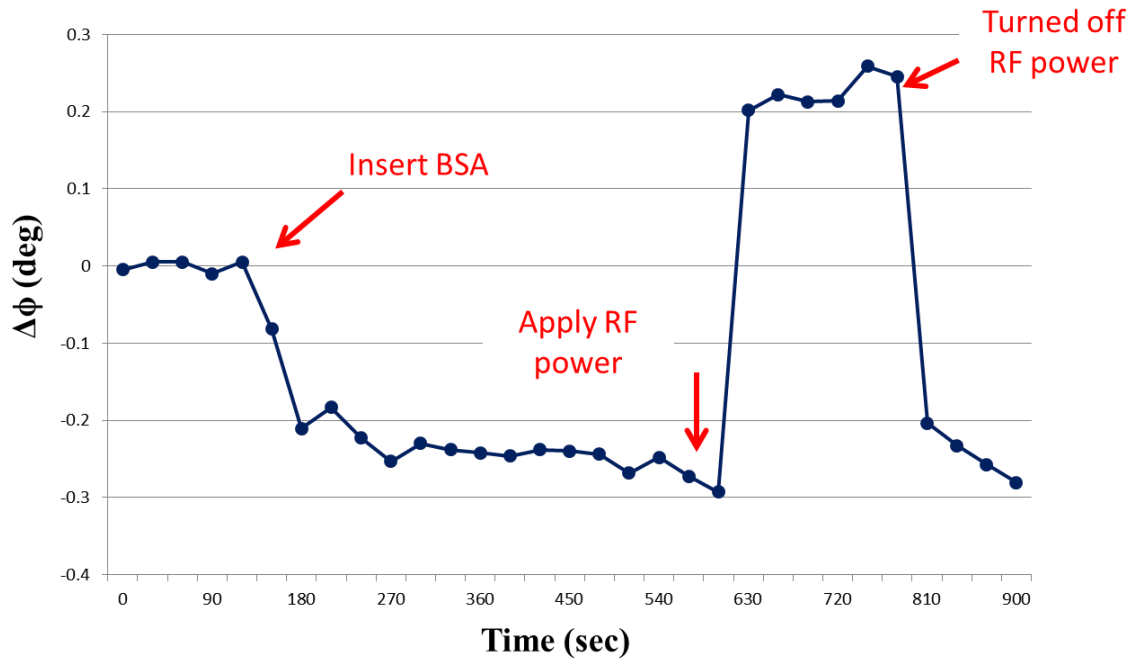


Figure 7.6 Plot of phase vs. time of the sensing path of the orthogonal SAW sensor during operation. The graph indicates when a 5  $\mu$ L BSA solution and RF signal are applied.

### 7.3. Conclusions

In summary, a SAW sensor with two delay lines oriented orthogonal to each other supporting two different wave modes (Rayleigh and SSBW) is presented. The phase response plotted in Figure 7.4 and 7.6 showed the SSBW mode can effectively detect BSA being adsorbed and de-adsorbed from the surface. In addition, Rayleigh SAW induced acoustic streaming removes non-specifically bound BSA. The ability of the sensor to simultaneously detect changes at its surface and remove weakly bound proteins could allow direct sensing of biomarkers in bodily fluids.

## CHAPTER 8: FUTURE WORK

### 8.1. Summary of Contributions

This dissertation is composed of two distinct parts. In the first part the modification of a surface acoustic wave (SAW) delay line device with an array of microcavities having square cross-sectional area was presented. Biosensing in liquids with SAW sensors is typically done with either  $36^\circ$  YX LiTaO<sub>3</sub> or  $90^\circ$  ST-X Quartz. These particular substrates support wave modes with shear-horizontal (SH) particle displacements. Since the particle displacements are parallel to the surface, minimal energy is dissipated into the adjacent fluid. However, as these waves travel away from their source, wave energy is lost within the substrate due to leakage or propagation into the bulk. As a result, these wave modes are termed leaky SAWs and surface skimming bulk waves (SSBWs) respectively. When they are used in sensing applications the loss of energy into the bulk decreases sensitivity to surface perturbations. To alleviate this problem a waveguide layer is usually applied to convert SSBWs and leaky SAWs into Love waves. As a result of having a waveguide, insertion loss (IL) is decreased and sensitivity is enhanced. One of the objectives of this work was to provide an alternative to applying a waveguide, thereupon improving its enhancement of power transfer and sensitivity. With this intention, the SAW delay path was modified with microcavities.

$36^\circ$  YX LiTaO<sub>3</sub> and ST-Quartz were examined because of their frequent use in biosensing applications. Observing that other studies showed filled microcavities performed better than unfilled microcavities [9, 100] has provided motivation to study other filling

materials. To aid in the comparison of different device configurations a finite element model (FEM) was employed. In chapter 4, ZnO and nanocrystalline diamond (NCD) were the filling materials chosen to insert into microcavities present in the delay path of a SAW device based on 36° YX LiTaO<sub>3</sub>. The results showed that ZnO filled microcavities with shallow depth (2.5 μm) were the most effective at reducing power loss ( $\Delta IL = 6.03$  dB). Also, the same design provided the highest sensitivity. In another study, detailed in chapter 5, tantalum and tungsten were inserted into cavities added to ST-Quartz. These materials were chosen because of their large density values, which results in high acoustic impedances. The goal was to reduce reflections from the microcavity array by minimizing the acoustic impedance mismatch between the inclusions (tantalum or tungsten) and the substrate (ST-Quartz). Thus, if reflections are reduced then the wave will propagate freely between SAW transducers. Our findings showed that microcavities with shallow depth ( $\leq 5\mu\text{m}$ ), filled with tantalum, successfully increased power transfer and confined the wave to the surface. Consequently, sensor sensitivity is improved. On the contrary, filling the microcavities with tungsten created a phononic bandgap around the SAW center frequency. At these frequencies acoustic waves were prohibited from propagating.

In summary, two improved SAW sensor designs have been realized. The first design consists of ZnO filled microcavities having a depth of  $\lambda/8$  added to 36° YX LiTaO<sub>3</sub>. The second design has tantalum filled microcavities ( $< 5 \mu\text{m}$  deep) inserted into the delay path of ST-Quartz. Both designs improved power transfer and wave confinement to the surface considerably. In the case where ZnO filled microcavities were inserted into 36° YX LiTaO<sub>3</sub>, mass sensitivity was greatly improved compared to a standard SAW design. In addition to the theoretical findings presented, it was shown that SAW devices containing microcavities can successfully be fabricated in both 36° YX LiTaO<sub>3</sub> and ST-Quartz. After comparing the measured frequency

responses for a device with and without cavities, it was shown that having cavities reduced IL. In conclusion, the device configurations presented in this work would be of interest to the sensor field for two reasons. One, power consumption is reduced resulting in decreased power requirements. This is beneficial for remote sensing applications. The second reason is sensitivity to surface perturbations is improved. As a result, the sensor's limit of detection is lowered. Thus, these devices can be used in clinical diagnostics where low concentrations need to be detected.

The second part of this dissertation dealt with the development of a multifunctional sensor that can remove biofouling and detect an analyte simultaneously. Healthcare providers are pushing for lower costs which would require fast accurate diagnostics of diseases. As a result there is a push for point of care testing (POCT). POCT are diagnostic tests performed in decentralized locations, outside of hospital laboratories or clinical laboratories. These tests don't require highly trained laboratory personnel but can be performed by physicians, nurses, assistants or EMTs. Sensor platforms for POCT need to be small, portable, easy to use, and inexpensive. With these things in mind, a sensor platform built around a SAW device can meet these requirements.

SAW sensors provide fast, real time detection without the use of labels. The issue with SAW sensors is that the responses from desired and undesired interactions cannot be discriminated. This is problematic when the sample to be tested is a biological fluid. In this case the sample contains various macromolecules other than the analyte of interest that can induce a response from the SAW device. Until now most sensing applications that utilize a SAW device take place in settings where an idealized sample (i.e. analyte isolated in buffer solution) is utilized. However, if these devices are to be used in POCT then it is desirable that bodily fluids

are detected directly. Therefore, sample prep is eliminated and sample prep and complexity is reduced. As a result, non-trained laboratory personnel can administer the test.

The issue that arises when testing bodily fluids is biofouling, which occurs from the non-specific binding of proteins or other biomolecules. The most common approach to combat biofouling is to modify the sensor surface to reduce non-specific binding that occurs from weak intermolecular forces. However, these techniques cannot be universally applied to all materials, adds steps and time to sample prep, and increases expenses. An alternative approach to remove loosely bound material is SAW induced acoustic streaming. The generated forces have been shown to effectively remove proteins non-specifically bound to the surface [99]. Even though this approach has proven to be successful, a multifunctional sensor cannot be realized without employing a separate sensing mechanism. To overcome this limitation a material that supports two different wave modes was chosen for this work. One wave mode (Rayleigh wave) is used to remove biofouling and the other wave mode (SSBW) is used for detection. By choosing a material that has these properties, the same transduction mechanism used for removal can be applied to detection. Because of this, the setup and electronics are simplified.

Prior to the work completed in this dissertation, Rayleigh waves generated in ST-quartz had been overlooked in microfluidic applications such as mixing, droplet manipulation, and microreactors because of its low electromechanical coupling coefficient ( $k^2$ ) compared to  $\text{LiNbO}_3$ . In chapter 6, it was shown that Rayleigh waves generated in ST-quartz can effectively remove biofouling. It was also shown in this study that surface cleaning using acoustic energy doesn't disrupt the specific binding between an antigen and antibody. Therefore, removal of biofouling with SAWs can be done in conjunction with immunosensing. In chapter 7 a multifunctional SAW device for biosensing applications was presented. The sensor consisted of

two pairs of IDTs oriented orthogonal to each other on an ST-Quartz substrate so that two different wave modes can be generated. The results from this investigation showed the sensor can detect the non-specific binding of BSA to its surface. Then when the surface is saturated, the BSA can be removed by exciting a Rayleigh wave with the appropriate input power. To the author's knowledge this is the first study that shows removal and sensing simultaneously with SAWs. The multifunctional sensor presented would be of great interest to the biosensing field because it has the potential to do fast and reliable sensing on a bodily fluid without the issues associated with biofouling.

## **8.2. Future Work**

The emphasis of all future work is to combine the best aspects of all the device configurations presented onto one sensor chip. Future work will also include integration of the best SAW sensor design practices such as using a waveguide and dual delay line sensing. The following material gives a brief description of some these concepts.

### ***8.2.1. SAW with Microcavities Combined with Waveguide***

Since the early 1990's waveguides applied to SAW sensors decreased IL and increased sensitivity [12, 189]. In this work and other recent studies [9, 192] an alternative method to using a waveguide has been presented. The delay path of a SAW device was modified by adding microcavities that also increased power transfer and sensitivity. Performance of microcavity based devices was improved by filling the cavities with certain materials (PMMA, ZnO, and tantalum). There still exists the possibility of using other filling material that can perform as well or better than those that were studied, such as SiO<sub>2</sub>. At the same time, the combination of a waveguide and microcavities should be a subject of future studies. There are several potential design configurations. One, design would contain a waveguide that covers the IDTs and the

delay path. In this scenario the waveguide material would also fill the cavities. Two other design alternatives have the waveguide only covering the IDTs. This sectional waveguide would leave the delay path uncovered. In this case the microcavities can be filled or unfilled. A comparative study of these device configurations is warranted based on the findings from this work and the work done by Cular *et al.* [9] and Singh *et al.* [192].

### **8.2.2. Microcavities Used as Reflectors**

Microcavities having the appropriate geometry so that the Bragg condition is met for the central frequency of the SAW being generated will block acoustic waves from propagating. Simulations have already been performed corroborating this. Since these microcavities block acoustic waves from traveling by reflecting the wave at the cavity substrate interface, they can be used as reflectors. The IDTs used in the sensor designs for this work are bi-directional. This means that the transducer generates waves in the forward and backward directions. A SAW delay line that uses these bi-directional IDTs at their input and output automatically suffer from 6 dB of IL before other losses are taken into account. The objective of a future project is to decrease IL using microcavities to reflect backward propagating waves excited by the IDT. Reflection of backward travelling waves with metal reflectors has been done. However, for Quartz the number of reflector required for total reflection of the wave is quite large due to its low electromechanical coupling coefficient. My hypothesis is that microcavities can reflect the SAW more efficiently with a fewer number of cavity columns than what can equivalently be done with reflectors. If successful, device size will be decreased substantially along with a decrease in IL.

### **8.2.3. Orthogonal SAW with Microcavities**

Currently, the orthogonal SAW design doesn't have its delay path modified. This leaves open the possibility to add microcavities. The inclusion of microcavities has already been shown to increase sensitivity to mass loading (Chapter 4 & 5). In addition, in a study by *Singh et al.* [192] it was shown that microcavities can increase SAW induced acoustic streaming which would improve biofouling removal capability. Therefore, addition of microcavities having the appropriate geometry can improve both the sensing and removal functions of an orthogonal SAW sensor.

### **8.2.4. Integration of a Dual Delay Line with the Orthogonal SAW Sensor**

The current orthogonal SAW configuration only contains one delay path for sensing. The inherent nature of SAW sensors is they are sensitive to various environmental factors and perturbations. Therefore, the sensor response due to the binding of an antigen to its antibody must be isolated. A common practice in SAW sensor design is to use two delay paths. One delay path is used as a reference and the other delay path contains the immobilized antibody and would be used for sensing. By monitoring the differential signal from the two delay paths, environmental effects common to both delay lines can be eliminated from the sensor response. Thus, the detection of the antigen binding to the antibody is singled out. By combining a dual delay line configuration with an orthogonally placed transducer, which will perform removal, would result in the accurate detection of an analyte in bodily fluids. Therefore, operators using the proposed sensor will have confidence that the sensor response is due just from the analyte of interest.

## REFERENCES

- [1] L. C. Clark and C. Lyons, "Electrode Systems for Continuous Monitoring in Cardiovascular Surgery," *Annals of the New York Academy of Sciences*, vol. 102, pp. 29- &, 1962.
- [2] B. E. Rapp, F. J. Gruhl, and K. Lange, "Biosensors with label-free detection designed for diagnostic applications," *Analytical and Bioanalytical Chemistry*, vol. 398, pp. 2403-2412, Dec 2010.
- [3] T. R. J. Holford, F. Davis, and S. P. J. Higson, "Recent trends in antibody based sensors," *Biosensors & Bioelectronics*, vol. 34, pp. 12-24, Apr 15 2012.
- [4] M. Mascini and S. Tombelli, "Biosensors for biomarkers in medical diagnostics," *Biomarkers*, vol. 13, pp. 637-657, 2008.
- [5] C. M. Lin, T. T. Wu, Y. Y. Chen, and T. T. Chou, "Improved frequency responses of saw filters with interdigitated interdigital transducers on ZnO/Diamond/Si layered structure," *Journal of Mechanics*, vol. 23, pp. 253-259, Sep 2007.
- [6] F. J. Gruhl, B. E. Rapp, and K. Länge, "Biosensors for Diagnostic Applications," *Advances in Biochemical Engineering/Biotechnology*, 2011.
- [7] "Biosensors Market-Global Industry Analysis, Size, Share, Growth, Trends and Forecasts, 2012-2018," ed: Transparency Market Research, 2011.
- [8] J. H. T. Luong, K. B. Male, and J. D. Glennon, "Biosensor technology: Technology push versus market pull," *Biotechnology Advances*, vol. 26, pp. 492-500, 2008.
- [9] S. Cular, S. K. R. S. Sankaranarayanan, and V. R. Bhethanabotla, "Enhancing effects of microcavities on shear-horizontal surface acoustic wave sensors: A finite element simulation study," *Applied Physics Letters*, vol. 92, Jun 16 2008.
- [10] R. L. Baer, C. A. Flory, M. Tom-Moy, and D. Solomon, "STW chemical sensors," in *Ultrasonics Symposium, 1992. Proceedings., IEEE 1992*, 1992, pp. 293-298 vol.1.
- [11] B. A. Auld and B. H. Yeh, "Theory of Surface Skimming SH Wave Guidance by a Corrugated Surface," in *1979 Ultrasonics Symposium, 1979*, pp. 786-790.

- [12] E. Gizeli, A. C. Stevenson, N. J. Goddard, and C. R. Lowe, "A Novel Love-Plate Acoustic Sensor Utilizing Polymer Overlayers," *Ieee Transactions on Ultrasonics Ferroelectrics and Frequency Control*, vol. 39, pp. 657-659, Sep 1992.
- [13] G. Kovacs, G. W. Lubking, M. J. Vellekoop, and A. Venema, "Love waves for (bio)-chemical sensing in liquids," in *IEEE 1992 Ultrasonics Symposium Proceedings*, 1992, pp. 281-285.
- [14] E. Simon, "Biological and chemical sensors for cancer diagnosis," *Measurement Science and Technology*, vol. 21, p. 112002, 2010.
- [15] A. P. F. Turner, "Biosensors: sense and sensibility," *Chemical Society Reviews*, vol. 42, pp. 3184-3196, 2013.
- [16] R. L. Bunde, E. J. Jarvi, and J. J. Rosentreter, "Piezoelectric quartz crystal biosensors," *Talanta*, vol. 46, pp. 1223-1236, Aug 1998.
- [17] T. M. H. Lee, "Over-the-counter biosensors: Past, present, and future," *Sensors*, vol. 8, pp. 5535-5559, Sep 2008.
- [18] R. Gabl, H. D. Feucht, H. Zeininger, G. Eckstein, M. Schreiter, R. Primig, D. Pitzer, and W. Wersing, "First results on label-free detection of DNA and protein molecules using a novel integrated sensor technology based on gravimetric detection principles," *Biosensors & Bioelectronics*, vol. 19, pp. 615-620, Jan 15 2004.
- [19] K. Mitsakakis and E. Gizeli, "Detection of multiple cardiac markers with an integrated acoustic platform for cardiovascular risk assesment," *Analytica Chimica Acta*, vol. 699, pp. 1-5, 2011.
- [20] M. Bisoffi, B. Hjelle, D. C. Brown, D. W. Branch, T. L. Edwards, S. M. Brozik, V. S. Bondu-Hawkins, and R. S. Larson, "Detection of viral bioagents using a shear horizontal surface acoustic wave biosensor," *Biosensors & Bioelectronics*, vol. 23, pp. 1397-1403, Apr 2008.
- [21] F. J. Gruhl and K. Länge, "Surface modification of an acoustic biosensor allowing the detection of low concentrations of cancer markers," *Analytical Biochemistry*, vol. 420, pp. 188-190, 2012.
- [22] F. J. Gruhl, M. Rapp, and K. Lange, "Label-free detection of breast cancer marker HER-2/neu with an acoustic biosensor," *Procedia Engineering*, vol. 5, pp. 914-917, 2010.
- [23] S. M. Brozik, "Low-level detection of a Bacillus anthracis simulant using Love-wave biosensors on 36 deg YX LiTaO," *Biosensors & Bioelectronics*, vol. 19, p. 11p, 2004.

- [24] M. Thompson and D. Stone, *Surface-launched acoustic wave sensors : chemical sensing and thin-film characterization / Michael Thompson and David C. Stone*: New York : Wiley, 1997., 1997.
- [25] A. Ballato, "Piezoelectricity - Old Effect, New Thrusts," *Ieee Transactions on Ultrasonics Ferroelectrics and Frequency Control*, vol. 42, pp. 916-926, Sep 1995.
- [26] G. T. A. Kovacs, *Micromachined transducers sourcebook / Gregory T.A. Kovacs*: Boston, Ma. : WCB, 1998., 1998.
- [27] B. Drafts, "Acoustic wave technology sensors," *Ieee Transactions on Microwave Theory and Techniques*, vol. 49, pp. 795-802, Apr 2001.
- [28] R. M. White and F. W. Voltmer, "DIRECT PIEZOELECTRIC COUPLING TO SURFACE ELASTIC WAVES," *Applied Physics Letters*, vol. 7, pp. 314-316, 1965.
- [29] J. D. Maines and E. G. S. Paige, "Surface-acoustic-wave components, devices and applications," *Electrical Engineers, Proceedings of the Institution of*, vol. 120, pp. 1078-1110, 1973.
- [30] C. K. Campbell and C. B. Saw, "Analysis and Design of Low-Loss Saw Filters Using Single-Phase Unidirectional Transducers," *Ieee Transactions on Ultrasonics Ferroelectrics and Frequency Control*, vol. 34, pp. 357-367, May 1987.
- [31] P. Das, C. Lanzl, and D. Barone, "A Surface Acoustic Wave Transmitting Hydrophone," in *1978 Ultrasonics Symposium*, 1978, pp. 458-463.
- [32] T. M. Reeder, D. E. Cullen, and M. Gilden, "SAW OSCILLATOR PRESSURE SENSORS," in *Ultrasonics Symposium 1975*, pp. 264-268.
- [33] T. M. Reeder and D. E. Cullen, "Surface-acoustic-wave pressure and temperature sensors," *Proceedings of the IEEE*, vol. 64, pp. 754-756, 1976.
- [34] J. F. Dias and H. E. Karrer, "Stress effects in acoustic wave circuits and applications to pressure and force transducers," in *IEEE Solid State Circuits Conference*, 1974.
- [35] H. Wohltjen and R. Dessy, "Surface acoustic wave probes for chemical analysis. III. Thermomechanical polymer analyzer," *Analytical Chemistry*, vol. 51, pp. 1470-1475, 1979/08/01 1979.
- [36] H. Wohltjen and R. Dessy, "Surface acoustic wave probe for chemical analysis. I. Introduction and instrument description," *Analytical Chemistry*, vol. 51, pp. 1458-1464, 1979/08/01 1979.

- [37] M. S. Nieuwenhuizen and A. J. Nederlof, "A SAW gas sensor for carbon dioxide and water. Preliminary experiments," *Sensors and Actuators B: Chemical*, vol. 2, pp. 97-101, 1990.
- [38] Y. J. Lee, H. B. Kim, Y. R. Roh, H. M. Cho, and S. Baik, "Development of a saw gas sensor for monitoring SO<sub>2</sub> gas," *Sensors and Actuators A: Physical*, vol. 64, pp. 173-178, 1998.
- [39] A. J. Ricco, S. J. Martin, and T. E. Zipperian, "Surface acoustic wave gas sensor based on film conductivity changes," *Sensors and Actuators*, vol. 8, pp. 319-333, 1985.
- [40] J. E. Roederer and G. J. Bastiaans, "Microgravimetric Immunoassay with Piezoelectric Crystals," *Analytical Chemistry*, vol. 55, pp. 2333-2336, 1983.
- [41] G. S. Calabrese, H. Wohltjen, and M. K. Roy, "Surface Acoustic-Wave Devices as Chemical Sensors in Liquids - Evidence Disputing the Importance of Rayleigh-Wave Propagation," *Analytical Chemistry*, vol. 59, pp. 833-837, Mar 15 1987.
- [42] G. S. Calabrese, "Surface Acoustic Wave Devices as Chemical Sensors in Liquids. Evidence Disputing the Importance of Rayleigh Wave Propagation," *Analytical Chemistry*, vol. 59, pp. 833-837, 1987.
- [43] I. Mannelli, M. Minunni, S. Tombelli, and M. Mascini, "Quartz crystal microbalance (QCM) affinity biosensor for genetically modified organisms (GMOs) detection," *Biosensors and Bioelectronics*, vol. 18, pp. 129-140, 2003.
- [44] M. Z. Atashbar, B. Bejcek, A. Vijh, and S. Singamaneni, "QCM biosensor with ultra thin polymer film," *Sensors and Actuators B: Chemical*, vol. 107, pp. 945-951, 2005.
- [45] D. S. Ballantine, R. M. White, S. J. Martin, A. J. Ricco, E. T. Zellers, G. C. Frye, and H. Wohltjen, *Acoustic Wave Sensors: Theory, Design, and Physico-Chemical Applications*: Academic Press, 1997.
- [46] K. Lange, B. E. Rapp, and M. Rapp, "Surface acoustic wave biosensors: a review," *Analytical and bioanalytical chemistry*, vol. 391, pp. 1509-1519, 2008.
- [47] S. J. Martin, A. J. Ricco, T. M. Niemczyk, and G. C. Frye, "Characterization of SH acoustic plate mode liquid sensors," *Sensors and Actuators*, vol. 20, pp. 253-268, 1989.
- [48] C. K. Campbell, *Surface Acoustic Wave Devices for Mobile and Wireless Communications*: Academic Press, 1998.
- [49] L. Fertier, M. Cretin, M. Rolland, J.-O. Durand, L. Raehm, R. Desmet, O. Melnyk, C. Zimmermann, C. Déjous, and D. Rebière, "Love wave immunosensor for antibody recognition using an innovative semicarbazide surface functionalization," *Sensors and Actuators B: Chemical*, vol. 140, pp. 616-622, 2009.

- [50] M. D. Schlenzog, T. M. A. Gronewold, M. Tewes, M. Famulok, and E. Quandt, "A Love-wave biosensor using nucleic acids as ligands," *Sensors and Actuators B: Chemical*, vol. 101, pp. 308-315, 2004.
- [51] E. Gizeli, "Study of the sensitivity of the acoustic waveguide sensor," *Analytical Chemistry*, vol. 72, pp. 5967-5972, Dec 15 2000.
- [52] E. Gizeli, F. Bender, A. Rasmusson, K. Saha, F. Josse, and R. Cernosek, "Sensitivity of the acoustic waveguide biosensor to protein binding as a function of the waveguide properties," *Biosensors & Bioelectronics*, vol. 18, pp. 1399-406, Oct 1 2003.
- [53] D. W. Branch and S. M. Brozik, "Low-level detection of a Bacillus anthracis simulant using Love-wave biosensors on 36 degrees YX LiTaO<sub>3</sub>," *Biosensors & Bioelectronics*, vol. 19, pp. 849-859, Mar 15 2004.
- [54] G. Kovacs and A. Venema, "Theoretical Comparison of Sensitivities of Acoustic Shear-Wave Modes for (Bio)Chemical Sensing in Liquids," *Applied Physics Letters*, vol. 61, pp. 639-641, Aug 10 1992.
- [55] T. I. Browning and M. F. Lewis, "A New Class of Quartz Crystal Oscillator Controlled by Surface-Skimming Bulk Waves," in *31st Annual Symposium on Frequency Control*, 1977, 1977, pp. 258-265.
- [56] T. Moriizumi and Y. Unno, "New sensor in Liquid using Leaky SAW," *Ultrasonics Symposium*, pp. 579-582, 1987.
- [57] J. Du, G. L. Harding, J. A. Ogilvy, P. R. Dencher, and M. Lake, "A study of love-wave acoustic sensors," *Sensors and Actuators a-Physical*, vol. 56, pp. 211-219, Sep 1996.
- [58] J. Du, G. L. Harding, A. F. Collings, and P. R. Dencher, "An experimental study of Love-wave acoustic sensors operating in liquids," *Sensors and Actuators A: Physical*, vol. 60, pp. 54-61, 1997.
- [59] H.-K. Oh, W. Wang, K. Lee, and C. Min, "The development of a wireless Love wave biosensor on 41 YX LiNbO<sub>3</sub>," *Smart Materials and Structures*, vol. 18, 2008.
- [60] P. Roach, M. I. Newton, and G. McHale, "Love Wave Sensors: Sectional Guiding Layers," presented at the 2008 IEEE International Frequency Control Symposium, 2008.
- [61] J. Zhao, C. Jiang, Y. Chen, H. Li, and S. He, "A study of Love wave sensors with SU-8 guiding layers," presented at the 2008 IEEE Ultrasonics Symposium, 2008.
- [62] V. Blondeau-Patissier, C. Elie-Caille, L. El Fissi, J. M. Friedt, and S. Ballandras, "Monitoring bio-molecular vesicle interactions in liquid using Love-wave sensors," *Procedia Chemistry*, vol. 1, pp. 1075-1078, 2009.

- [63] F.-m. Zhou, Z. Li, L. Fan, S.-y. Zhang, and X.-j. Shui, "Experimental study of Love-wave immunosensors based on ZnO/LiTaO<sub>3</sub> structures," *Ultrasonics*, vol. 50, pp. 411-415, 2010.
- [64] K. K. Zadeh, A. Trinchì, W. Włodarski, and A. Holland, "A novel Love-mode device based on a ZnO/ST-cut quartz crystal structure for sensing applications," *Sensors and Actuators A: Physical*, vol. 100, pp. 135-143, 2002.
- [65] W. Water, R.-Y. Zhao, L.-W. Ji, T.-H. Fang, and S.-E. Chen, "Love wave ultraviolet photodetector using ZnO nanorods synthesized on 90°-rotated ST-cut (42°45') quartz," *Sensors and Actuators A: Physical*, vol. 161, pp. 6-11, 2010.
- [66] Y. Q. Fu, J. K. Luo, X. Y. Du, A. J. Flewitt, Y. Li, G. H. Markx, A. J. Walton, and W. I. Milne, "Recent developments on ZnO films for acoustic wave based bio-sensing and microfluidic applications: a review," *Sensors and Actuators B: Chemical*, vol. 143, pp. 606-619, 2010.
- [67] R.-C. Chang, S.-Y. Chu, C.-S. Hong, and Y.-T. Chuang, "A study of Love wave devices in ZnO/Quartz and ZnO/LiTaO<sub>3</sub> structures," *Thin Solid Films*, vol. 498, pp. 146-151, 2006.
- [68] E. Berkenpas, P. Millard, and M. Pereira da Cunha, "Detection of Escherichia coli O157:H7 with langasite pure shear horizontal surface acoustic wave sensors," *Biosensors & Bioelectronics*, vol. 21, pp. 2255-62, Jun 15 2006.
- [69] D. Deobagkar, "Acoustic wave immunosensing of Escherichia coli in water," *Sensors and Actuators B: Chemical*, vol. 104, pp. 85-89, 2005.
- [70] E. Howe and G. Harding, "A comparison of protocols for the optimisation of detection of bacteria using a surface acoustic wave (SAW) biosensor," *Biosensor & Bioelectronics*, vol. 15, pp. 641-649, 2000.
- [71] N. Moll, E. Pascal, D. H. Dinh, J.-P. Pillot, B. Bennetau, D. Rebière, D. Moynet, Y. Mas, D. Mossalayi, J. Pistré, and C. Déjous, "A Love wave immunosensor for whole E. coli bacteria detection using an innovative two-step immobilisation approach.," *Biosensors & bioelectronics*, vol. 22, pp. 2145-50, 2007.
- [72] T. M. A. Gronewold, A. Baumgartner, E. Quandt, and M. Famulok, "Discrimination of Single Mutations in Cancer-Related Gene Fragments with a Surface Acoustic Wave Sensor," *Analytical Chemistry*, vol. 78, pp. 4865-4871, 2006/07/01 2006.
- [73] Y. Hur, J. Han, J. Seon, Y. Pak, and Y. Roh, "Development of an SH-SAW sensor for the detection of DNA hybridization," *Sensors and Actuators A: Physical*, vol. 120, pp. 462-467, 2005.

- [74] J. Sakong, H. Roh, and Y. Roh, "Surface Acoustic Wave DNA Sensor with Micro-Fluidic Channels," *Japanese Journal of Applied Physics*, vol. 46, pp. 4729-4733, 2007.
- [75] J. Sakong, Y. Roh, and H. Roh, "3F-2 SAW Sensor System with Micro-Fluidic Channels to Detect DNA Molecules," *2006 IEEE Ultrasonics Symposium*, pp. 548-551, 2006.
- [76] M. Schlensog, "A Love-wave biosensor using nucleic acids as ligands," *Sensors and Actuators B: Chemical*, vol. 101, pp. 308-315, 2004.
- [77] A. Tsortos, G. Papadakis, K. Mitsakakis, K. a. Melzak, and E. Gizeli, "Quantitative determination of size and shape of surface-bound DNA using an acoustic wave sensor.," *Biophysical journal*, vol. 94, pp. 2706-15, 2008.
- [78] C. Zerrouki, N. Fourati, R. Lucas, J. Vergnaud, J.-M. Fournion, R. Zerrouki, and C. Pernelle, "Biological investigation using a shear horizontal surface acoustic wave sensor: small "Click generated" DNA hybridization detection.," *Biosensors & bioelectronics*, vol. 26, pp. 1759-62, 2010.
- [79] P. Bröker, K. Lücke, M. Perpeet, and T. M. A. Gronewold, "A nanostructured SAW chip-based biosensor detecting cancer cells," *Sensors and Actuators B: Chemical*, vol. 165, pp. 1-6, 2012.
- [80] O. Tigli, L. Bivona, P. Berg, and M. E. Zaghoul, "Fabrication and Characterization of a Surface-Acoustic-Wave Biosensor in CMOS Technology for Cancer Biomarker Detection," *IEEE Transactions on Biomedical Circuits and Systems*, vol. 4, pp. 62-73, 2010.
- [81] D. Wang, K. Yu, Y. Wang, C. Zhao, L. Wang, P. Wang, and P. Gouma, "An Electronic Nose Based on Hybrid MOS-SAW Sensors for Detection of Different Biomarkers of Lung Cancer," vol. 2, pp. 161-162, 2011.
- [82] C. Zerrouki, N. Fourati, R. Lucas, J. Vergnaud, J.-M. Fournion, R. Zerrouki, and C. Pernelle. "Biological investigation using a shear horizontal surface acoustic wave sensor: small "click generated" DNA hybridization," *Biosensors and Bioelectronics*, vol. 26, pp. 1759-62, 2010.
- [83] N. Moll, E. Pascal, D. H. Dinh, J. P. Pillot, B. Bennetau, D. Rebiere, D. Moynet, Y. Mas, D. Mossalayi, J. Pistre, and C. Dejous, "A Love wave immunosensor for whole E-coli bacteria detection using an innovative two-step immobilisation approach," *Biosensors & Bioelectronics*, vol. 22, pp. 2145-2150, Apr 15 2007.
- [84] S. Srivastava, M. Verma, and D. E. Henson, "Biomarkers for Early Detection of Colon Cancer," *Clinical Cancer Research*, vol. 7, pp. 1118-1126, 2001.

- [85] O. Onen, A. Sisman, N. D. Gallant, P. Kruk, and R. Guldiken, "A Urinary Bcl-2 Surface Acoustic Wave Biosensor for Early Ovarian Cancer Detection," *Sensors*, vol. 12, pp. 7423-7437, 2012.
- [86] X. Chen, M. Cao, Y. Li, W. Hu, P. Wang, K. Ying, and H. Pa, "A study of an electronic nose for detection of lung cancer based on virtual SAW gas sensors in array and imaging recognition method," *Measurement Science and Technology*, vol. 16, 2005.
- [87] E. Brynda, M. Houska, a. Brandenburg, and a. Wikerstål, "Optical biosensors for real-time measurement of analytes in blood plasma.," *Biosensors & bioelectronics*, vol. 17, pp. 665-75, 2002.
- [88] R. Dahint, F. Bender, and F. Morhard, "Operation of acoustic plate mode immunosensors in complex biological media," *Analytical Chemistry*, vol. 71, pp. 3150-3156, Aug 1 1999.
- [89] G. Markovic, T. Mutschler, K. Wollner, and G. Gauglitz, "Application of surface acoustic waves for optimisation of biocompatibility of carboxymethylated dextran surfaces," *Surface & Coatings Technology*, vol. 201, pp. 1282-1288, Oct 5 2006.
- [90] T. Tamura, T. Terada, and A. Tanaka, "A quantitative analysis and chemical approach for the reduction of nonspecific binding proteins on affinity resins," *Bioconjugate Chemistry*, vol. 14, pp. 1222-1230, Nov-Dec 2003.
- [91] N. A. Alcantar, E. S. Aydil, and J. N. Israelachvili, "Polyethylene glycol-coated biocompatible surfaces," *Journal of Biomedical Materials Research*, vol. 51, pp. 343-351, Sep 5 2000.
- [92] D. R. Miller and N. A. Peppas, "Diffusional Effects during Albumin Adsorption on Highly Swollen Poly(vinyl-Alcohol) Hydrogels," *European Polymer Journal*, vol. 24, pp. 611-615, 1988.
- [93] E. Iwaoka, T. Mori, T. Shimizu, K. Hosoya, and A. Tanaka, "Improvement of monolithic solid material by utilization of spacer for identification of the target using affinity resins," *Bioorganic & Medicinal Chemistry Letters*, vol. 19, pp. 1469-1472, Mar 1 2009.
- [94] S. D. Bruck, "Aspects of three types of hydrogels for biomedical applications," *Journal of Biomedical Materials Research*, vol. 7, pp. 387-404, 1973.
- [95] J. Piehler, A. Brecht, K. E. Geckeler, and G. Gauglitz, "Surface modification for direct immunoprobes," *Biosensors & Bioelectronics*, vol. 11, pp. 579-590, 1996.
- [96] S. Herrwerth, T. Rosendahl, C. Feng, J. Fick, W. Eck, M. Himmelhaus, R. Dahint, and M. Grunze, "Covalent coupling of antibodies to self-assembled monolayers of carboxy-functionalized poly(ethylene glycol): Protein resistance and specific binding of biomolecules," *Langmuir*, vol. 19, pp. 1880-1887, Mar 4 2003.

- [97] S. Rupp, M. von Schickfus, S. Hunklinger, H. Eipel, A. Priebe, D. Enders, and A. Pucci, "A shear horizontal surface acoustic wave sensor for the detection of antigen-antibody reactions for medical diagnosis," *Sensors and Actuators B-Chemical*, vol. 134, pp. 225-229, Aug 28 2008.
- [98] G. D. Meyer, J. M. Moran-Mirabal, D. W. Branch, and H. G. Craighead, "Nonspecific binding removal from protein microarrays using thickness shear mode resonators," *Ieee Sensors Journal*, vol. 6, pp. 254-261, Apr 2006.
- [99] S. Cular, D. W. Branch, V. R. Bhethanbotla, G. D. Meyer, and H. G. Craighead, "Removal of nonspecifically bound proteins on microarrays using surface acoustic waves," *IEEE Sensors Journal*, vol. 8, pp. 314-320, Mar-Apr 2008.
- [100] R. Singh, S. K. R. S. Sankaranarayanan, and V. R. Bhethanabotla, "Orthogonal surface acoustic wave device based on langasite for simultaneous biosensing and biofouling removal," *Applied Physics Letters*, vol. 94, Jun 29 2009.
- [101] D. P. Morgan, "History of SAW devices," in *IEEE International Frequency Control Symposium*, 1998.
- [102] B. A. Auld, *Acoustic fields and waves in solids / B.A. Auld*: Malabar, Fla. : R.E. Krieger, 2nd ed., 1990.
- [103] R. Lerch, "Simulation of piezoelectric devices by two- and three-dimensional finite elements," *Ultrasonics, Ferroelectrics, and Frequency Control, IEEE Transactions on*, vol. 37, pp. 233-247, 1990.
- [104] G. S. Xu, "Direct finite-element analysis of the frequency response of a Y-Z lithium niobate SAW filter," *Smart Materials & Structures*, vol. 9, pp. 973-980, Dec 2000.
- [105] S. K. R. S. Sankaranarayanan and V. R. Bhethanabotla, "Orthogonal surface acoustic wave device based on langasite for simultaneous biosensing and biofouling removal," *Applied Physics Letters*, vol. 94, p. 3p, 2009.
- [106] S. K. R. S. Sankaranarayanan and V. R. Bhethanabotla, "Enhancement of acoustic streaming induced flow on a focused surface acoustic wave device: Implications for biosensing and microfluidics," *Journal of Applied Physics*, vol. 107, p. 9p, 2010.
- [107] A. Abdollahi, Z. Jiang, and S. A. Arabshahi, "Evaluation on mass sensitivity of SAW sensors for different piezoelectric materials using finite-element analysis," *Ieee Transactions on Ultrasonics Ferroelectrics and Frequency Control*, vol. 54, pp. 2446-2455, Dec 2007.
- [108] S. J. Ippolito, K. Kalantar-Zadeh, D. A. Powell, and W. Wlodarski, "A 3-dimensional finite element approach for simulating acoustic wave propagation in layered SAW devices," in *Ultrasonics, 2003 IEEE Symposium on*, 2003, pp. 303-306 Vol.1.

- [109] L. Le Brizoual and O. Elmazria, "FEM modeling of AlN/diamond surface acoustic waves device," *Diamond and Related Materials*, vol. 16, pp. 987-990, 2007.
- [110] M. Buchner, W. Ruile, A. Dietz, and R. Dill, "FEM analysis of the reflection coefficient of SAWs in an infinite periodic array," in *Ultrasonics Symposium, 1991. Proceedings., IEEE 1991*, 1991, pp. 371-375 vol.1.
- [111] Y. Yook-Kong, R. Garon, S. Kanna, and K.-Y. Hashimoto, "Effects of periodically missing fingers and periodically shifted fingers on SAW propagation in quartz resonators," in *Frequency Control Symposium, 1998. Proceedings of the 1998 IEEE International*, 1998, pp. 461-469.
- [112] G. S. Xu and Q. Jiang, "A finite element analysis of second order effects on the frequency response of a SAW device," *Journal of Intelligent Material Systems and Structures*, vol. 12, pp. 69-77, Feb 2001.
- [113] V. Kutiš, G. Gálik, V. Královič, I. Rýger, E. Mojto, and T. Lalinský, "Modelling and Simulation of SAW Sensor Using FEM," *Procedia Engineering*, vol. 48, pp. 332-337, 2012.
- [114] M. Z. Atashbar, B. J. Bazuin, M. Simpeh, and S. Krishnamurthy, "3D FE simulation of H(2)SAW gas sensor," *Sensors and Actuators B-Chemical*, vol. 111, pp. 213-218, Nov 11 2005.
- [115] F. S. Hickernell, "Surface acoustic wave devices: a rewarding past, a significant present, and a promising future," in *Microwaves and Radar, 1998. MIKON '98., 12th International Conference on*, 1998, pp. 159-168 vol.4.
- [116] D. S. Ballantine, R. M. White, S. I. Martin, A. J. Ricco, and E. T. Zellers, *Acoustic Wave Sensors: Theory, Design, and Physico-Chemical Applications*. Chestnut Hill, MA: Academic, 1997.
- [117] K. Yamanouchi, F. M. Nyffeler, and K. Shibayama, "Low Insertion Loss Acoustic Surface Wave Filter Using Group-Type Unidirectional Interdigital Transducer," in *1975 Ultrasonics Symposium*, 1975, pp. 317-321.
- [118] E. Gizelli, A. C. Stevenson, N. J. Goddard, and C. R. Lowe, "Surface skimming bulk waves: a novel approach to acoustic biosensors," in *Solid-State Sensors and Actuators, 1991. Digest of Technical Papers, TRANSDUCERS '91., 1991 International Conference on*, 1991, pp. 690-692.
- [119] K. Saha, F. Bender, and E. Gizeli, "Comparative study of IgG binding to proteins G and A: Nonequilibrium kinetic and binding constant determination with the acoustic waveguide device," *Analytical Chemistry*, vol. 75, pp. 835-842, Feb 15 2003.

- [120] O. Onen, A. A. Ahmad, R. Guldiken, and N. D. Gallant, "Surface Modification on Acoustic Wave Biosensors for Enhanced Specificity," *Sensors*, vol. 12, pp. 12317-12328, Sep 2012.
- [121] D. Samanta and A. Sarkar, "Immobilization of bio-macromolecules on self-assembled monolayers: methods and sensor applications," *Chemical Society Reviews*, vol. 40, pp. 2567-2592, 2011.
- [122] D. M. Disley, D. C. Cullen, H. X. You, and C. R. Lowe, "Covalent coupling of immunoglobulin G to self-assembled monolayers as a method for immobilizing the interfacial-recognition layer of a surface plasmon resonance immunosensor," *Biosensors & Bioelectronics*, vol. 13, pp. 1213-1225, Nov 15 1998.
- [123] C. Mao and W. S. Kisaalita, "Characterization of 3-D collagen hydrogels for functional cell-based biosensing," *Biosensors and Bioelectronics*, vol. 19, pp. 1075-1088, 2004.
- [124] L. Hang, Q. Wang, F. Gao, J. Shi, and F. Gao, "A high-performance DNA biosensor using polyhydroxylated fullereneol as 3D matrix for probe immobilization," *Electrochemistry Communications*, vol. 47, pp. 84-87, 2014.
- [125] A. K. Trilling, J. Beekwilder, and H. Zuilhof, "Antibody orientation on biosensor surfaces: a minireview," *Analyst*, vol. 138, pp. 1619-1627, 2013.
- [126] A. K. Trilling, M. M. Harmsen, V. J. B. Ruigrok, H. Zuilhof, and J. Beekwilder, "The effect of uniform capture molecule orientation on biosensor sensitivity: Dependence on analyte properties," *Biosensors and Bioelectronics*, vol. 40, pp. 219-226, 2013.
- [127] J. Bennès, S. Ballandras, and F. Chérioux, "Easy and versatile functionalization of lithium niobate wafers by hydrophobic trichlorosilanes," *Applied Surface Science*, vol. 255, pp. 1796-1800, 2008.
- [128] Y. Nam, D. W. Branch, and B. C. Wheeler, "Epoxy-silane linking of biomolecules is simple and effective for patterning neuronal cultures," *Biosensors & Bioelectronics*, vol. 22, pp. 589-597, Dec 15 2006.
- [129] G. T. Hermanson, "Bioconjugation techniques," *San Diego*, 1996.
- [130] M. I. R. Gaso, Y. Jiménez, L. A. Francis, and A. Arnau, *Love Wave Biosensors: A Review*, 2013.
- [131] J. C. McDonald, D. C. Duffy, J. R. Anderson, D. T. Chiu, H. K. Wu, O. J. A. Schueller, and G. M. Whitesides, "Fabrication of microfluidic systems in poly(dimethylsiloxane)," *Electrophoresis*, vol. 21, pp. 27-40, Jan 2000.

- [132] S. K. Sia and G. M. Whitesides, "Microfluidic devices fabricated in poly(dimethylsiloxane) for biological studies," *Electrophoresis*, vol. 24, pp. 3563-3576, Nov 2003.
- [133] V. Raimbault, D. Rebiere, C. Dejous, M. Guirardel, J. Pistre, and J. L. Lachaud, "High frequency microrheological measurements of PDMS fluids using saw microfluidic system," *Sensors and Actuators B-Chemical*, vol. 144, pp. 467-471, Feb 17 2010.
- [134] V. Raimbault, D. Rebiere, C. Dejous, M. Guirardel, and V. Conedera, "Acoustic Love wave platform with PDMS microfluidic chip," *Sensors and Actuators a-Physical*, vol. 142, pp. 160-165, Mar 10 2008.
- [135] K. Lange, F. J. Gruhl, and M. Rapp, "Influence of Preparative Carboxylation Steps on the Analyte Response of an Acoustic Biosensor," *IEEE Sensors Journal*, vol. 9, pp. 2033-2034, Dec 2009.
- [136] E. Berkenpas, S. Bitla, P. Millard, and M. P. da Cunha, "Pure shear horizontal SAW biosensor on langasite," *Ieee Transactions on Ultrasonics Ferroelectrics and Frequency Control*, vol. 51, pp. 1404-1411, Nov 2004.
- [137] M. M. Ahmadi and G. A. Jullien, "A Wireless-Implantable Microsystem for Continuous Blood Glucose Monitoring," *Biomedical Circuits and Systems, IEEE Transactions on*, vol. 3, pp. 169-180, 2009.
- [138] J. Kondoh, Y. Okiyama, S. Mikuni, Y. Matsui, M. Nara, T. Mori, and H. Yatsuda, "Development of a Shear Horizontal Surface Acoustic Wave Sensor System for Liquids with a Floating Electrode Unidirectional Transducer," *Japanese Journal of Applied Physics*, vol. 47, pp. 4065-4069, May 2008.
- [139] K. Lange, S. Grimm, and M. Rapp, "Chemical modification of parylene C coatings for SAW biosensors," *Sensors and Actuators B-Chemical*, vol. 125, pp. 441-446, Aug 8 2007.
- [140] S. K. R. S. Sankaranarayanan and V. R. Bhethanabotla, "Enhanced surface acoustic wave biosensor performance via delay path modifications in mutually interacting multidirectional transducer configuration: A computational study," *Applied Physics Letters*, vol. 95, p. 3p, 2009.
- [141] G. Kovacs, W. Ruile, M. Jakob, U. R. E. Maier, U. Knauer, and H. Zottl, "A SAW duplexer with superior temperature characteristics for US-PCS," in *2004 IEEE Ultrasonics Symposium*, 2004, pp. 974-977.
- [142] C.-M. Lin, T.-T. Yen, Y.-J. Lai, V. V. Felmetzger, M. A. Hopcroft, J. H. Kuypers, and A. P. Pisano, "Temperature-Compensated Aluminum Nitride Lamb Wave Resonators," *IEEE Transactions on Ultrasonics, Ferroelectrics, and Frequency Control*, vol. 57, pp. 524-532, 2010.

- [143] S. Krishnamoorthy, A. A. Iliadis, T. Bei, and G. P. Chrousos, "An interleukin-6 ZnO/SiO<sub>2</sub>/Si surface acoustic wave biosensor," *Biosensors and Bioelectronics*, vol. 24, pp. 313-318, 2008.
- [144] L. Le Brizoual, O. Elmazria, F. Sarry, M. El Hakiki, A. Talbi, and P. Alnot, "High frequency SAW devices based on third harmonic generation," *Ultrasonics*, vol. 45, pp. 100-103, 2006.
- [145] K. Kalantar-Zadeh, W. Wlodarski, Y. Y. Chen, B. N. Fry, and K. Galatsis, "Novel Love mode surface acoustic wave based immunosensors," *Sensors and Actuators B: Chemical*, vol. 91, pp. 143-147, 2003.
- [146] S. Chu, W. Water, and J. Liaw, "An investigation of the dependence of ZnO film on the sensitivity of Love mode sensor in ZnO/quartz structure," *Ultrasonics*, vol. 41, pp. 133-139, 2003.
- [147] T. Uemura, S. Fujii, H. Kitabayashi, K. Itakura, A. Hachigo, H. Nakahata, S. Shikata, K. Ishibashi, and T. Imai, "Low-loss diamond surface acoustic wave devices using small-grain poly-crystalline diamond," *Japanese Journal of Applied Physics Part I-Regular Papers Short Notes & Review Papers*, vol. 41, pp. 3476-3479, May 2002.
- [148] M. Zerdali, S. Hamzaoui, F. H. Teherani, and D. Rogers, "Growth of ZnO thin film on SiO<sub>2</sub>/Si substrate by pulsed laser deposition and study of their physical properties," *Materials Letters*, vol. 60, pp. 504-508, Feb 2006.
- [149] I. Sayago, M. Aleixandre, A. Martinez, M. Fernandez, J. P. Santos, J. Gutierrez, I. Gracia, and M. C. Horrillo, "Structural studies of zinc oxide films grown by RF magnetron sputtering," *Synthetic Metals*, vol. 148, pp. 37-41, Jan 3 2005.
- [150] L. Znaidi, G. J. A. A. S. Illia, S. Benyahia, C. Sanchez, and A. V. Kanaev, "Oriented ZnO thin films synthesis by sol-gel process for laser application," *Thin Solid Films*, vol. 428, pp. 257-262, 2003.
- [151] F. Bénédic, M. B. Assouar, F. Mohasseb, O. Elmazria, P. Alnot, and A. Gicquel, "Surface acoustic wave devices based on nanocrystalline diamond and aluminium nitride," *Diamond and Related Materials*, vol. 13, pp. 347-353, 2004.
- [152] B. Bi, W. S. Huang, J. Asmussen, and B. Golding, "Surface acoustic waves on nanocrystalline diamond," *Diamond and Related Materials*, vol. 11, pp. 677-680, 2002.
- [153] K. Mitsakakis, A. Tsortos, J. Kondoh, and E. Gizeli, "Parametric study of SH-SAW device response to various types of surface perturbations," *Sensors and Actuators B: Chemical*, vol. 138, pp. 408-416, 2009.

- [154] S. Sivaramakrishnan, S. Hur, R. Rajamani, W. Robbins, and B. J. Nelson, "Passive Wireless MEMS Microphones for Biomedical Applications," *Journal of Biomechanical Engineering*, vol. 127, p. 5p, 2005.
- [155] Y. M. Soliman, M. F. Su, Z. C. Leseman, C. M. Reinke, I. El-Kady, and R. H. Olsson, "Phononic crystals operating in the gigahertz range with extremely wide band gaps," *Applied Physics Letters*, vol. 97, Nov 8 2010.
- [156] M. F. Su, R. H. Olsson, Z. C. Leseman, and I. El-Kady, "Realization of a phononic crystal operating at gigahertz frequencies," *Applied Physics Letters*, vol. 96, Feb 1 2010.
- [157] M. Richardson, S. K. R. S. Sankaranarayanan, and V. R. Bhethanabotla, "Shear-horizontal surface acoustic wave phononic device with high density filling material for ultra-low power sensing applications," *Applied Physics Letters*, vol. 104, pp. -, 2014.
- [158] R. H. O. III and I. El-Kady, "Microfabricated phononic crystal devices and applications," *Measurement Science and Technology*, vol. 20, pp. 1-13, 2009.
- [159] R. S. Kane, P. Deschatelets, and G. M. Whitesides, "Kosmotropes Form the Basis of Protein-Resistant Surfaces," *Langmuir*, vol. 19, pp. 2388-2391, 2003/03/01 2003.
- [160] Y. Teramura and H. Iwata, "Label-free immunosensing for  $\alpha$ -fetoprotein in human plasma using surface plasmon resonance," *Analytical Biochemistry*, vol. 365, pp. 201-207, 2007.
- [161] R. E. Holmlin, X. Chen, R. G. Chapman, S. Takayama, and G. M. Whitesides, "Zwitterionic SAMs that Resist Nonspecific Adsorption of Protein from Aqueous Buffer," *Langmuir*, vol. 17, pp. 2841-2850, 2001/05/01 2001.
- [162] S. Jiang and Z. Cao, "Ultralow-Fouling, Functionalizable, and Hydrolyzable Zwitterionic Materials and Their Derivatives for Biological Applications," *Advanced Materials*, vol. 22, pp. 920-932, 2010.
- [163] C. Fernández-Sánchez, M. B. González-García, and A. Costa-García, "AC voltammetric carbon paste-based enzyme immunosensors," *Biosensors and Bioelectronics*, vol. 14, pp. 917-924, 2000.
- [164] W. Welsch, C. Klein, R. M. Öksüzoglu, M. von Schickfus, and S. Hunklinger, "Immunosensing with surface acoustic wave sensors," *Sensors and Actuators A: Physical*, vol. 62, pp. 562-564, 1997.
- [165] C. Sun, J. Miao, J. Yan, K. Yang, C. Mao, J. Ju, and J. Shen, "Applications of antibiofouling PEG-coating in electrochemical biosensors for determination of glucose in whole blood," *Electrochimica Acta*, vol. 89, pp. 549-554, 2013.

- [166] Y. S. Chi, B. S. Lee, M. Kil, H.-j. Jung, E. Oh, and I. S. Choi, "Asymmetrically Functionalized, Four-Armed, Poly(ethylene glycol) Compounds for Construction of Chemically Functionalizable Non-Biofouling Surfaces," *Chemistry – An Asian Journal*, vol. 4, pp. 135-142, 2009.
- [167] T. Waterboer, P. Sehr, and M. Pawlita, "Suppression of non-specific binding in serological Luminex assays," *Journal of Immunological Methods*, vol. 309, pp. 200-204, 2006.
- [168] D. J. Rodda and H. Yamazaki, "Poly(Vinyl Alcohol) as a Blocking Agent in Enzyme Immunoassays," *Immunological Investigations*, vol. 23, pp. 421-428, 1994.
- [169] S. K. R. S. Sankaranarayanan, S. Cular, V. R. Bhethanabotla, and B. Joseph, "Flow induced by acoustic streaming on surface-acoustic-wave devices and its application in biofouling removal: A computational study and comparisons to experiment," *Physical Review E*, vol. 77, Jun 2008.
- [170] S. K. R. S. Sankaranarayanan, R. Singh, and V. R. Bhethanabotla, "Acoustic streaming induced elimination of nonspecifically bound proteins from a surface acoustic wave biosensor: Mechanism prediction using fluid-structure interaction models," *Journal of Applied Physics*, vol. 108, Nov 15 2010.
- [171] R. A. Bowling, *Particles on Surface-Detection, Adhesion, and Removal*. Plenum, New York, 1988.
- [172] H. Krupp, *Particle adhesion theory and experiment*. Amsterdam: Elsevier, 1967.
- [173] Q. Qi and G. J. Brereton, "Mechanisms of Removal of Micron-Sized Particles by High-Frequency Ultrasonic-Waves," *Ieee Transactions on Ultrasonics Ferroelectrics and Frequency Control*, vol. 42, pp. 619-629, Jul 1995.
- [174] V. I. Cherednik and M. Y. Dvoesherstov, "Propagation of surface acoustic waves in a piezoelectric medium with a periodic groove structure," *Acoustical Physics*, vol. 56, pp. 37-46, 2010/01/01 2010.
- [175] S. Furukawa, T. Nomura, and T. Yasuda, "Characteristic Features of Leaky Surface Acoustic-Waves Propagating on Liquid Piezoelectric Film Glass Structures," *Journal of Physics D-Applied Physics*, vol. 24, pp. 706-713, May 14 1991.
- [176] R. M. Moroney, "Ultrasonic Microtransport," Ph.D., University of California, Berkeley, 1995.
- [177] Z. Guttenberg, A. Rathgeber, S. Keller, J. O. Radler, A. Wixforth, M. Kostur, M. Schindler, and P. Talkner, "Flow profiling of a surface-acoustic-wave nanopump," *Physical Review E*, vol. 70, Nov 2004.

- [178] A. Sano, Y. Rlatsui, and S. Shiokawa, "A new manipulator based on surface acoustic wave streaming," in *Ultrasonics Symposium, 1997. Proceedings., 1997 IEEE*, 1997, pp. 467-470 vol.1.
- [179] S. Shiokawa, Y. Matsui, and T. Moriizumi, "Experimental-Study on Liquid Streaming by Saw," *Japanese Journal of Applied Physics Part 1-Regular Papers Short Notes & Review Papers*, vol. 28, pp. 126-128, 1989.
- [180] J. N. Israelachvili, *Intermolecular and surface forces [electronic resource] / Jacob N. Israelachvili*: Burlington, MA : Academic Press, 3rd ed., 2011.
- [181] K. Mitsakakis and E. Gizeli, "Detection of multiple cardiac markers with an integrated acoustic platform for cardiovascular risk assessment," *Analytica Chimica Acta*, vol. 699, pp. 1-5, Aug 5 2011.
- [182] J. Hechner and W. Soluch, "Pseudo surface acoustic wave dual delay line on 41 degrees YX LiNbO3 for liquid sensors," *Sensors and Actuators B-Chemical*, vol. 111, pp. 436-440, Nov 11 2005.
- [183] G. L. Harding, J. Du, P. R. Dencher, D. Barnett, and E. Howe, "Love wave acoustic immunosensor operating in liquid," *Sensors and Actuators a-Physical*, vol. 61, pp. 279-286, Jun 1997.
- [184] W. Welsch, C. Klein, R. M. Oksuzoglu, M. vonSchickfus, and S. Hunklinger, "Immunosensing with surface acoustic wave sensors," *Sensors and Actuators a-Physical*, vol. 62, pp. 562-564, Jul 1997.
- [185] Y. S. Chi, H. R. Byon, H. C. Choi, and I. S. Choi, "A Noncovalent Approach to the Construction of Tween 20-Based Protein Microarrays," *ChemBioChem*, vol. 8, pp. 1380-1387, 2007.
- [186] F. Josse and Z. Shana, "Analysis of shear horizontal surface waves at the boundary between a piezoelectric crystal and a viscous fluid medium," *The Journal of the Acoustical Society of America*, vol. 84, pp. 978-984, 1988.
- [187] A. Renaudin, P. Tabourier, V. Zhang, J. C. Camart, and C. Druon, "SAW nanopump for handling droplets in view of biological applications," *Sensors and Actuators B: Chemical*, vol. 113, pp. 389-397, 2006.
- [188] R. Raghavan, J. Friend, and L. Yeo, "Particle concentration via acoustically driven microcentrifugation: microPIV flow visualization and numerical modelling studies," *Microfluidics and Nanofluidics*, vol. 8, pp. 73-84, 2010/01/01 2010.
- [189] G. Kovacs, M. J. Vellekoop, R. Haueis, G. W. Lubking, and A. Venema, "A Love Wave Sensor for (Bio)Chemical Sensing in Liquids," *Sensors and Actuators a-Physical*, vol. 43, pp. 38-43, May 1994.

- [190] T. Franke, A. R. Abate, D. A. Weitz, and A. Wixforth, "Surface acoustic wave (SAW) directed droplet flow in microfluidics for PDMS devices," *Lab on a Chip*, vol. 9, pp. 2625-2627, 2009.
- [191] M. Richardson, S. Morrill, K. J. Suthar, S. K. R. S. Sankaranarayanan, and V. R. Bhethanabotla, "Removal of Non-Specifically Bount Proteins using Rayleigh Waves on an ST-Quartz Substrate," *Sensors and Actuators A: Physical*, 2014 submitted for publication
- [192] R. Singh, S. K. R. S. Sankaranarayanan, and V. R. Bhethanabotla, "Enhanced surface acoustic wave biosensor performance via delay path modifications in mutually interacting multidirectional transducer configuration: A computational study," *Applied Physics Letters*, vol. 95, pp. -, 2009.

## **APPENDICES**

## Appendix A Copyright Permission for Chapter 4



RightsLink®

Home

Account Info

Help



**Title:** Low Insertion Loss and Highly Sensitive SH-SAW Sensors Based on 36° YX LiTaO<sub>3</sub> Through the Incorporation of Filled Microcavities

**Author:** Richardson, M.; Sankaranarayanan, S.K.R.S.; Bhethanabotla, V.R.

**Publication:** IEEE Sensors Journal

**Publisher:** IEEE

**Date:** Feb. 2015

Copyright © 2015, IEEE

Logged in as:  
Mandek Richardson

LOGOUT

### Thesis / Dissertation Reuse

**The IEEE does not require individuals working on a thesis to obtain a formal reuse license, however, you may print out this statement to be used as a permission grant:**

*Requirements to be followed when using any portion (e.g., figure, graph, table, or textual material) of an IEEE copyrighted paper in a thesis:*

- 1) In the case of textual material (e.g., using short quotes or referring to the work within these papers) users must give full credit to the original source (author, paper, publication) followed by the IEEE copyright line © 2011 IEEE.
- 2) In the case of illustrations or tabular material, we require that the copyright line © [Year of original publication] IEEE appear prominently with each reprinted figure and/or table.
- 3) If a substantial portion of the original paper is to be used, and if you are not the senior author, also obtain the senior author's approval.

*Requirements to be followed when using an entire IEEE copyrighted paper in a thesis:*

- 1) The following IEEE copyright/ credit notice should be placed prominently in the references: © [year of original publication] IEEE. Reprinted, with permission, from [author names, paper title, IEEE publication title, and month/year of publication]
- 2) Only the accepted version of an IEEE copyrighted paper can be used when posting the paper or your thesis on-line.
- 3) In placing the thesis on the author's university website, please display the following message in a prominent place on the website: In reference to IEEE copyrighted material which is used with permission in this thesis, the IEEE does not endorse any of [university/educational entity's name goes here]'s products or services. Internal or personal use of this material is permitted. If interested in reprinting/republishing IEEE copyrighted material for advertising or promotional purposes or for creating new collective works for resale or redistribution, please go to [http://www.ieee.org/publications\\_standards/publications/rights/rights\\_link.html](http://www.ieee.org/publications_standards/publications/rights/rights_link.html) to learn how to obtain a License from RightsLink.

If applicable, University Microfilms and/or ProQuest Library, or the Archives of Canada may supply single copies of the dissertation.

BACK

CLOSE WINDOW

Copyright © 2015 [Copyright Clearance Center, Inc.](#) All Rights Reserved. [Privacy statement](#). [Terms and Conditions](#).

Comments? We would like to hear from you. E-mail us at [customercare@copyright.com](mailto:customercare@copyright.com)

## Appendix B Copyright Permission for Chapter 5



The screenshot shows the AIP Publishing website. At the top left is the AIP Publishing logo. Below it is a navigation bar with links: About, Publications, Librarians, Authors, Publishing Partners, Advertisers, Careers, and Contact Us. A dropdown menu is open under 'About', showing 'Before you begin' (highlighted) and 'Why publish with AIP?'. To the right of the dropdown, the text 'Copyright and Permission to Reuse AIP Material FAQ' and 'Copyright' is visible.

### Q: May I include my AIP article in my thesis or dissertation?

AIP permits authors to include their published articles in a thesis or dissertation. It is understood that the thesis or dissertation may be published in print and/or electronic form and offered for sale, as well as included in a university's repository. Formal permission from AIP is not needed. If the university requires written permission, however, we are happy to supply it.

### AIP PUBLISHING LLC LICENSE TERMS AND CONDITIONS

Mar 17, 2015

**All payments must be made in full to CCC. For payment instructions, please see information listed at the bottom of this form.**

License Number	3591670085857
Order Date	Mar 17, 2015
Publisher	AIP Publishing LLC
Publication	Applied Physics Letters
Article Title	Shear-horizontal surface acoustic wave phononic device with high density filling material for ultra-low power sensing applications
Author	M. Richardson, S. K. R. S. Sankaranarayanan, V. R. Bhethanabotla
Online Publication Date	Jun 23, 2014
Volume number	104
Issue number	25
Type of Use	Thesis/Dissertation
Requestor type	Author (original article)
Format	Print and electronic
Portion	Excerpt (> 800 words)
Will you be translating?	No
Title of your thesis / dissertation	Theoretical and Experimental Investigations to Improve the Performance of Surface Acoustic Wave (SAW) Biosensors
Expected completion date	May 2015
Estimated size (number of pages)	150
Total	0.00 USD
Terms and Conditions	

AIP Publishing LLC -- Terms and Conditions: Permissions Uses

AIP Publishing LLC ("AIPP") hereby grants to you the non-exclusive right and license to use and/or distribute the Material according to the use specified in your order, on a one-time basis, for the specified term, with a maximum distribution equal to the number that you have ordered. Any links or other content accompanying the Material are not the subject of this license.

1. You agree to include the following copyright and permission notice with the reproduction of the Material: "Reprinted with permission from [FULL CITATION]. Copyright [PUBLICATION YEAR], AIP Publishing LLC." For an article, the copyright and permission notice must be printed on the first page of the article or book chapter. For photographs, covers, or tables, the copyright and permission notice may appear with the Material, in a footnote, or in the reference list.
2. If you have licensed reuse of a figure, photograph, cover, or table, it is your responsibility to ensure that the material is original to AIPP and does not contain the copyright of another entity, and that the copyright notice of the figure, photograph, cover, or table does not indicate that it was reprinted by AIPP, with permission, from another source. Under no circumstances does AIPP, purport or intend to grant permission to reuse material to which it does not hold copyright.
3. You may not alter or modify the Material in any manner. You may translate the Material into another language only if you have licensed translation rights. You may not use the Material for promotional purposes. AIPP reserves all rights not specifically granted herein.
4. The foregoing license shall not take effect unless and until AIPP or its agent, Copyright Clearance Center, receives the Payment in accordance with Copyright Clearance Center Billing and Payment Terms and Conditions, which are incorporated herein by reference.
5. AIPP or the Copyright Clearance Center may, within two business days of granting this license, revoke the license for any reason whatsoever, with a full refund payable to you. Should you violate the terms of this license at any time, AIPP, AIP Publishing LLC, or Copyright Clearance Center may revoke the license with no refund to you. Notice of such revocation will be made using the contact information provided by you. Failure to receive such notice will not nullify the revocation.
6. AIPP makes no representations or warranties with respect to the Material. You agree to indemnify and hold harmless AIPP, AIP Publishing LLC, and their officers, directors, employees or agents from and against any and all claims arising out of your use of the Material other than as specifically authorized herein.
7. The permission granted herein is personal to you and is not transferable or assignable without the prior written permission of AIPP. This license may not be amended except in a writing signed by the party to be charged.
8. If purchase orders, acknowledgments or check endorsements are issued on any forms containing terms and conditions which are inconsistent with these provisions, such inconsistent terms and conditions shall be of no force and effect. This document, including the CCC Billing and Payment Terms and Conditions, shall be the entire agreement between the parties relating to the subject matter hereof.

This Agreement shall be governed by and construed in accordance with the laws of the State of New York. Both parties hereby submit to the jurisdiction of the courts of New York County for purposes of resolving any disputes that may arise hereunder.

**Questions? [customercare@copyright.com](mailto:customercare@copyright.com) or +1-855-239-3415 (toll free in the US) or +1-978-646-2777.**